



MONASH University

Thermal Mixing of Fractal Geometry Induced Turbulence

by

Teh An Liang

A dissertation submitted to the faculty of

Department of Mechanical Engineering

Monash University Malaysia

In fulfilment of the requirements for the degree

Master of Engineering Science (Research), MEngSc(Res)

21st September 2015

Copyright Notices

Notice 1

Under the Copyright Act 1968, this thesis must be used only under the normal conditions of scholarly fair dealing. In particular, no results or conclusions should be extracted from it, nor should it be copied or closely paraphrased in whole or in part without the written consent of the author. Proper written acknowledgement should be made for any assistance obtained from this thesis.

Notice 2

I certify that I have made all reasonable efforts to secure copyright permission for third-party content included in this thesis and have not knowingly added copyright content to my work without the owner's permission.

Statement of Authorship

I hereby declare that the thesis titled “Thermal Mixing of Fractal Geometry Induced Turbulence” is submitted with accordance to requirements for Master of Engineering Science (Research) in the Department of Mechanical Engineering of Monash University Malaysia. The thesis:

- Contains no material which has been accepted for the award to the candidate of any other degree or diploma at any university or equivalent institution, except where due reference is made in the text of examinable outcome.
- To the best of this candidate’s knowledge contains no materials published or written by another person except where due reference is made in the text of the examinable outcome.

Name: TEH AN LIANG
.....

Signature: 
.....

Date: 14/09/2015
.....

PART A: General Declaration

Monash University

Declaration for thesis based or partially based on conjointly published or unpublished work

General Declaration

In accordance with Monash University Doctorate Regulation 17.2 Doctor of Philosophy and Research Master's regulations the following declarations are made:

I hereby declare that this thesis contains no material which has been accepted for the award of any other degree or diploma at any university or equivalent institution and that, to the best of my knowledge and belief, this thesis contains no material previously published or written by another person, except where due reference is made in the text of the thesis.

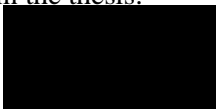
This thesis includes **one** original papers **accepted** in peer reviewed journals and **one** unpublished publications. The core theme of the thesis is **Thermal Mixing of Fractal Geometry Induced Turbulence**. The ideas, development and writing up of all the papers in the thesis were the principal responsibility of myself, the candidate, working within the **Department of Mechanical Engineering** under the supervision of **Dr. Foo Ji Jinn** and **Dr. Tan Boon Thong**.

[The inclusion of co-authors reflects the fact that the work came from active collaboration between researchers and acknowledges input into team-based research.]

In the case of **chapter 5 and 6**, my contribution to the work involved the following:

Thesis chapter	Publication title	Publication status	Nature and extent of candidate's contribution
5	Thermal Mixing Enhancement of Free Cooling/Heating System with 2D Space Filling Plate	Accepted and published (ISI Q1, 18th June 2015)	Main author, contributes constructive comments, insights, and analysis towards results and discussion section of this paper.
6	Thermal Mixing Enhancement of Free-Cooling System with Fractal Orifice Plate	Accepted and published (ISI Q1, 7th May 2015)	Main author, construction of wind tunnel, compiling results and provides constructive comments, insight, and analysis towards results and discussion section of this paper.

I have renumbered sections of submitted or published papers in order to generate a consistent presentation within the thesis.

Signed: 

Date: 14/09/2015

ACKNOWLEDGEMENT

Huge amount of dedications in both time and effort have been placed into the present study by the candidate. However, credit must be given where credit is due to a group of remarkable people, to whom had also dedicate much of their time and effort to assist, to supervise, and to contribute technically, morally, and emotionally support towards the candidate and the present study.

First and foremost, I wish to express my sincerest appreciation to my main supervisor Dr. Foo Ji Jinn who accepted me as part of his research group at a time of loss and uncertainty during my candidature. His guidance and support are invaluable and instrumental towards the successful conclusion this study and his helpful advices given in research skills will be dearly remembered and utilised in my future career path. Next, I wish to thank Dr. Tan Boon Thong as my co-supervisor, who provided access to his facilities which are helpful in the present study.

Following on, I wish to thank my parents for their unwavering support towards my education which enables me to stand at where I am today, and my family members for their accommodating support. Furthermore, I am grateful to my colleagues and friends, to whom had been through thick and thin, anxious and joyous times together, and their provision of constructive comments and helpful ideas throughout the course of my candidature, especially Jason Gan Jie Sheng, Parisa Amouzgar, and Yong Kai Yen for their help in the proof-reading of this thesis.

I am also thankful to several undergraduate students, Siow Yong Hoi, Siti Munirah Anuar, Amar Ikhwan bin Ab'llah, Teh Eng Khim, and Chin Kee Wen, to whom had been working together within the same research group and their assistance during setting up the wind tunnel together, as well as gathering of experimental and numerical data. Without their keen contributions, this project would not have started off smoothly and concluded in a fruitful manner.

Last but not least, I would like to acknowledge Malaysia Ministry of Education (MOE) for the financial support for the present research project through Project Code: FRGS/1/2012/TK07/SEGI/02/1 and Monash University Malaysia (MUM) for supporting the high

speed computing system under Research Project No.: 5140810-113-00, as well as the provision of tuition fee waiver for the last three months of the candidature.

ABSTRACT

The present study focuses on exploring numerically the possibility of employing the unique features of fractal geometry to strengthen the thermal mixing performance of a free cooling system that placing within a heating, ventilation and air conditioning system (HVAC). Square duct is used throughout the study with different hydrodynamic inlet conditions, i.e. (i) co-axial flow injection, and (ii) T -duct channelling of working fluid at different temperatures. In general, grid type and orifice-liked inserts are investigated, namely: (i) regular grid (RG), (ii) 2D space filling square fractal grid (SFG), and (iii) orifices. Numerical validations using experimental results from [Mazellier and Vassilicos \(2010\)](#), [Morrison, Deotte, Nail, and Panak \(1993\)](#), [Nicolleau, Salim, and Nowakowski \(2011\)](#), as well as the in-house wind tunnel experiments are conducted. Clearly, all the numerical predictions are in good agreement with the recorded data. Three physical scenarios are then revealed in phases. The first phase aims to evaluate the thermal mixing performance between grid inserts (RG and SFG) and circular orifice (CO) of different thicknesses at $\delta = 5\text{mm}$ and 40mm . It is found that CO outperforms the rest in thermal mixing, where wider in range and higher in value of turbulence kinetic energy is generated leeward from the orifice. In phase two, the effects of inserts tilting at $\beta = 0^\circ, \pm 45^\circ$ are performed using positive square fractal grid (PSFG), negative square fractal grid (NSFG), and CO. It is observed that tilted inserts thermal mixing are significantly better than the non-tilted cases. This is due to the increase in insert surface area in producing larger scales of flow fluctuation. Hence, $\beta = +45^\circ$ tilted CO thermal mixing performance is about 1382% and 374% higher than PSFG and NSFG, respectively, at $x / H = 4.2$. Lastly, the implementation of fractal characteristics around the perimeter of an orifice is carried out to further improve thermal mixing. The selected geometries include (i) CO, (ii) square orifice (SO), (iii) square fractal orifice (SFO), and (iv) Koch's fractal orifice (KSFO). The result show that KSFO generated area-averaged turbulence kinetic energy of about 37%, 48%, 371%, and 1454% higher than those of CO, SO, SFO. Overall, KSFO forms a good balance between the pressure coefficient and the thermal mixing at a Re_H of 1.94×10^4 .

Keywords: *fractal geometry, orifice, thermal mixing, CFD, HVAC, free cooling*

PUBLICATIONS

Teh, A. L., Siow, Y. H., Chin, W. M., Chia, C. M., & Foo, J. J. (2015). Thermal mixing enhancement of a free cooling/heating system with a 2D space-filling plate. *Applied Thermal Engineering*, 89, 946-957. doi:<http://dx.doi.org/10.1016/j.applthermaleng.2015.06.058> (**ISI Q1**, **Accepted on 18th June 2015**).

Teh, A. L., Chin, K. W., Teh, E. K., Chin, W. M., Chia, C. M., & Foo, J. J. (2015). Thermal mixing enhancement of a free-cooling system with a fractal orifice plate. *Chemical Engineering Research and Design*, 100, 57-71. doi:<http://dx.doi.org/10.1016/j.cherd.2015.05.009> (**ISI Q1**, **Accepted on 7th May 2015**).

TABLE OF CONTENTS

ACKNOWLEDGEMENT	I
ABSTRACT	III
PUBLICATIONS	IV
NONMENCLATURE	VIII
ABBREVIATION	XI
LIST OF TABLES.....	XII
LIST OF FIGURES	XIII
CHAPTER 1 – INTRODUCTION	1
Research Aims	4
Thesis Outline	5
CHAPTER 2 – LITERATURE REVIEW	7
Mixing.....	7
Turbulence Generated by Three-Dimensional Fractal Object	7
Two-Dimensional Regular Grids, Planar Fractal Grids and Orifices	9
Numerical Methods for CFD	24
Free-cooling system in HVAC	25
CHAPTER 3 –METHODOLOGY	27
Validation of turbulence models	27
Numerical simulation.....	32
PHASE 1: Thermal mixing enhancement of a co-axially inlets with a 2D space filling inserts	32
PHASE 2: Thermal mixing enhancement after a <i>T</i> -duct with a 2D space filling insert	37
PHASE 3: Thermal mixing enhancement after a <i>T</i> -duct with a fractal orifice insert	40
CHAPTER 4 – RESULTS AND DISCUSSION : PHASE 1 Thermal mixing enhancement of a co-axially inlets with a 2D space filling inserts	45
Validation of numerical results.....	45

Effects of different inserts and thickness on normalised centreline velocity	48
Thermal mixing performance of the various plates	50
Influence of turbulence kinetic energy on thermal mixing performance	52
Stream-wise cross-section temperature, turbulence kinetic energy contour, and velocity streamline plot.....	55
LES simulated velocity fluctuation using CO-5 insert	59
Pressure drop and system performance of the various inserts	64
Chapter summary	67
PART B: Suggested Declaration for Thesis Chapter 5	69
CHAPTER 5 – RESULTS AND DISCUSSION : PHASE 2 Thermal mixing enhancement after a <i>T</i> -duct with a 2D space filling insert.....	71
Validation of numerical simulations	71
Effects of various inserts and tilted angle on thermal mixing performance.....	74
Influence of turbulence kinetic energy with different space-filling inserts and tilting configurations	78
Vertical velocity profiles at several location downstream at $z / H = 0.5$ for CO and NSFG inserts for all tilting configuration	85
Pressure drop and system performance of the various inserts	88
Chapter summary	91
PART B: Suggested Declaration for Thesis Chapter 6	93
CHAPTER 6 – RESULTS AND DISCUSSION : PHASE 3 Thermal mixing enhancement after a <i>T</i> -duct with a fractal orifice insert.....	95
Validation of numerical validation	95
Thermal mixing performance of the different inserts	101
Influence of turbulence kinetic energy using different orifice inserts	105
Vertical velocity profiles downstream of the inserts.....	110
Pressure drop and system performance among the various inserts.....	113
Chapter summary	117

CHAPTER 7 – CONCLUSION AND RECCOMENDATIONS	119
REFERENCES	121
Appendix A Turbulence Theory	127
Navier-Stokes Equation	127
Reynolds-averaged Navier-Stokes Equations.....	127
k - ε Turbulence Model	127
Reynolds Stress Model (RSM)	130
Large Eddy Simulation (LES) Model.....	134
Appendix B Wind Tunnel Technical Drawings.....	137

NONMENCLATURE

A	Area filled by the grid
C_d	Drag coefficient
d	Normal distance to the wall
D_f	Fractal dimension
H	Test section cross-section length
k	Turbulence kinetic energy
k_A or k_{ave}	Cross-sectional area-averaged turbulence kinetic energy
k_{norm}	Normalised k_A over $k_{A,EC}$
L_0	Length of the largest bar
L_u	Longitudinal integral length scale
M_{eff}	Effective mesh size
N	Number of fractal iterations
Nu	Nusselt number
P or p	Static pressure
ΔP	Pressure difference
P_{in}	Pressure before insert
P_{out}	Pressure after insert
P_f	Fractal perimeter length
Pr	Prandtl number
T	Test section cross-section length
T_A	Cross-sectional area-averaged temperature
Re	Reynolds number
t_{max} or t_0	Thickness of largest bar in square fractal grid
t_{min}	Thickness of smallest bar in square fractal grid
t_r	Thickness ratio
$T_{A,ave}$	Averaged value for the temperature for the cross-section at distance x / H downstream

$T_{A,max}$	Maximum value for the temperature for the cross-section at distance x / H downstream
$T_{A,min}$	Minimum value for the temperature for the cross-section at distance x / H downstream
T_H	Temperature for warm air inlet
T_C	Temperature for cool air inlet
u	Velocity
U_∞	Inlet velocity
U_C	Centreline velocity
U_P	Plateau velocity described in Mazellier and Vassilicos (2010)
U_{max}	Maximum velocity
x_*	Characteristic length scale of SFG defined by Mazellier and Vassilicos (2010)
x_{peak}	Location of peak turbulence intensity in square fractal grid

Greek Symbols

α	Free-stream turbulence intensity and length scale parameter
β	Tilting angle of insert
δ	Thickness of the insert
η	Overall system performance
ε	Turbulence kinetic energy dissipation rate
λ	Taylor microscale
ρ	Density of fluid
σ	Blockage ratio (Area of covered space over total area of test section)
θ	Normalised difference between cross-sectional area-averaged temperature and T_H over temperature difference between T_H and T_C
$\Delta\theta$	Normalised maximum cross-sectional temperature difference
Θ	Thermal mixing performance

ABBREVIATION

2D	Two-dimensions
3D	Three-dimensions
CCD	Charge-coupled device
CO	Circular orifice
DES	Detached eddy simulation
DNS	Direct numerical simulation
EC	Empty channel
GHG	Greenhouse gas
GOY	Gledzer, Ohkitani, and Yamada
HVAC	Heating, ventilating, and air-conditioning
IBM	Immersed boundary method
KSFO	Koch fractal orifice
LES	Large eddy simulation
Nd:YAG	Neodymium-doped yttrium aluminium garnet; Nd:Y ₃ Al ₅ O ₁₂
NSFG	Negative square fractal grid
PIV	Particle image velocimetry
PLIF	Planar laser-induced fluorescence
PSFG	Positive square fractal grid
RANS	Reynolds averaged Navier-Stokes
RG	Regular biplanar grid
RSM	Reynolds stress model
SFG or SG	Space-filling square fractal grid
SFO	Square fractal orifice
SO	Square orifice
SSM	Space-scale unfolding mechanism
T	“Tee” joint

LIST OF TABLES

<i>Table 1.</i> Space-filling square fractal grids geometry details used in Gomes-Fernandes et al. (2012), dimensions in millimetre (mm)	21
<i>Table 2.</i> SFG parameters and x_{peak} by Suzuki et al. (2013).....	23
<i>Table 3.</i> Geometry of space-filling square fractal grids used by Mazellier and Vassilicos (2010), dimensions in millimetre (mm).....	28
<i>Table 4.</i> Number of mesh elements for each case in PHASE 1	35
<i>Table 5.</i> Boundary conditions set for all cases in PHASE 1	35
<i>Table 6.</i> Dimensions for inserts used in PHASE 2	39
<i>Table 7.</i> Dimensions for regular orifices and fractal orifices.....	43
<i>Table 8.</i> Standard deviation for u_x / U , u_y / U , and u_z / U at y / H & $z / H = 0$	63
<i>Table 9.</i> Standard deviation for u_x / U , u_y / U , and u_z / U at y / H & $z / H = 0.125$	63
<i>Table 10.</i> Standard deviation for u_x / U , u_y / U , and u_z / U at y / H & $z / H = 0.313$	63
<i>Table 11.</i> Space filling inserts blockage ratios	75

LIST OF FIGURES

<i>Figure 1.</i> (a) Three-dimensional fractal object stirrer proposed by Staicu et al. (2003), (b – d) two-dimensional planar fractal grids proposed by Hurst and Vassilicos (2007), (e) two-dimensional planar fractal orifices (Koch snowflake) by Aly et al. (2010).....	3
<i>Figure 2.</i> Free-cooling system in HVAC	5
<i>Figure 3.</i> Test section with 3D fractal grid inserted by Queiros-Conde and Vassilicos (2001)	8
<i>Figure 4.</i> Fractal generating patterns extracted from Hurst and Vassilicos (2007)	11
<i>Figure 5.</i> (a) Bar length L_i and bar thickness t_i used in the space-filling square fractal grids; (b) and (c) illustrates square fractal grid $N = 4$ and $N = 5$ used in the investigation by Mazellier and Vassilicos (2010)	12
<i>Figure 6.</i> Schematic of the experimental apparatus used in Geipel et al. (2010)	13
<i>Figure 7.</i> Fractal cross grids used by Geipel et al. (2010)	14
<i>Figure 8.</i> Experimental setup by Suzuki, Nagata, Sakai, and Ukai (2010)	15
<i>Figure 9.</i> Instantaneous fluctuating velocity vector field for regular grid (top) and SFG (middle), $ \mathbf{V} = 0.1$ (red), $ \mathbf{V} = 0.05$ (green), $ \mathbf{V} \approx 0.0$ (blue) as extracted from Suzuki, Nagata, Sakai, and Ukai (2010).....	15
<i>Figure 10.</i> Instantaneous scalar fields turbulence by (a) regular grid and (b) SFG by Suzuki, Nagata, Sakai, and Ukai (2010), $c = 1$ (red), $c = 0.5$ (white), and $c = 0$ (blue)	15
<i>Figure 11.</i> Instantaneous temperature fields in (a) regular grid, (b) $N = 4$ SFG $t_r = 5.0$, and (c) $N = 4$ SFG $t_r = 8.5$ by Suzuki, Nagata, Sakai, and Ukai (2010); non-dimensioned temperature of $T = 1$ (red), $T = 0.5$ (white), and $T = 0$ (blue)	16
<i>Figure 12.</i> Instantaneous fluctuating temperature fields in (a) regular grid, (b) $N = 4$ SFG $t_r = 5.0$, and (c) $N = 4$ SFG $t_r = 8.5$ by Suzuki, Nagata, Sakai, and Ukai (2010); non-dimensioned temperature of $\theta = 0.3$ (red), $\theta = 0$ (white), and $\theta = -0.3$ (blue).....	17
<i>Figure 13.</i> Downstream evolution of U / U_∞ , V / U_∞ , W / U_∞ , and $(u'^2)^{1/2} / U_\infty$ (top to bottom) for (a) regular grid, and (b) space-filling square fractal grid $t_r = 5$, $N = 4$, from Laizet and Vassilicos (2011).....	18

<i>Figure 14.</i> (a) An illustration of the water tunnel PIV set up and (b) detailed schematic for the construct of space-filling fractal grid used by Gomes-Fernandes et al. (2012)	20
<i>Figure 15.</i> Schematic of space-scale unfolding mechanism (SSU) mechanism by Laizet and Vassilicos (2012)	21
<i>Figure 16.</i> Orifice plate (s1c) and evolution of fractal orifice plate (s1f0 to s1f3) by Salim and Nicolleau (2012)	22
<i>Figure 17.</i> Diagram of $N = 3$ SFG used by Soulopoulos et al. (2013)	23
<i>Figure 18.</i> SolidWorks models of (a) SFG17 space-filling plate insert and (b) interior air space of the wind tunnel test section from Mazellier and Vassilicos (2010).....	28
<i>Figure 19.</i> Close up view of the SFG17 insert in the cuboid air space (left), dimension for the cuboid air space (top right) and location of the SFG17 insert (bottom right).....	29
<i>Figure 20.</i> Numerical setup as accordance to the experimental setup in Morrison et al. (1993)...	31
<i>Figure 21.</i> Schematic of computational domain and the dimensions for PHASE 1 study, the coloured faces at the inlet represent warm air inlet (in red) and cool air inlet (in blue)	33
<i>Figure 22.</i> Illustration of $160 \times 160 \text{ mm}^2$ turbulence generator inserts (a) Regular Grid (RG), (b) Square Fractal Grid (SG), and (c) Circular Orifice (CO); black area represents filled-space whilst the rest are spaces which allows air to pass through.....	34
<i>Figure 23.</i> Dimensions for test section employed in PHASE 2 (top), and the inserts (a) positive square fractal grid (PSFG), (b) negative square fractal grid (NSFG), and (c) circular orifice (CO)	38
<i>Figure 24.</i> (a) Schematic for the wind tunnel test section experimental setup, and (b) its dimensions	41
<i>Figure 25.</i> (i) Square orifice (SO), (ii) circular orifice (CO), (iii) square fractal orifice, (iv) Koch fractal orifice (KSFO); red dotted line represents triangle “cut-out” at $N = 1$ and cyan dotted line represents $N = 2$	42
<i>Figure 26.</i> Variation of normalised centreline velocity U_C / U_P of $N = 4$ SFG17 with thickness $\delta = 5\text{mm}$ in the lee of the insert: numerical validation	46

<i>Figure 27.</i> Comparisons of the present numerical model with earlier reported experimental data for orifice insert: (a) U_C / U_{max} and (b) $(P - P_{out}) / (P_{in} - P_{out})$	47
<i>Figure 28.</i> RSM calculated steady-state normalised centreline velocities U_C / U_{∞} between RG-5, RG-40, $N = 3$ SG-5, $N = 3$ SG-40, CO-5, CO-40, and EC leeward of the insert.....	49
<i>Figure 29.</i> Comparisons of thermal mixing performance level among different inserts.....	51
<i>Figure 30.</i> Comparisons of area-averaged turbulence kinetic energy between the various inserts using steady-state RSM model	53
<i>Figure 31.</i> Planar turbulence kinetic energy histogram for SG-5 (a, c, e, g, i) and CO-5 (b, d, f, h, j).....	54
<i>Figure 32.</i> RSM calculated steady-state 45° diagonal section 1-1' temperature distribution (top), turbulent kinetic energy (middle), and velocity streamline (bottom) contour plot for (a) empty channel, (b) RG-5, (c) SG-5, and (d) CO-5, respectively – Scaling in $y/H : x/H = 1 : 2.5$	57
<i>Figure 33.</i> 45° diagonal temperature distributions and velocity profiles in the lee of the insert of (a) SG-5 and (b) CO-5 at downstream distance $x/H = 21.88$	58
<i>Figure 34.</i> U_C / U_{in} velocity fluctuations between steady-state RSM and transient LES simulation ($\Delta t = 1s$) for CO-5 along the diagonal distance of $y/H = z/H$ i.e., at (a) $z/H = 0$, (b) $z/H = 0.125$, and (c) $z/H = 0.313$	61
<i>Figure 35.</i> Velocity components u_x / U , u_y / U , and u_z / U in the lee of CO-5 at $x/H = 3.13$, 6.25, 9.38, and 21.88, along the diagonal distance i.e. y/H & $z/H = 0$ (top, a-c), 0.125 (middle, d-f), and 0.313 (bottom, g-i)	62
<i>Figure 36.</i> Numerically examined pressure drop of each insert with RSM modeling	65
<i>Figure 37.</i> Overall system performance level for the present study	66
<i>Figure 38.</i> Numerical validation between the present work and experimental results by Nail (Shaaban, 2014) (a) Normalised centreline velocity, and (b) normalised static pressure.....	72
<i>Figure 39.</i> Numerical validation using normalised centreline velocity distributions of 2D space-filling positive square fractal grid $N = 4$ between turbulence model used in present work and experimental results (Mazellier & Vassilicos, 2010).....	73

<i>Figure 40.</i> Dimensionless temperature differences among different inserts (a) CO, (b) PSFG, and (c) NSFG at different tilting angles β	76
<i>Figure 41.</i> Thermal mixing performance among different inserts (a) CO, (b) PSFG, and (c) NSFG at different tilting angles β	77
<i>Figure 42.</i> Cross-sectional averaged turbulence kinetic energy among different inserts (a) CO, (b) PSFG, and (c) NSFG at different tilting angles β	81
<i>Figure 43.</i> Histogram for cross-sectional turbulence kinetic energy k at location $x / H = 2.6$ for different tilting angle β for CO (a-c), PSFG (d-f), and NSFG (g-i)	82
<i>Figure 44.</i> Cross-sectional $z / H = 0.5$ velocity streamline and turbulence kinetic energy in the thermal mixing chamber at for CO (a, b, e, f) and NSFG (c, d, g, h)	83
<i>Figure 45.</i> Tilting effect of space-filling inserts on the generation of flow recirculation velocity streamline (a, b) and turbulent kinetic energy k (c, d) in the lee of the inserts at $\beta = +45^\circ$ and $y / H = 0.5$	84
<i>Figure 46.</i> Dimensionless vertical velocity profiles at $z / H = 0.5$ for CO insert (a, b) and NSFG insert (c, d) at tilting angle $\beta = 0^\circ$ and $+45^\circ$	86
<i>Figure 47.</i> Vertical temperature profiles at $z / H = 0.5$ for CO insert (a, b) and NSFG insert (c, d) at tilting angle $\beta = 0^\circ$ and $+45^\circ$	87
<i>Figure 48.</i> Normalised pressure drop of each inserts over pressure drop of empty channel at $\beta = 0^\circ$, -45° , and $+45^\circ$	89
<i>Figure 49.</i> System performance η between CO and NSFG inserts.....	90
<i>Figure 50.</i> Numerical validation of centreline velocity downstream of each insert using (a) empty channel and circular orifice, (b) triangular orifice, (c) s1f1, and (d) s1f2. (Nicolleau et al., 2011)	97
<i>Figure 51.</i> Numerical validation using empty channel centreline velocity and centreline temperature downstream of the Tee joint test section.....	98
<i>Figure 52.</i> Numerical validation using centreline velocity in the lee of various insets (a) CO, (b) SO, (c) SFO, and (d) KSFO	99

<i>Figure 53.</i> Numerical validation using centreline temperature in the lee of various insets (a) CO, (b) SO, (c) SFO, and (d) KSFO	100
<i>Figure 54.</i> Dimensionless (a) average temperature θ and (b) temperature variation $\Delta\theta$ for the different inserts and smooth channel	103
<i>Figure 55.</i> Thermal mixing performance Θ for CO, SO, SFO, and KSFO insert in a Tee joint test section	104
<i>Figure 56.</i> Cross-sectional averaged turbulence kinetic energy among different inserts	107
<i>Figure 57.</i> Histogram for cross-sectional turbulence kinetic energy downstream of the insert at $x/H = 0.106, 0.731, \text{ and } 3.856$ for KSFO (a-c), SFO (d-f), CO (g-i), SO (j-l), and smooth channel (m-o)	108
<i>Figure 58.</i> Cross-sectional $z/H = 0.5$ velocity streamline (top four illustrations) and turbulence kinetic energy (bottom four illustrations) for the various inserts.....	109
<i>Figure 59.</i> Vertical dimensionless velocity profiles at $x/H = 0.106$ and 23.54 for all inserts and empty channel (control) at different $z/H =$ (a) 0.5 , (b) 0.25 , and (c) 0.125	111
<i>Figure 60.</i> Vertical dimensionless temperature profiles at $x/H = 0.106$ and 23.54 for all inserts and empty channel (control) at different $z/H =$ (a) 0.5 , (b) 0.25 , and (c) 0.125	112
<i>Figure 61.</i> (a) Pressure drop and (b) cross-sectional averaged pressure gradients of the various inserts and smooth channel	115
<i>Figure 62.</i> System performance among KSFO, CO, and SO inserts	116

CHAPTER 1 – INTRODUCTION

Mixing is an important process, of which its applications can be found in various kinds of industries, from food manufacturing, chemical bioreactor, to thermal management in heating, ventilating, and air-conditioning (HVAC), as well as engine combustions in motorised vehicles. In general, [Dimotakis \(2005\)](#) has categorised mixing into three categories. The simplest case being level-1 mixing where mixing is conducted passively without any change in chemical nor thermal characteristics of the fluid; level-2 mixing is coined as its attachment with dynamic effect, such as Rayleigh-Taylor instability flow, Richtmyer-Meshkov instability flow, mixing of different temperature or of different concentration, which causes a change in density of the fluid, thus gravitational effect may be included; level-3 mixing is associated with the change in fluid due to dynamic effects, such as combustion, detonation, increase in pressure, change in enthalpy, etc., may take place.

Hydrodynamic flow can be characterised as laminar and turbulent flow, which is differentiated by [Reynolds \(1883\)](#). The former has a characteristic of low Reynolds number which flow is fairly uniform, steady and has minimal interaction with other parallel streamlines, On the other hand, the latter generally has much higher Reynolds number where the local velocity fluctuates irregularly and chaotic. This promotes higher chance of interaction between different streamlines in flow. Hence, mixing can be achieved by the latter by the means of a turbulence generator. Turbulence generator can be of many different geometries and sizes, in planar or three-dimensional forms, as well as generated using active mechanised perturbation movement, or passive stationary objects. The geometry of a turbulence generator can also be tuned to suit various applications and conditions, however, limitations can likewise, be imposed due to the size to accommodate the turbulence generator, inlet flow speed, fluid properties, downstream flow condition, pressure drop, etc. Apart from the hydrodynamic aspect, other aspects such as the complexity to manufacture, the cost of production, etc. has to be taken into consideration when designing a turbulence generator.

Turbulence generator can be categorised into active and passive turbulence generator. Active turbulence generator produces turbulence by means of oscillating mechanical movement. Numerical study performed by [Sarkar and Schluter \(2014\)](#) with the excitation of two frequency on mixing boundary layer can be said to be catered for active oscillating turbulence generator. On the other hand, passive turbulence generator generates turbulence by forcing the flow of the fluid through space-filling plates and allows the blockage to generate wake turbulence leeward of the plate. Some examples of passive turbulence generator are grid type regular grid and fractal grid turbulence generator by [Suzuki, Nagata, Sakai, and Hayase \(2010\)](#), and orifice type turbulence generator by [Hashiehbf and Romano \(2013\)](#). These two types of turbulence generator will be compared in the present study.

Fractal was first coined by [Mandelbrot \(1983\)](#), whom had extensively studied the mathematical theory behind fractals. As illustrated in *Figure 1*, fractal is the repetition of a self-similar base geometry which subsequent iterations is reduced in size and follows a fixed pattern of arrangement. Numerous researchers have proposed the use of fractal to enhance various applications, including mixing enhancement and the understanding of the turbulence generated by fractal geometry. Some examples given are three-dimensional fractal stirrer by [Staicu, Mazzi, Vassilicos, and van de Water \(2003\)](#), as illustrated in *Figure 1(a)*, the study of turbulence generated of two-dimensional planar fractal grids by [Hurst and Vassilicos \(2007\)](#) in *Figure 1(b)*, (c), (d), the study of pressure drop across a two-dimensional planar fractal orifice by [Aly, Chong, Nicolleau, and Beck \(2010\)](#), as shown in *Figure 1(e)*, as well as many other remarkable researches into applying fractal geometry into hydrodynamic flow control.

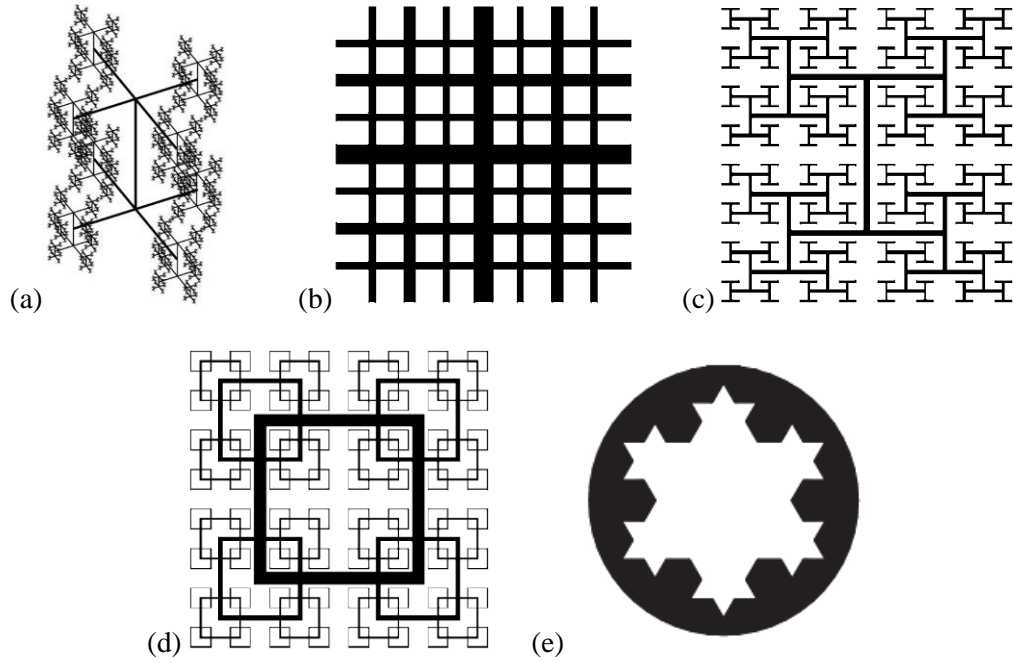


Figure 1. (a) Three-dimensional fractal object stirrer proposed by [Staicu et al. \(2003\)](#), (b – d) two-dimensional planar fractal grids proposed by [Hurst and Vassilicos \(2007\)](#), (e) two-dimensional planar fractal orifices (Koch snowflake) by [Aly et al. \(2010\)](#)

Besides grids type turbulence generator, i.e. fractal grids, many researches have also shown that orifice type turbulence generator is able to produce good mixing qualities. [Mi, Nathan, and Nobes \(2001\)](#) noted the jet formed by an orifice plate can produce good mixing rate when compared to a contoured nozzle and a pipe. Another study of using triangular orifice plate had been performed by [Azad, Quinn, and Groulx \(2012\)](#), and they also had noted the mixing performance of a triangular shaped orifice is better than a contoured orifice. Fractal applied orifice is as well studied by [Salim and Nicolleau \(2012\)](#), and is found that fractal orifice has its potential as an outstanding turbulence generator in mixing application. It would be more interesting to compare which of the two geometries would be superior in terms of mixing performance.

Numerical analysis is extensively employed in the present study to predict the best performing turbulence generator inserts for the thermal mixing of two streams. In Computational Fluid Dynamics (CFD), numerical study can be branched into direct numerical simulation (DNS), Reynolds averaged Navier-Stokes (RANS) turbulence models, i.e $k-\varepsilon$ model, Reynolds stress

model (RSM) and scale filter based large-eddy simulation (LES). The former explicitly resolves the Navier-Stokes equation at all scales, in both spatial scale, which ranges from integral scale to the smallest dissipative Kolmogorov microscales, and temporal scale. Hence, it is able to produce high fidelity solution for turbulence flow. On the other hand, RANS turbulence models, as its name suggested, is the averaged time component of the equation of motion for fluid flow. Furthermore, LES applies a scale filter to implicitly resolve the smaller spatial scale using turbulence models, i.e. Smagorinsky–Lilly model, while the larger scale above the scale filter is explicitly resolved with the DNS method.

DNS is the most preferable choice among researchers due to its high fidelity results. Nevertheless, employing DNS is not within easy reach of most researchers as it is computationally intensive and requires very high performance computing and costly resources, especially at the high Re regime. In order to cope with the computational resources, LES is employed to study the transient development of turbulence flow. Furthermore, three-dimensional steady-state incompressible analysis is done using the k - ε model and RSM.

Research Aims

Many researches have noted that by applying fractal onto turbulence generators, the nature of the turbulence can be tuned and altered to suit one's application and design. This research aims to benefit the HVAC system, particularly in free-cooling system (economiser). Referring to *Figure 2*, a free-cooling system works by drawing in cool recycled warm air from an air-conditioned room, mixing it with cooler fresh air, supplies it to a heat exchanger prior to sending back into the room. In a free-cooling system, the cool fresh air stream and warm recycled air stream is freely let to mix in a Tee-joint which join the two working fluids together. [L. Z. Zhang \(2009\)](#) and [Bury \(2012\)](#) noted that should there exist velocity and temperature mal-distribution after the mixing phase and the air is supplied to a cross-flow heat exchanger, the performance of the heat exchanger will deteriorate. Therefore, it is important to ensure the supplied air is as thoroughly mixed as it possibly can, while maintaining minimum velocity mal-distribution, to avoid or minimise energy wastage.

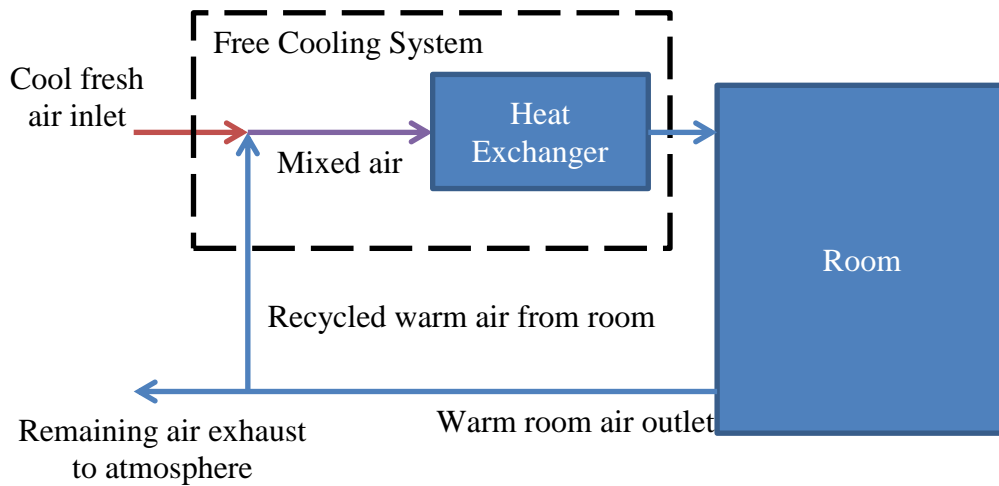


Figure 2. Free-cooling system in HVAC

Besides the benefit which could be gained in HVAC by this research, the present study could also explore new ideas for applications in other industries, i.e. manufacturing, chemical processes, etc. where two or more different temperature streams are required to be mixed in a long channel prior to the processes downstream of the channel. Hence, the present study research aims are listed as follow:

1. To compare the thermal mixing performance of symmetrical co-axial inlet of two air streams with temperature difference between grid type and orifice type inserts.
2. To compare the thermal mixing performance of asymmetrical inlet of two air streams with temperature difference between grid type and orifice type inserts.
3. To study the effect of tilting the inserts in asymmetrical inlet conditions.

Thesis Outline

The present study has adopted the numerical study approach in predicting the turbulence and mixing performance of planar fractal geometry. The thesis is structured to provide comparative results between fractal geometry of different configurations and under different inlet conditions.

The outline of the thesis is as follows:

CHAPTER 2: Literature Review

Previous research on the types of fractal turbulence generators, numerical methods, inlet conditions, and free-cooling systems are reviewed and presented within this chapter.

CHAPTER 3: Methodology

Numerical methods used in the present study and their validations with the experimental results are discussed in this chapter. Three phases are planned for the present study and their numerical setups are discussed in this chapter.

CHAPTER 4 - 6: Results and Discussion

Results from all three phases of the present study are presented and discussed meticulously in each of the chapters respectively. Numerically validated results will be discussed at the beginning of all the three phase. It is then followed by the numerically investigated results obtained in the studies as well as a brief summary of the chapters.

CHAPTER 7: Conclusions and Recommendations

Summarised conclusions of the present studies are presented in this chapter as well as future recommendations for improvement and possible applications in other industries.

CHAPTER 2 – LITERATURE REVIEW

Mixing

[Dimotakis \(2005\)](#) described mixing as the transport and diffusion of molecules induced by turbulence, from the largest to the smallest eddies. It would provide large interaction area which permits molecular mixing to take place. [Eckart \(1948\)](#) characterised turbulence mixing by turbulence as three-stage process of entrainment, dispersion, and diffusion, which spans the whole spatial and temporal scales of the flow. Three levels of mixing were described by [Dimotakis \(2005\)](#), namely level-1 mixing where mixing is passive scalar in nature. Furthermore, level-2 mixing can be described by level-1 mixing accompanied by dynamic effects. On another step higher, level-3 mixing associates level-2 mixing with change in the property of the fluid in terms of chemical composition, pressure, internal energy, etc.

Turbulence Generated by Three-Dimensional Fractal Object

Many researches have suggested on the possibility of exploiting fractal as turbulence generator inserts as a medium for mixing or stirring. One of the earlier experimental and numerical studies into employing fractal geometry in stirring application are by [Queiros-Conde and Vassilicos \(2001\)](#), [Mazzi, Okkels, and Vassilicos \(2002\)](#), and [Staicu et al. \(2003\)](#).

[Queiros-Conde and Vassilicos \(2001\)](#) experimentally studied the turbulence generated by 3D fractal grids (structure). The test section for the wind tunnel used in their study was 45.7cm in both width and height while the length was 176cm. Laminar inlet conditions was kept and the upstream background turbulence of the wind tunnel employed was measured at 0.6% in all test section. DANTEC (Denmark) constant temperature anemometer was employed in their study and data acquisition and analysis were carried out using Labview 5 at 100kHz (10ms/data) sampling frequency. *Figure 3* shows the schematics of the test section. Three 3D fractal structures were used with different fractal dimension $D_f = 2.05, 2.17, \text{ and } 2.75$. They compared the turbulence generated by fractal configuration, and found that the turbulence intensity was about $5\times$ higher than a classical grid, which was used in the validation of the test section earlier in the study. By

altering the fractal dimension D_f of a fractal object, the scaling of the turbulence could be changed.

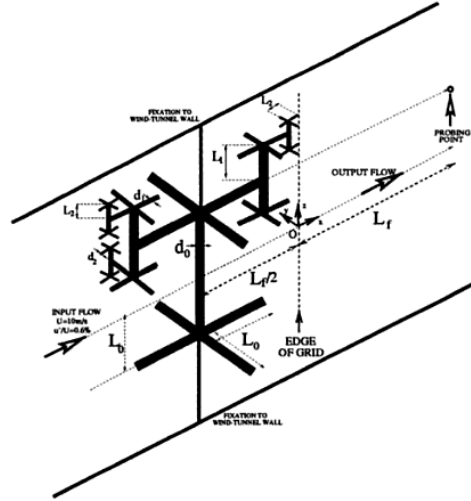


Figure 3. Test section with 3D fractal grid inserted by [Queiros-Conde and Vassilicos \(2001\)](#)

Numerical study was also carried out using shell-model to further understand the flow of energy among different wave-numbers in fully developed turbulence flow. This study was done by [Mazzi et al. \(2002\)](#). Power law forcing of Gledzer, Ohkitani, and Yamada (GOY) shell-model equation was employed in this study. The shell-models were simplified Navier-Stokes equations and validated using the same test section as in [Queiros-Conde and Vassilicos \(2001\)](#). Four different 3D fractal structures of $D_f = 2.05, 2.17, 2.40$, and 2.75 were employed and the fractal insert for $D_f = 2.05, 2.17$, and 2.40 consisted iterations $N = 4$ while $N = 5$ for $D_f = 2.75$. As with [Queiros-Conde and Vassilicos \(2001\)](#), the study by [Mazzi et al. \(2002\)](#) also suggested that fractal geometry could alter the turbulence scaling and dynamics, which in turns provide a new tool into the investigation of turbulence.

[Staicu et al. \(2003\)](#) employed three-dimensional fractal stirring object at three fractal dimensions $D_f = 2.05, 2.17$, and 2.40 . The dimensions of the wind tunnel employed in their study were $0.7\text{m} \times 0.9\text{m}$. Velocity measurements were taken using hot-wire probes at a distance downstream of the channel with 45 measurements arranged in a manner perpendicular to the flow and distributed

exponentially along the horizontal axis of the fractal object. Inlet condition ranged from $Re_\lambda = 175$ to 650 throughout the course of the study, where Re_λ was Re based on Taylor's micro-scale. Three types of measurement placement were made, which are diagonal, horizontally behind the upper lobe and lower lobe respectively. They observed that the turbulence generated by the fractal object is dependent on its orientation. Large-scale perturbation is almost not present when the fractal object was diagonally orientated, as the Re_λ was too low for the larger branch to make an impression. Fractal object $D_f = 2.17$ produced much stronger perturbation when compared to fractal object $D_f = 2.05$ closer to the centre of the object. Although in this study, the authors could not establish the distinctive feature influenced by fractal object on the generated turbulence, subsequent studies using simpler two-dimensional planar grids were done by the same research group to fill in the gap of understanding.

Hiramatsu, Kato, Ushijima, and Kitoh (2011) used Sierpinski tetrahedron to study the wakes generation. Sierpinski tetrahedron was a three-dimensional fractal configuration with a fractal dimension of 2. The authors noted the fractal object was able to generate comparatively high Re_λ due to the increase in turbulence intensities, despite the small scale wind tunnel.

Two-Dimensional Regular Grids, Planar Fractal Grids and Orifices

Turbulence generated by two-dimensional regular grid, or also known as, biplane square grid, had been extensively studied in the past. It was known that this least complex geometry had enabled extensive development of turbulence theories (Antonia, Lee, Djenidi, Lavoie, & Danaila, 2013; Comte-Bellot & Corrsin, 1966; Khan & Joshi, 2015) Murzyn and Belorgey (2005). conducted experimental study of using regular grid placing in a free flow surface to investigate the basic characteristic of the turbulence. The authors noted the turbulence intensity increases significantly immediately in the lee of the grid, followed by a rapid decay to a constant at about $15\times$ of the mesh size distance. They also observed that the fluctuation downstream from the channel was about 25% higher than the undisturbed flow.

Following the footsteps of their previous research in three-dimensional fractal objects, the same research group began their study into the turbulence generated by two-dimensional planar fractal grids.

Hurst and Vassilicos (2007) had experimentally studied the scaling and decay using 21 sets of two-dimensional planar fractal grids of different fractal dimensions and base geometries. *Figure 1(b), (c), and (d)* are derived from three patterns as shown in *Figure 4* respectively. Two wind tunnels were used throughout the course of this experimental study. One was a recirculating wind tunnel having a cross-section of $T = 0.91^2 \text{ m}^2$ and 4.8m in length, while the other was an open circuit wind tunnel with cross-section of $T = 0.46^2 \text{ m}^2$ and 3.6m in length. The background turbulence for both wind tunnels were measured at 0.25% and 0.4% respectively. Hot-wire probe was utilised to measure velocity throughout the study. They noted turbulence generated by generic fractal were strongly dependent on its fractal dimension $D_f \leq 2$, its effective mesh size M_{eff} , and its ratio of the largest to the smallest bar thickness $t_r = t_{max} / t_{min}$. Furthermore, at a relatively low blockage ratio $\sigma = 25\%$, fractal grids were able to generate flow with higher turbulence intensities as compared with classical grids of higher blockage ratio. They also observed that the turbulence intensity peaks at a distance leeward of the grid x_{peak} , and followed by decaying exponentially [further studies performed later by Valente and Vassilicos (2011) do not support this statement].

$$M_{eff} = \frac{4T^2}{P_f} \sqrt{1 - \sigma} \quad \text{Eqn. 1}$$

where T^2 is the cross-section area of the wind tunnel, P_f is the fractal perimeter length of the grid, and σ is the blockage ratio.

$$\sigma = \frac{A}{T^2} \quad \text{Eqn. 2}$$

where A is the filled area of the grid.

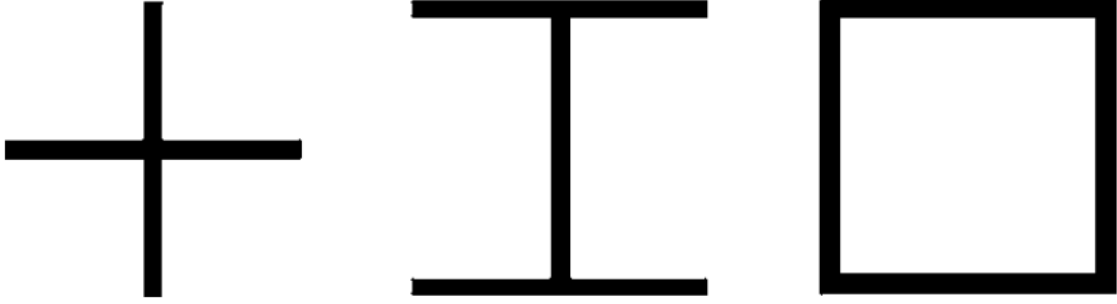


Figure 4. Fractal generating patterns extracted from [Hurst and Vassilicos \(2007\)](#)

[Seoud and Vassilicos \(2007\)](#) had conducted experimental study on the space-filling fractal grids as suggested by [Hurst and Vassilicos \(2007\)](#). All the experimental apparatus were similar. In this study, [Seoud and Vassilicos \(2007\)](#) agreed with the fact that both the Taylor microscale λ and integral length scale stayed relatively constant after the peak of turbulence intensity x_{peak} for all of the three space-filling square fractal grids (SFG) employed in their study. These length-scales were independent of fractal grid configurations and inlet velocity U_∞ . Moreover, upon decay the turbulence generated by these grids was homogeneous and isotropic in nature, and remains into a single length-scale. The authors could not establish what influenced the single length-scale decay, but they hinted the way the fractal was constructed may have caused this phenomenon. In addition, a notable observation made by the authors is the non-Kolmogorov $-5/3$ energy spectra was observed in the turbulence generated by these grids.

[Mazellier and Vassilicos \(2010\)](#) conducted a continuation study of [Seoud and Vassilicos \(2007\)](#). In their study, the authors established the wake interaction length scale (*Eqn. 3*) and the location of peak turbulence intensity (*Eqn. 4*),

$$x_* = \frac{L_0^2}{t_0} \quad \text{Eqn. 3}$$

$$x_{peak} \approx 0.45x_* \quad \text{Eqn. 4}$$

where L_0 is the length of the largest bar and t_0 is the thickness of the largest bar. More details on the method of measurement on the bar length and thickness is shown in *Figure 5(a)*. *Figure 5(b)* and (c) showed the SFG for $N = 4$ and 5 respectively. The turbulence intensity at the peak separated the two turbulence regimes of different nature, the turbulence generating domain and

the turbulence decaying zone. They noted that the turbulence generating domain was inhomogeneous and the velocity fluctuation did not follow a Gaussian manner. Conversely, after the peak, the decaying turbulence was fairly homogeneous and also followed a fairly Gaussian fluctuation. Moreover, the ratio of L_u / λ to Re_λ (L_u is the longitudinal integral length scale) remains constant throughout the decay regime, unlike turbulence decay exhibited in regular grid. Hence, this had led the authors to believe the nature of the turbulence generated by fractal grids did not follow Richardson-Kolmogorov cascade. This new finding was also published in *Physical Review Letters* by [Stresing, Peinke, Seoud, and Vassilicos \(2010\)](#).

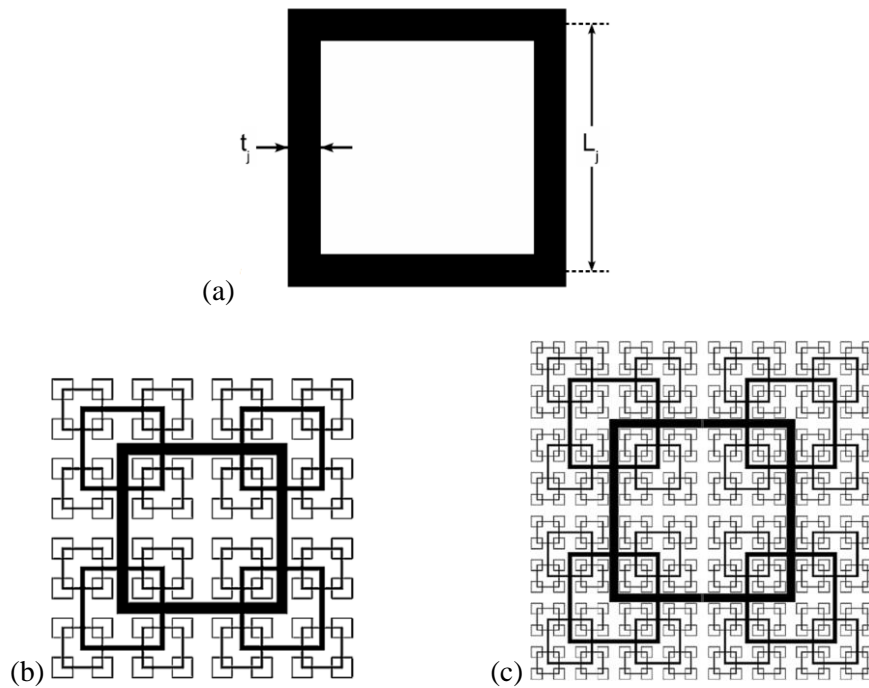


Figure 5. (a) Bar length L_i and bar thickness t_i used in the space-filling square fractal grids; (b) and (c) illustrates square fractal grid $N = 4$ and $N = 5$ used in the investigation by [Mazellier and Vassilicos \(2010\)](#)

[Geipel, Goh, and Lindstedt \(2010\)](#) conducted experimental study using five different configurations of fractal cross grids inserts in opposed jet geometry. *Figure 6* shows the experimental setup used in their study and *Figure 7* depicts the fractal cross grids, similar to one of the fractal grids used in the study by [Hurst and Vassilicos \(2007\)](#). LaVision Flowmaster 3-

particle image velocimetry (PIV) was used to record the axial and radial velocity components. Two 120mJ Solo-New Wave double pulsing Nd:YAG lasers illuminated the central plane perpendicular to the nozzle with a thickness of between 0.5mm to 2.5mm. The authors noted the turbulence had increased of more than 100% with the use of fractal grids at the nozzle outlet with anisotropy perturbation downstream of the system, although the turbulence was isotropy upstream of the nozzle outlet. High blockage ratio from one of the grids configurations could produce the highest turbulence intensity, but at the expense of lesser uniform radial perturbation.

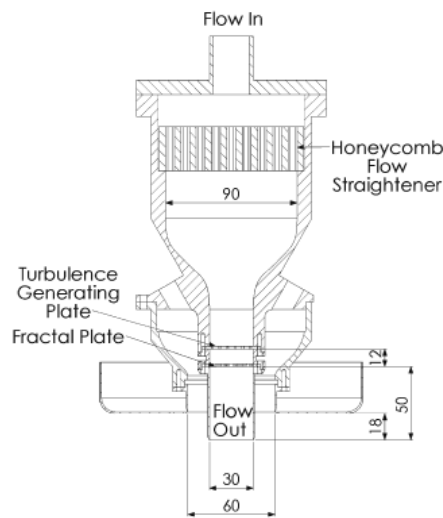


Figure 6. Schematic of the experimental apparatus used in [Geipel et al. \(2010\)](#)

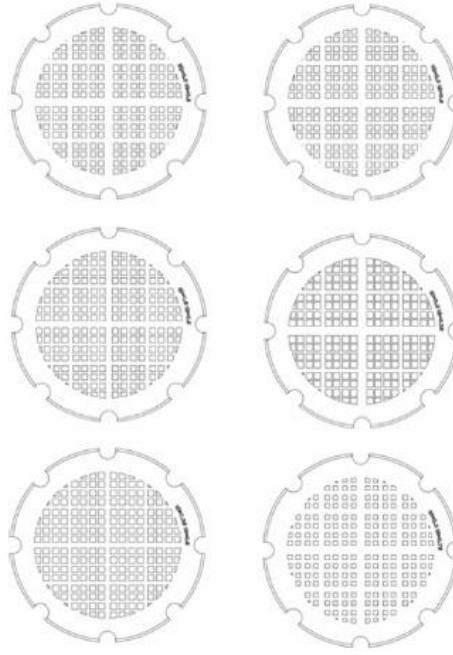


Figure 7. Fractal cross grids used by [Geipel et al. \(2010\)](#)

One of the first look into mixing using turbulence generated by SFG, which was conducted by [Hurst and Vassilicos \(2007\)](#), was done by [Suzuki, Nagata, Sakai, and Ukai \(2010\)](#). They studied experimentally the turbulence generated by two types of regular grid and SFG in a water channel with a cross-section of $0.1^2\text{m}^2 \times 1.5\text{m}$ in length. SFG used in their study was similar to the SFG $N = 4$ used by [Hurst and Vassilicos \(2007\)](#), whilst two regular grids of same t_r were constructed using round and square rods respectively. PIV method was used to measure the velocity of the perturbation generated by the grids and planar laser-induced fluorescence (PLIF) was used to measure the instantaneous concentration field. Rhodamine B was used as the fluorescent dye, and was excited by a 532nm continuous laser wave. The excited fluorescent dye was captured using a Nikon D700 single-lens reflex camera. A schematic of the experimental setup is shown in *Figure 8*. The authors confirmed the velocity fluctuation is much greater in SFG compared to regular grid, as shown in *Figure 9*. *Figure 10* presents the fact that the mixing was more stimulated by SFG, compared to the regular grid.

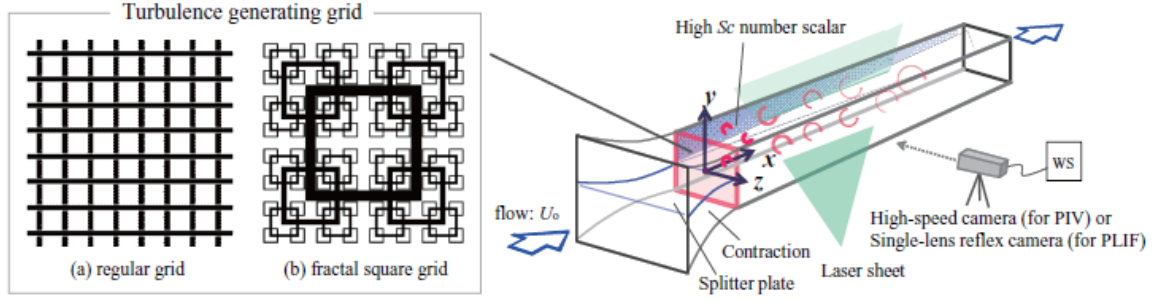


Figure 8. Experimental setup by Suzuki, Nagata, Sakai, and Ukai (2010)

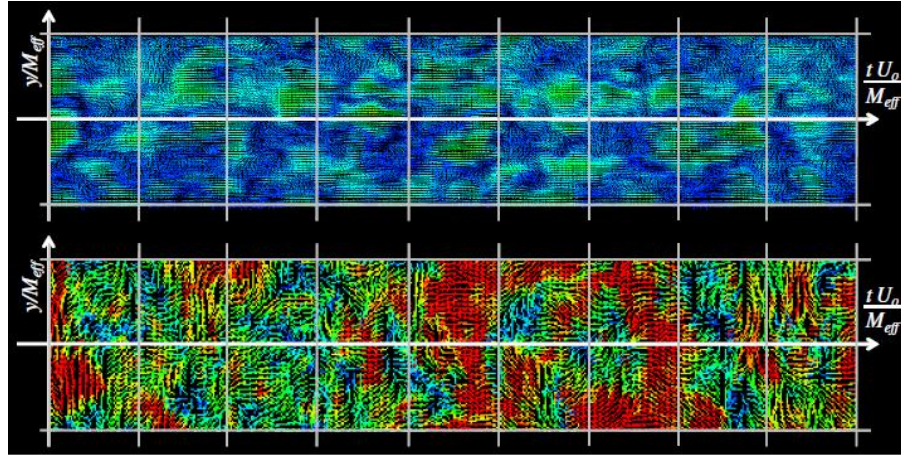


Figure 9. Instantaneous fluctuating velocity vector field for regular grid (top) and SFG (middle), $|\mathbf{V}| = 0.1$ (red), $|\mathbf{V}| = 0.05$ (green), $|\mathbf{V}| \approx 0.0$ (blue) as extracted from Suzuki, Nagata, Sakai, and Ukai (2010)

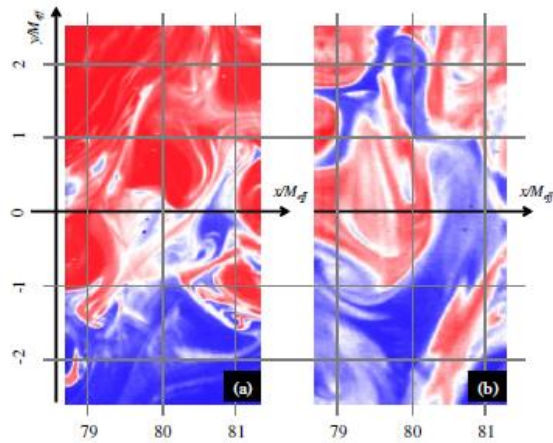


Figure 10. Instantaneous scalar fields turbulence by (a) regular grid and (b) SFG by Suzuki, Nagata, Sakai, and Ukai (2010), $\tilde{c} = 1$ (red), $\tilde{c} = 0.5$ (white), and $\tilde{c} = 0$ (blue)

Suzuki, Nagata, Sakai, and Hayase (2010) conducted DNS to numerically study the mixing effect in turbulence generated by regular and fractal grids of the same blockage ratio σ . SFG of $t_r = 5.0$ and 8.5 were used in this study. Two non-dimensioned temperature streams separated at half cross-sectional length formed the inlet conditions. Initial condition of $Re_M = 2500$ (Re_M represents Re at M_{eff}) and Prandtl number Pr was set at 0.71. The authors noted turbulence generated by SFG tested in their study was able to induce mixing to a higher degree compared to regular grid, as shown in *Figure 11* and *Figure 12*.

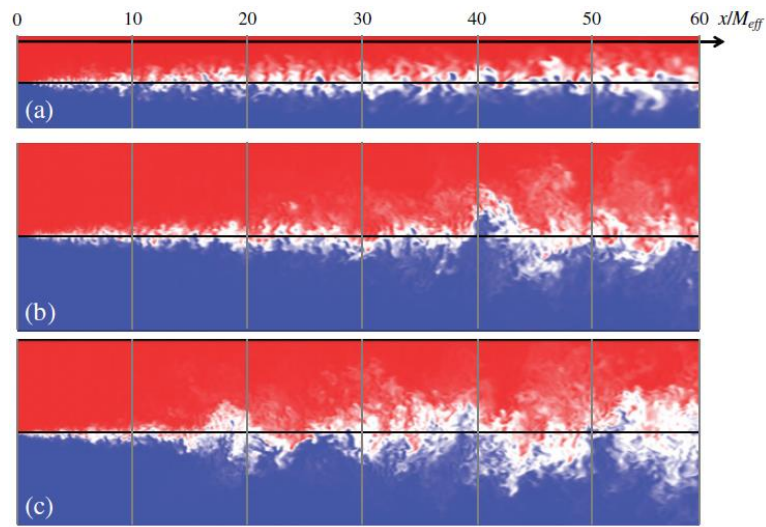


Figure 11. Instantaneous temperature fields in (a) regular grid, (b) $N = 4$ SFG $t_r = 5.0$, and (c) $N = 4$ SFG $t_r = 8.5$ by Suzuki, Nagata, Sakai, and Ukai (2010); non-dimensioned temperature of $\hat{T} = 1$ (red), $\hat{T} = 0.5$ (white), and $\hat{T} = 0$ (blue)

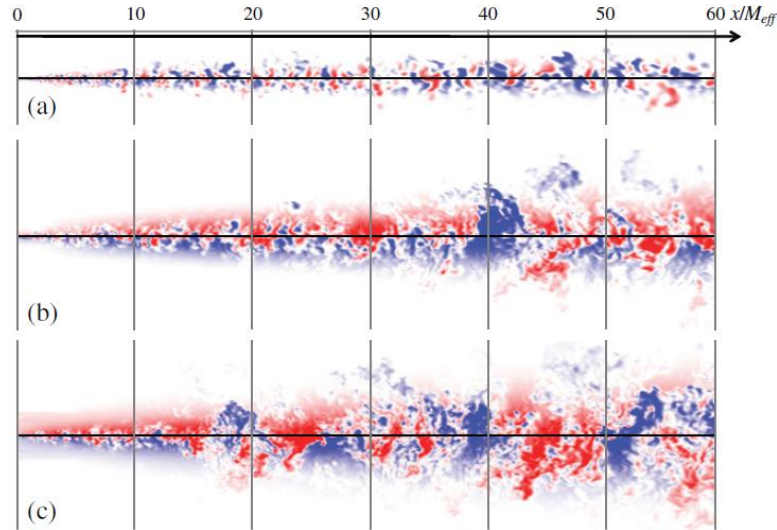


Figure 12. Instantaneous fluctuating temperature fields in (a) regular grid, (b) $N = 4$ SFG $t_r = 5.0$, and (c) $N = 4$ SFG $t_r = 8.5$ by [Suzuki, Nagata, Sakai, and Ukai \(2010\)](#); non-dimensioned temperature of $\theta = 0.3$ (red), $\theta = 0$ (white), and $\theta = -0.3$ (blue)

Another type of fractal geometry in the form of orifice was proposed by [Aly et al. \(2010\)](#) as shown in *Figure 1(e)*. They experimentally studied the pressure drop across the fractal-shaped orifice in a pipe. The authors observed that with the introduction of fractal in the design of the orifice, it could influence the pressure drop across the inserts. Fractal-shaped orifice resulted in lower pressure drop compared to circular orifice of similar blockage area. It was also reported by [Shaaban \(2014\)](#) that by installing a ring downstream of the orifice plate, the pressure drop across the orifice plate (i.e. an orifice meter) could be reduced by 31% to 33%.

[Laizet and Vassilicos \(2011\)](#) numerically studied and compared the turbulence flow of a regular grid with three different square fractal grids using DNS. They concluded that: (i) the vorticity field of the square fractal grids were more erratic and grouped together, compared that to a regular grid, (ii) prolonged higher vorticity and turbulence intensity were generated by square fractal grids than regular grid, (iii) the geometrical features were able to propagate further downstream of the channel for turbulence generated using square fractal grids as compared with regular grids, the results were presented as shown in *Figure 13*, (iv) it is confirmed that square fractal grids were able to generate two regimes of turbulence downstream of the channel, i.e.

turbulence continually intensified in the lee from the grids until reaches to a peak followed by decaying thereafter, (v) dominant small wakes induced by the smallest scales near the grid was produced before subsequent smaller turbulence frequencies were activated by interaction with larger wakes.

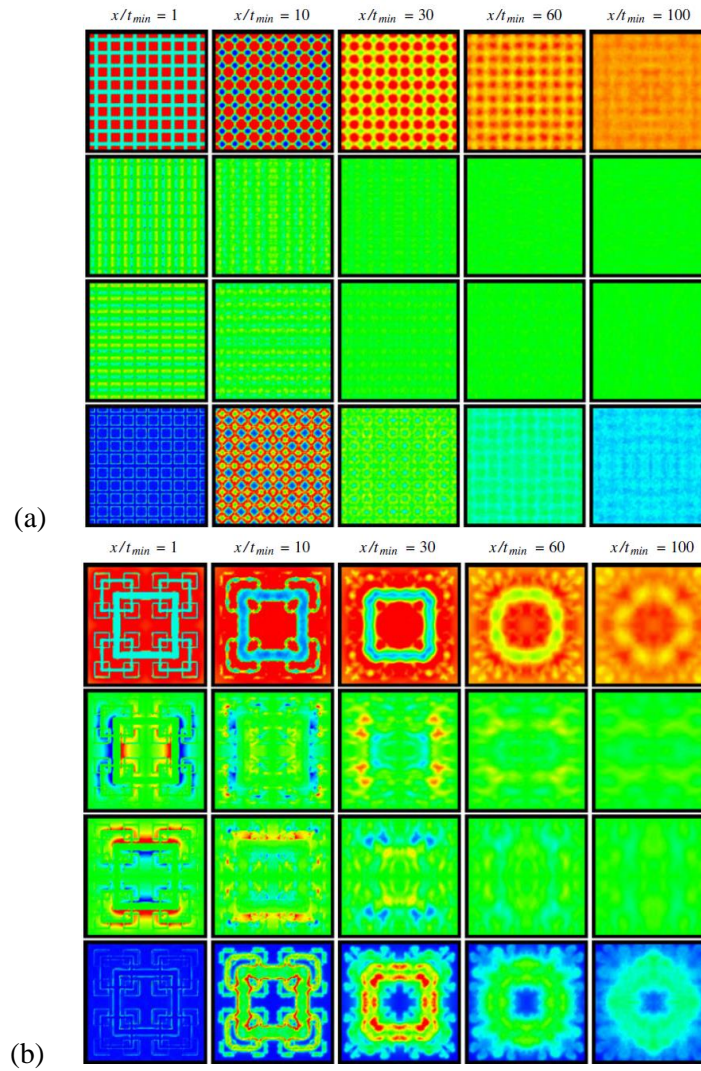


Figure 13. Downstream evolution of U / U_∞ , V / U_∞ , W / U_∞ , and $(u'^2)^{1/2} / U_\infty$ (top to bottom) for (a) regular grid, and (b) space-filling square fractal grid $t_r = 5$, $N = 4$, from Laizet and Vassilicos (2011)

The experimental study by Valente and Vassilicos (2011) was the continuation of the previous studies undertaken by the same research group in square fractal grids. The key areas being

studied were the effect of spatial resolution upon data recording, the analysis of the homogeneousness of flow in the decay region, and looking at the energy spectra in directionally dependent method, as opposed to previous analysis in using isotropy method. The turbulence decayed almost homogeneously after $x / x_* \approx 0.6$ and in such a way that L_u / λ was about constant while the Re_λ decreases up to the furthestmost measurable distance downstream. Meanwhile, the increment of Re_0 led to L_u / λ being increased as well. This observation led the authors to believe single-scale self-similar form could better describe turbulence generated by SFG, compared to [Kolmogorov \(1941\)](#) phenomenology. This study confirmed the abnormal high power-law decay exponents, but disproved the turbulence decayed in an exponential manner at the decay regime, both of which were noted previously by [Hurst and Vassilicos \(2007\)](#) and [Mazellier and Vassilicos \(2010\)](#).

At a later stage, an experimental study of SFG in water tunnel was performed by [Gomes-Fernandes, Ganapathisubramani, and Vassilicos \(2012\)](#), using PIV. The experimental setup is illustrated in *Figure 14(a)* and the detailed construct of the SFG used in their investigation as shown in *Figure 14(b)*. The imaging apparatus used in their investigation were two CCD cameras with 2048×2048 pixel resolution, aided by a double-pulsed Nd:YAG laser capable of 200mJ/pulse to illuminate the flow. The laser was set at 1.04Hz as sampling frequency and focused at the mid-plane of the channel's cross-section. The authors concluded that the study with an improved wake interaction length scale as *Eqn. 5* (previously defined by [Mazellier and Vassilicos \(2010\)](#) as *Eqn. 3*),

$$x'_* = \frac{L_0^2}{\alpha C_d t_0} \quad \text{Eqn. 5}$$

where α represents the free-stream turbulence intensity and length scale parameter, C_d is the drag coefficient, L_0 is the length of the thickest bar, and t_0 is the thickness of the thickest bar. The location of the peak previously defined by [Mazellier and Vassilicos \(2010\)](#), was also redefined as *Eqn. 6*,

$$x'_{peak} = 0.21x'_* = 0.21 \frac{L_0^2}{\alpha C_d t_0} \quad \text{Eqn. 6}$$

They also noted the perturbations in the lee of the grids grown faster when the inlet possesses free-stream turbulence, when compared to inlet with laminar flow. This could influence the location of peak turbulence intensity downstream, which was taken into account in *Eqn. 6* as the parameter α . As with previous studies, they also identified that the turbulence is isotropy in nature and in terms of energy dissipation, the ratio of L_u / λ to Re_λ remained constant with decreasing Re_λ downstream from x_*^{peak} to $3x_*^{peak}$.

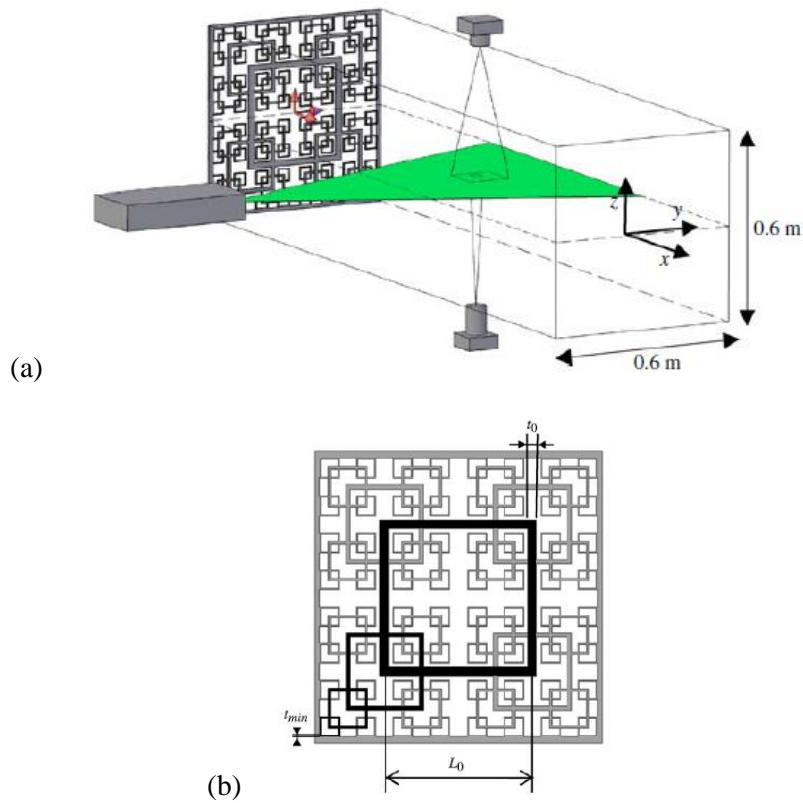


Figure 14. (a) An illustration of the water tunnel PIV set up and (b) detailed schematic for the construct of space-filling fractal grid used by [Gomes-Fernandes et al. \(2012\)](#)

Table 1. Space-filling square fractal grids geometry details used in [Gomes-Fernandes et al.](#)

(2012), dimensions in millimetre (mm)

Grid	SFG8	SFG13	SFG17
N	4	4	4
t_r	8.5	13.0	17.0
t_0	17.5	21.0	23.5
t_{min}	2.1	1.6	1.4
L_0	302.9	303.2	303.3
σ	25.3	25.0	25.0

[Laizet and Vassilicos \(2012\)](#) reported on the influence of space-scale unfolding (SSU) mechanism in the turbulence generated by SFG, as illustrated in *Figure 15*, each bar thickness generated different length scales corresponding to their bar thickness and length. When looking at the furthest length scale x_* , all four wakes will be able to meet each other. They also noted that due to the SSU mechanism, scalar transfer and turbulent diffusion could be improved, whilst the pressure drop was reduced. As a result, the authors suggested that this new understanding could deeply affect the integrative fractal design into new mixing and cooling enhancement for use in numerous industrial application.

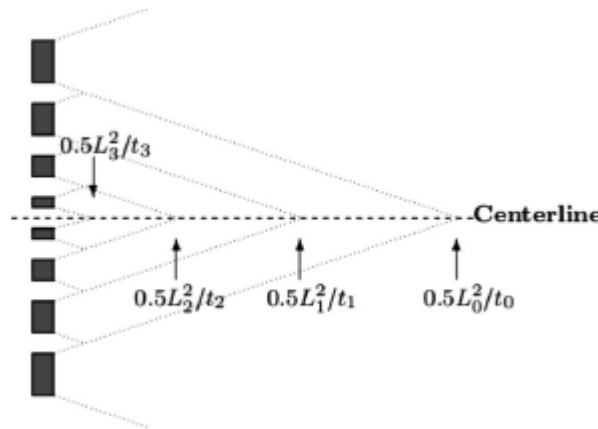


Figure 15. Schematic of space-scale unfolding mechanism (SSU) mechanism by [Laizet and Vassilicos \(2012\)](#)

[Salim and Nicolleau \(2012\)](#) experimentally studied the turbulence generated by fractal orifice as shown in *Figure 16*. Hot-wire anemometry was used to collect velocity in the wind tunnel. The

internal diameter of the wind tunnel was 140.8mm, with wall thickness of 5mm, and length of 4400mm. Based on the time correlation and energy spectra of the turbulence generated by fractal orifice, it was indicated that fractal orifice performed better in terms of mixing efficiency as compared to the classical circular orifice.

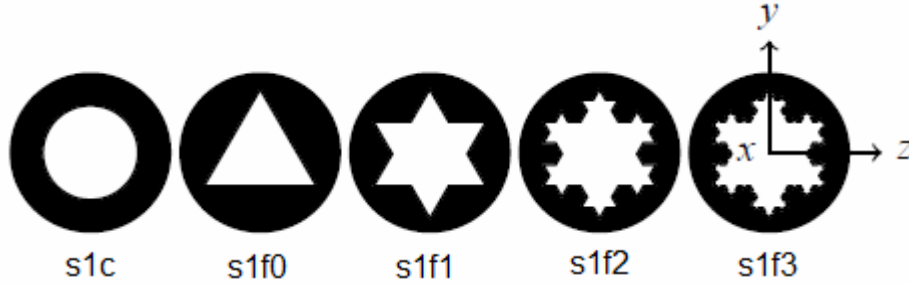


Figure 16. Orifice plate (s1c) and evolution of fractal orifice plate (s1f0 to s1f3) by [Salim and Nicolleau \(2012\)](#)

[Nagata et al. \(2013\)](#) conducted the experimental study of turbulence generated by SFG in a wind tunnel of cross-section of $T = 300^2 \text{ mm}^2$, and 3800mm in channel length. The background turbulence of the wind tunnel was reported to be lower than 0.65%. Inlet velocity was set to correspond with $Re_M = 5900$ and 11400. Through this investigation, the authors supported the works of [Mazellier and Vassilicos \(2010\)](#) that the classical scaling of $L_u / \lambda \sim Re_\lambda$ and Richardson-Kolmogorov cascade were not applicable to all boundary-free weakly sheared/strained turbulence.

[Soulopoulos et al. \(2013\)](#) experimentally studied the burning premixed flame enhanced by turbulence generated by SFG. Figure 17 shows the $N = 3$ SFG used in their study, with $L_0 = 36.8\text{mm}$ and $t_0 = 2.7\text{mm}$, which resulted in blockage ratio $\sigma = 0.22$. The authors noted the turbulence generated by SFG promoted higher burning rate by 40% as well as increased surface area of the flame compared to square grid, which operated at same flow rate and stoichiometry.

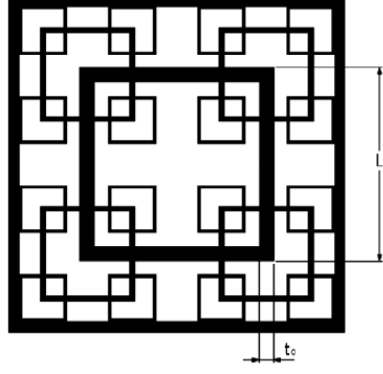


Figure 17. Diagram of $N = 3$ SFG used by Soulopoulos et al. (2013)

Via DNS, Suzuki et al. (2013) conducted the numerical study of turbulence generated by SFG with the geometrical t_r and σ which are different from previous studies (Hurst & Vassilicos, 2007; Mazellier & Vassilicos, 2010; Nagata et al., 2013). Their results showed the position of x_{peak} was approximately $0.45x_*$, which fell within the range reported in the previous study (see Table 2). The authors confirmed the turbulence velocity fluctuated almost constantly for integral length scales distributed in both stream-wise and transverse direction. k_c for the turbulence induced by SFG follows a power-law function and its integral length scales remains constant.

Table 2. SFG parameters and x_{peak} by Suzuki et al. (2013)

	D_f	N	σ	t_r	x_* / L_0	x_{peak} / x_*
Present (run 1)	2	4	0.36	8.5	7.5	0.42
Present (run 2)	2	4	0.36	15	7.5	0.54
Present (run 3)	2	4	0.44	8.5	9.4	0.53
Mazellier and Vassilicos (2010)	2	4, 5	0.25	8-17	12.4-19.8	0.45
Hurst and Vassilicos (2007)	2	4, 5	0.25	2.5-17	12.4-22.2	0.33-0.49
Nagata et al. (2013)	2	4	0.25	13	14.0	0.45

Cafiero, Discetti, and Astarita (2014) experimentally studied the effect of turbulence generated by $N = 3$ SFG for the heat transfer enhancement of impinging jet on a smooth surface. Its performance was compared with the regular grid. The temperature distributions were recorded using infra-red camera (FLIR SC6000), capable in capturing 640×512 pixel. The authors reported that with the use of SFG, it showed an improvement in local heat transfer rate over

regular grid, although, a reduction in the uniformity of Nusselt number Nu on the heated surface was identified.

Numerical Methods for CFD

DNS is a class of CFD which provides high-fidelity solution in the prediction of turbulent flows as it explicitly resolves the Navier-Stokes equation directly. However, there are many limitations hindering the use of DNS for many researchers. Firstly, the computational cost required increases with increasing Re . It was reported that by doubling Re , the computational cost increases by a factor of $11\times$ (Coleman & Sandberg, 2010). Despite its requirement in extraordinary computational cost, there are researchers who are able to attain such significant resources to support the study using DNS.

Laizet and Vassilicos (2009) successfully conducted DNS to simulate the turbulence generated by fractal grids by employing immersed boundary method and terascale parallel high performance computing. All computations were done on HECToR high performance computer. Following the research investigation reported by Laizet, Lamballais, and Vassilicos (2010), they successfully employed a parallelised version of Incompact3D DNS scheme where the numerically calculated results agreed with early experimental data. In addition, a total of 15,300 computational cores were used in Laizet and Vassilicos (2012) numerical studies. Hence, the computational resource of such level is in general cannot be easily available for a vast majority of researchers around the world.

Hence, CFD simulations based on the computational models simplified through assumptions made upon its derivation, e.g. the (i) RANS based $k-\epsilon$ model, (ii) Reynolds stress model (RSM), as well as (iii) hybrid LES-RANS detached eddies simulation (DES), or even the (iv) large eddies simulation (LES) which resolved iteratively the larger scales (similar to DNS) but employing filtering method to filter out smaller scales, are able to indirectly reflect the hydrodynamic of various behaviours (Khan & Joshi, 2015; Kumar, 2015; Zheng, Nicolleau, & Qin, 2012).

Free-cooling system in HVAC

Airside free-cooling system, or otherwise known as economiser, is one of the effective solutions in reducing the total power consumption of HVAC cooling system. (Rackes & Waring, 2014) Free-cooling system works by redrawing the heated air, mixing it with cooler surrounding air, and recirculates it through an air-conditioning system prior to sending the reconditioned air back into the room. (Shehabi et al., 2009) This configuration had proven to considerably reduce the energy usage, thus enable one to save the cooling cost. (Siriwardana, Jayasekara, & Halgamuge, 2013) It is reported that by coupled with optimised strategies, the airside free-cooling system is able to save up to 29% of the yearly energy consumption. (H. N. Zhang, Shao, Xu, Zou, & Tian, 2014)

CHAPTER 3 –METHODOLOGY

The whole project was split into three phases to realise the aims of this research.

PHASE 1: Thermal mixing enhancement of a co-axially inlets with a 2D space filling inserts.

PHASE 2: Thermal mixing enhancement after a *T*-duct with a 2D space filling insert.

PHASE 3: Thermal mixing enhancement after a *T*-duct with a fractal orifice insert.

Validation of turbulence models

The turbulence models employed throughout this research were realisable $k-\varepsilon$ model, Reynolds stress model, and to a certain extent, large eddies simulation (LES). It is important to validate the numerical results with the experimental results in order to gain a better confidence with the numerical understanding. ANSYS FLUENT 14.0/14.5 (USA) were used throughout the present study in solving for the above mentioned turbulence models.

Validation were carried out using experimental results by [Mazellier and Vassilicos \(2010\)](#) and [Morrison et al. \(1993\)](#). Many studies conducted in the past raised the issue by which the turbulence generated from SFG did not completely follow the classical understanding of turbulence ([Mazellier & Vassilicos, 2010](#); [Nagata et al., 2013](#)). Hence, it is important for this validation to take place so to ensure the currently available turbulence models could still predict the turbulence generated by SFG to a certain degree of accuracy.

First and foremost, 3D models were created using Dassault Systèmes SolidWorks Education 2013-2014 (France) as according to the wind tunnel test section in [Mazellier and Vassilicos \(2010\)](#) and [Morrison et al. \(1993\)](#). *Figure 18* shows the assembled SolidWorks models for both the SFG17 $N = 4$ with thickness of 5mm insert and a cuboid which represents the air space for the interior of the test section in the wind tunnel. The dimensions for the 5mm thick SFG17 insert can be found in *Table 3* and the dimensions for the cuboid air space were $460 \times 460 \times 5050 \text{ mm}^3$. The centre of the 5mm SFG17 insert was situated 50mm from the inlet, as shown in *Figure 19*. The resulted meshing holds about 1.12×10^6 of elements.

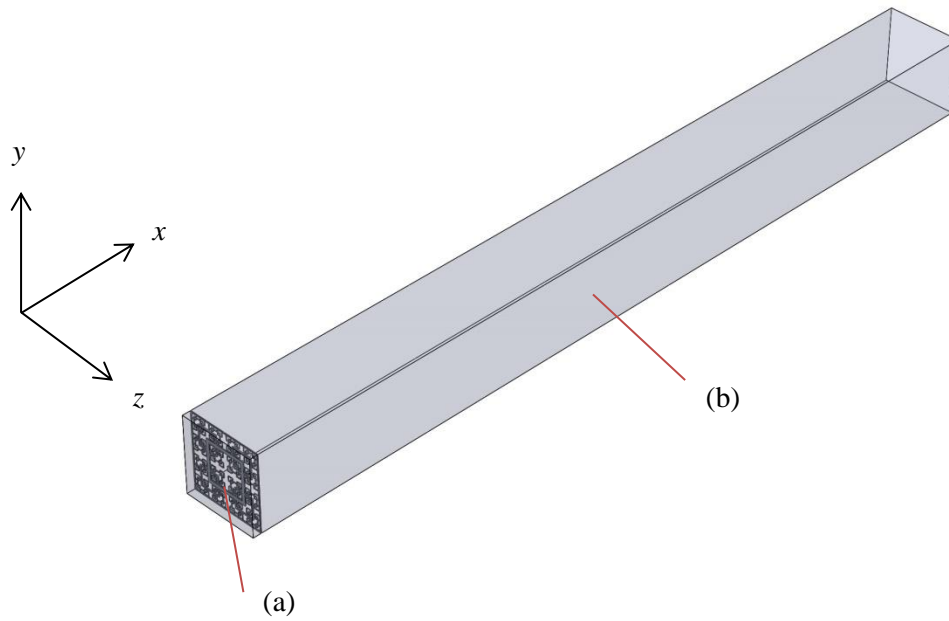


Figure 18. SolidWorks models of (a) SFG17 space-filling plate insert and (b) interior air space of the wind tunnel test section from Mazellier and Vassilicos (2010)

Table 3. Geometry of space-filling square fractal grids used by Mazellier and Vassilicos (2010),

dimensions in millimetre (mm)

	SFG8	SFG13	SFG17	BFG17
N	4	4	4	5
L_0	237.5	237.7	237.8	471.2
L_1	118.8	118.9	118.9	235.6
L_2	59.4	59.4	59.5	117.8
L_3	29.7	29.7	29.7	58.9
L_4	-	-	-	29.5
t_0	14.2	17.2	19.2	23.8
t_1	6.9	7.3	7.5	11.7
t_2	3.4	3.1	2.9	5.8
t_3	1.7	1.3	1.1	2.8
t_4	-	-	-	1.4

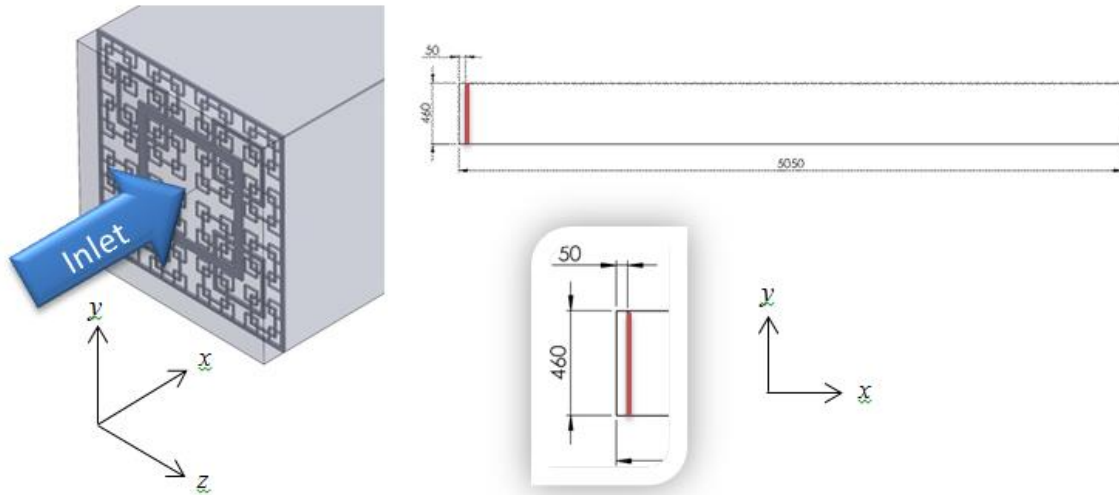


Figure 19. Close up view of the SFG17 insert in the cuboid air space (left), dimension for the cuboid air space (top right) and location of the SFG17 insert (bottom right)

An assumption was made that the inlet to Mazellier and Vassilicos (2010) wind tunnel test section was a fully developed flow, taking the shape of a parabolic velocity distribution profile. Hence, another cuboid of length $460 \times 460 \times 20,000 \text{ mm}^3$ was modelled to acquire this parabolic velocity distribution profile. The inlet velocity was set at 4.1m/s and the background turbulence intensity was set at 10%. Then, the velocity, turbulence kinetic energy at the outflow was collected and saved. The saved profile took the shape of a parabolic distribution, which typically found in a fully developed flow, and had centreline velocity of $U_c \approx 5.2\text{m/s}$. This profile was then imported into the M&V 2010 case.

Two turbulence models were setup in FLUENT for validation with M&V 2010, which were (i) steady-state pressure-based solver using RSM, and (ii) transient pressure-based solver using LES. Inlet turbulence intensity was set at 10% as well as the coupling of velocity and pressure was implemented using SIMPLEC algorithm. Grid independent test were done using steady-state RSM with increasing number of mesh elements up until the simulated result for centreline velocity were within 5% different of previous mesh density (number of mesh elements). Numerical results for the highest mesh density case were compared with experimental results from M&V 2010 using U_c/U_p . For transient LES numerical calculations, the realisable $k-\varepsilon$ model

was initially employed to simulate an initial steady-state solution. The method and boundary conditions for set up was the same as the steady-state RSM. The turbulence model is then replaced by transient LES model. A total time of 3s was run with time step of 5×10^{-6} , resulting in a total of 6×10^5 steps in total. After the initial transient simulation using LES, further 1 second (2×10^5 steps) was performed with data captured in every interval of 2 milliseconds, i.e. 400 steps.

Next, standard $k-\varepsilon$ and RSM was validated with the experimental results from MDNP 1993 orifice insert. *Figure 20* shows the overall numerical setup as accordance to MDNP 1993's experimental setup. The diameter of the air space volume inside the test section was 50.4mm (2 inch) and the length upstream and downstream of the insert were $5\times$ and $10\times$ the diameter of the air space volume respectively. Thickness of the insert was 1.59mm with an orifice in the middle measuring 25.4mm (1 inch) and bevelled 45° on one side, which resulted in a blockage ratio of 0.5 (see *Eqn. 2* for method of calculation for blockage ratio). The resulted mesh had 1.1×10^5 elements. Another cylindrical air space volume of similar diameter and 5m in length was modelled to simulate the parabolic velocity profile of a fully developed flow. The resultant centreline velocity of the parabolic profile U_C was about 82m/s. The profile was then input as the inlet of the test section and inlet turbulence intensity was set at 1%. Finally, the simulated results were compared with experimental results using U_C / U_{max} and $(P - P_{out}) / (P_{in} - P_{out})$.

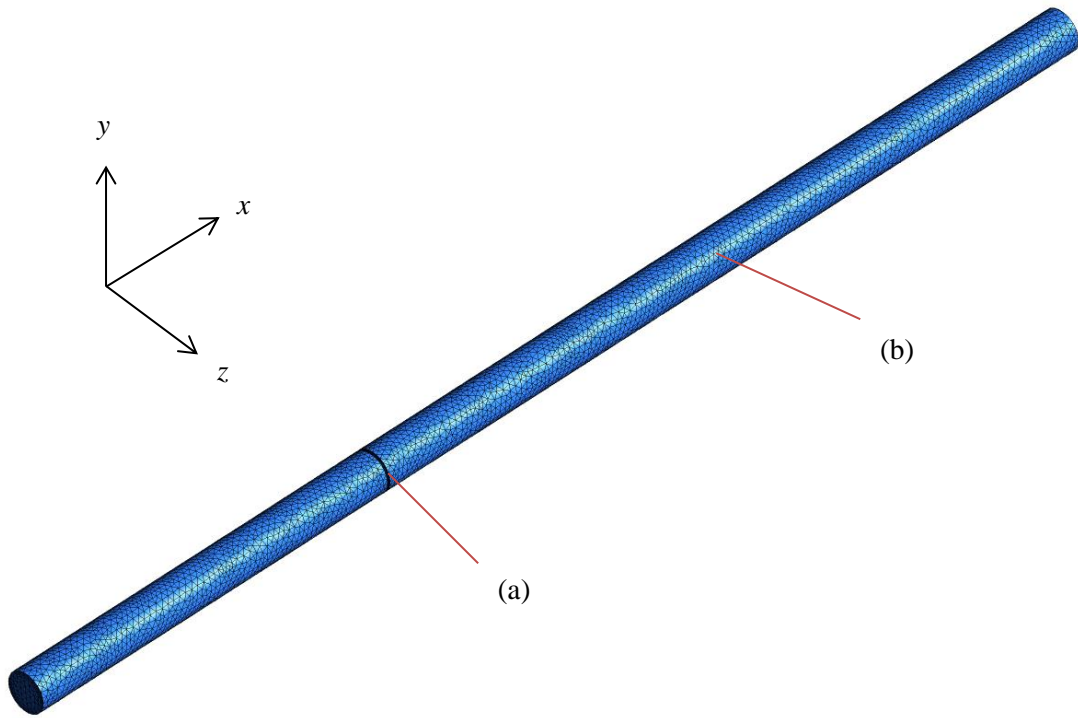


Figure 20. Numerical setup as accordance to the experimental setup in [Morrison et al. \(1993\)](#)

Numerical simulation

PHASE 1: Thermal mixing enhancement of a co-axially inlets with a 2D space filling inserts

To start off with the present study, the thermal mixing performance using two sets of turbulence generator inserts were evaluated, namely grid type and orifice type inserts. First, the test section was modelled out in SolidWorks and the resultant 3D drawing was later import into ANSYS Workbench (USA) for pre-processing. The computational domain of the test section takes the form of a cuboid with cross-section of $160 \times 160 \text{ mm}^2$ and length of 4,140mm. A small cuboid of $40 \times 40 \text{ mm}^2$ and 50mm in length protruded out at the inlet side of the test section and was co-axially placed to the test section. The purpose of this small protrusion was to facilitate the injection of warm air inlet into the test section, whilst the area surrounding the protrusion on the main test section was the cool air inlet. This configuration was to enable the evaluation of thermal mixing performance using the turbulence generated by different designs and thicknesses with symmetrical co-axial inlets of two different temperatures. Next, the inserts comprised of (a) regular grid (RG), (b) square fractal grids (SG), and circular orifice (CO) were modelled out, as shown in *Figure 22*. The black area of the grids in *Figure 22* represents the space-filling blocked areas whilst the rest were unfilled areas and air was allowed to pass through the inserts. All inserts were $160 \times 160 \text{ mm}^2$ to completely fill the interior of the computational domain. The spacing between the bars for RG was 19.7mm and the thickness of the bar was 4.3mm. Dimensions for SG at $N = 3$ were $L_0 = 91.43\text{mm}$, $L_1 = 45.71\text{mm}$, and $L_2 = 22.86\text{mm}$, with bar thickness $t_0 = 10\text{mm}$, $t_1 = 5\text{mm}$, as well as $t_2 = 2.5\text{mm}$. The diameter for CO cut-out was 141.97mm. Two insert thicknesses were modelled out for all RG, SG, and CO, which were $\delta = 5\text{mm}$ and 40mm , to study the effect of thickness on the turbulence generated and thermal mixing performance. All inserts have about the same blockage ratio at $\sigma = 0.38$. All inserts were placed at 170mm from the warm air inlet (or 120mm from the cool air inlet), measuring from the midpoint of the thickness of the inserts (see *Figure 21* for more details).

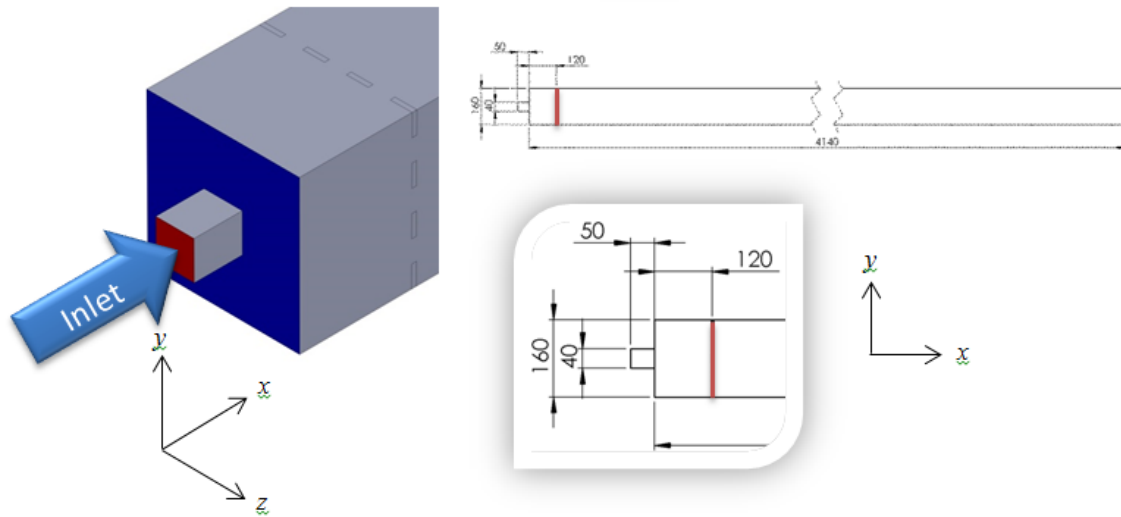
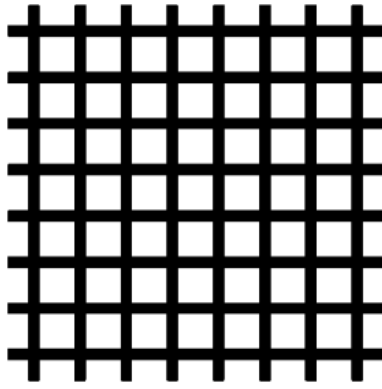
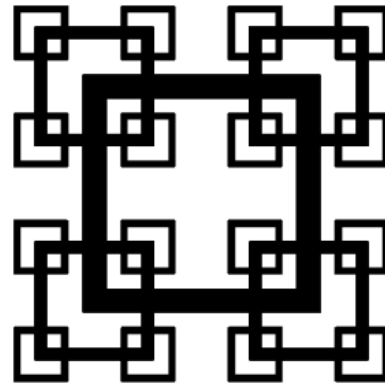


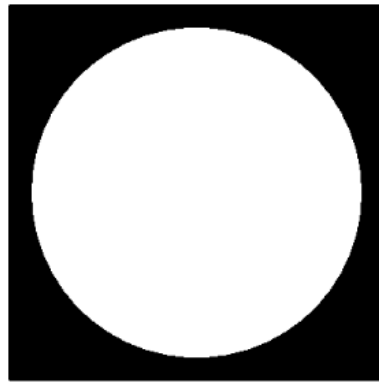
Figure 21. Schematic of computational domain and the dimensions for PHASE 1 study, the coloured faces at the inlet represent warm air inlet (in red) and cool air inlet (in blue)



(a) RG



(b) SG



(c) CO

Figure 22. Illustration of $160 \times 160 \text{ mm}^2$ turbulence generator inserts (a) Regular Grid (RG), (b) Square Fractal Grid (SG), and (c) Circular Orifice (CO); black area represents filled-space whilst the rest are spaces which allows air to pass through

Pre-processing was done using ANSYS Workbench built-in meshing program and solved by FLUENT 14.0. Mesh independent tests were carried out for all the inserts as well as an empty channel for further comparison at a later stage. The density of the mesh (number of mesh elements) was increased gradually until the difference in calculated centreline velocity differed less than 5% from the previous mesh density. The resulted number of mesh elements for Empty Channel (EC), RG-5, RG-40, SG-5, SG-40, CO-5, and CO-40 were tabulated in *Table 4* (values are rounded to 3 significant numbers). Steady-state RSM simulation was set using of boundary conditions for both inlets as in *Table 5* and SIMPLEC scheme was selected for pressure-velocity

coupling and residual criteria were set as default at 10^{-3} for all parameters. Velocity profiles for both inlets are left as default, i.e. uniform profile.

Table 4. Number of mesh elements for each case in PHASE 1

Cases	Number of elements (rounded)
EC	1.72×10^6
RG-5	1.16×10^6
RG-40	1.15×10^6
SG-5	1.16×10^6
SG-40	1.15×10^6
CO-5	9.59×10^4
CO-40	3.35×10^5

Table 5. Boundary conditions set for all cases in PHASE 1

Parameter	Values
Warm air inlet velocity	2.5m/s
Cool air inlet velocity	2.5m/s
Warm air inlet temperature	308.15K (35°C)
Cool air inlet temperature	298.15K (25°C)
Inlets turbulence intensity	1%

Moving on, the results for all cases were compared to gauge the effect of different insert thicknesses on all cases leeward from the inserts. Key comparison parameters were defined as normalised centreline velocity U_C / U_∞ , maximum cross-sectional temperature difference $\Delta\theta$, thermal mixing performance Θ , and turbulence kinetic energy of various inserts normalised to turbulence kinetic energy of EC k_{norm} .

$$\theta = \frac{T_H - T_{A,ave}}{T_H - T_C} \quad \text{Eqn. 7}$$

$$\Delta\theta = \frac{T_{A,max} - T_{A,min}}{T_H - T_C} \quad \text{Eqn. 8}$$

$$\Theta = \frac{T_H - T_{A,ave}}{T_{A,max} - T_{A,min}} \quad \text{Eqn. 9}$$

$$k_{norm} = \frac{k_{A,ave}}{k_{A,ave,EC}} \quad \text{Eqn. 10}$$

Continuing on, the pressure drop across the insert ΔP were obtained and an overall system performance η were made.

$$\Delta P = P_{in} - P_{out} \quad \text{Eqn. 11}$$

$$\eta = \frac{\Theta}{\Delta P} \quad \text{Eqn. 12}$$

Apart from the quantitative analyses, diagonal stream-wise 2D cross-sections for streamline velocity, temperature distribution, and turbulence kinetic energy were also assessed. Temperature distributions as well as the histogram for turbulence kinetic energy for comparison between the two best thermal mixing inserts were taken at a few interval distances leeward of the inserts.

On the other hand, transient LES calculations were conducted to study the fluctuations of the turbulence generated by the best performing type of insert. Initially, realisable k - ε conditions were employed to simulate a steady-state initial prediction. Boundary conditions were set as the same as in RSM cases. Then the turbulence model was switched to transient LES. Total time of 3s was simulated with time step of 5×10^{-6} second, which was 6×10^5 steps in total. Later on, an additional of 2×10^5 steps (1 second) was calculated and data was captured at every interval of 400 steps (2 millisecond) upon LES numerical modelling.

PHASE 2: Thermal mixing enhancement after a *T*-duct with a 2D space filling insert

The flows of methodology for the present phase was similar to those in phase one. First and foremost, the 3D model of the test section was modelled out using SolidWorks, as well as the planar inserts. The test section for this phase differed from the previous phase by an additional “*T*” (Tee) joint to link the two inlets of different temperature. The resultant flow was an asymmetrical flow inlet prior to the turbulence generating insert. Cross-section of the whole test section was $160 \times 160 \text{ mm}^2$ and the length for the main channel was 4,000mm end-to-end. An additional shorter secondary branch inlet was joined at a distance 620mm and the $\delta = 20\text{mm}$ turbulence generating insert was situated 1,120mm from the inlet of the main channel. Detailed schematic for the test section and the location of the insert can be found in *Figure 23*. Numerical results from phase one suggest that the length of the blockage area was an important trait in the designs of a turbulence generating insert which is capable of inducing good thermal mixing performance.

Three turbulence generating inserts were used in the present study and presented in *Figure 23*, namely (a) positive square fractal grid $N = 3$ (PSFG), (b) negative square fractal grid $N = 3$ (NSFG), and (c) circular orifice (CO). The dimensions for the grids can be found in *Table 6*. It is worth mentioned that the bars are designed to “grown” inwards to the squares for NSFG, a slight difference from original PSFG model. Three tilting configurations were considered, in which $\beta = 0^\circ$ and $\pm 45^\circ$. The resulted blockage ratio for PSFG was 0.314 whilst 0.692 for both NSFG and CO at $\beta = 0^\circ$, and $\sigma = 0.515$ for PSFG, 0.782 for NSFG and CO at $\beta = \pm 45^\circ$. The space-filling area for NSFG was just the inverse of PSFG, where the area of the air was able to flow through the insert was the opposite between the two inserts.

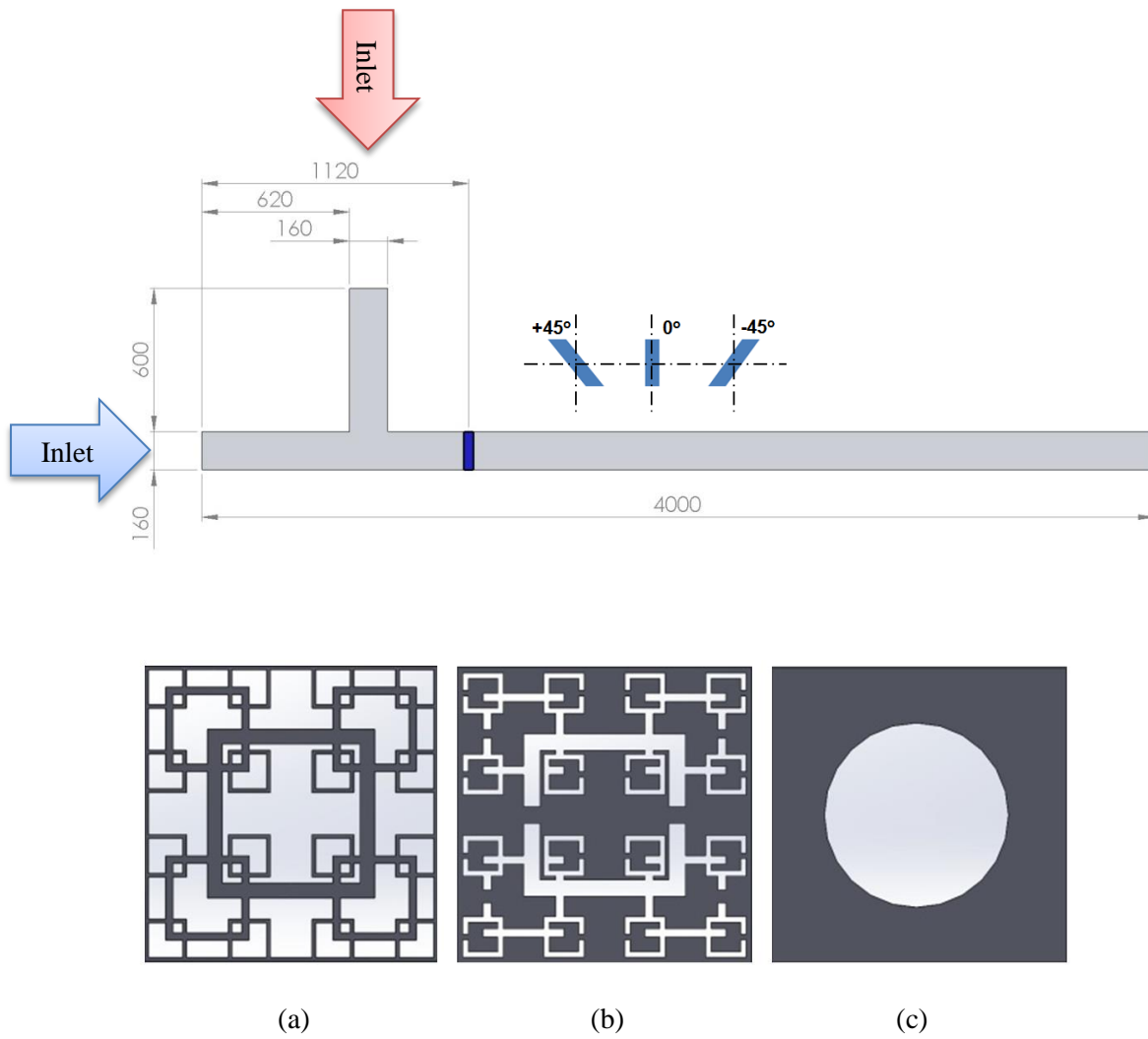


Figure 23. Dimensions for test section employed in PHASE 2 (top), and the inserts (a) positive square fractal grid (PSFG), (b) negative square fractal grid (NSFG), and (c) circular orifice (CO)

Table 6. Dimensions for inserts used in PHASE 2

Grid	PSFG	NSFG	CO
L_0	91.4mm	88.0mm	-
L_1	45.7mm	44.0mm	-
L_2	22.9mm	22.0mm	-
t_0	8.0mm	9.0mm	-
t_1	4.0mm	6.0mm	-
t_2	2.0mm	3.0mm	-
D_0	-	-	100.2mm

3D steady-state, incompressible turbulence and thermal mixing of the inserts were numerically simulated using k - ε turbulence model. Grid independent test were conducted which result in the number of elements of about 1.03×10^6 for all cases. Boundary conditions for the present study were as follow: velocity for both inlets were set at 2.5m/s, followed default uniform distributed inlet profile with 5% inlet turbulence intensity, temperature were set at 300K for the inlet of the main channel and was 320K for the inlet of the branched channel. Convergence criteria were set at 10^{-3} for mass balance, velocities, k and ε , whilst 10^{-6} for energy. Methods of analysing the thermal mixing performance are similar to phase one.

PHASE 3: Thermal mixing enhancement after a T-duct with a fractal orifice insert

The numerical validation of the $k-\varepsilon$ turbulence model was compared with the experimentally measured centreline velocity reported by [Nicolleau et al. \(2011\)](#), using the various orifice inserts in their studies, i.e. smooth channel, circular orifice, triangular orifice, s1f1, and s1f2, of which all having the same blockage ratio $\sigma = 0.66$. Hence, a cylindrical flow test section was modelled with diameter of 140.8mm, and velocity inlet conditions of 5m/s. It is important to note that the experimental results were collected using high sensitivity and accuracy hotwire anemometry device.

Besides the numerical validation against experimental results from other research groups, a wind tunnel was constructed (see *Figure 24*) to validate the simulated results of a Tee-inlet using $k-\varepsilon$ turbulence model coupled with energy equation. Two streams of different temperature were joined in a ‘Tee’ prior to the insert. The insert was situated 433mm downstream from the Tee-joint. The wind tunnel cross-section area was $160 \times 160 \text{ mm}^2$ and it had a total length of 4,906.6mm and inlet length prior to the Tee-joint was 490mm. The wind tunnel was constructed with 10mm thick clear acrylic with thermal conductivity of $0.17\text{W/m}\cdot\text{K}$. Air was drawn in by an axial fan (Kruger MD200, Singapore) with built-in flow controller, and the fan was situated at the outflow of the wind tunnel. The inlet velocities at both inlets were kept at around 1.9m/s to 2.0m/s. Two bell-mouth inlets were placed at each of the inlets respectively as well as a 3kW electrical finned air heater was situated at the inlet which was perpendicular to the main channel, before the bell-mouth, to provide warm air inlet representing the warm inlet air in a HVAC free-cooling system, which was controlled at about 35°C while the horizontal inlet was maintained at ambient temperature in the room. Air velocity and temperature were recorded using a velocity probe (TESTO 445, Germany) of accuracy $\pm 0.03 \text{ m/s}$ and $\pm 0.3^\circ\text{C}$. Six velocities and temperature readings were taken simultaneously at time step of 10 seconds.

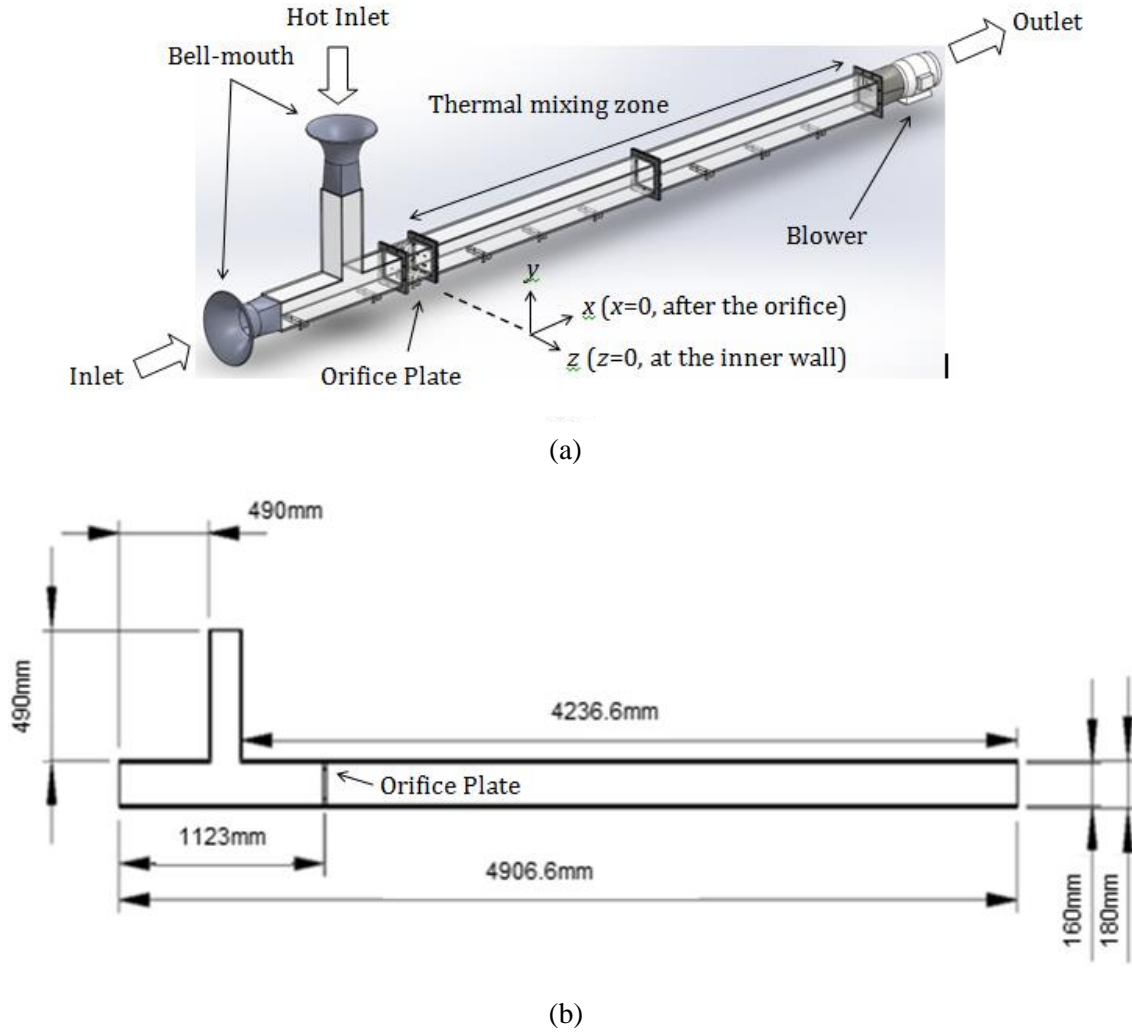


Figure 24. (a) Schematic for the wind tunnel test section experimental setup, and (b) its dimensions

From the understanding gained from phase one and phase two, of which orifice type inserts could generate better thermal mixing enhancement and overall system performance. Hence, the current study focused on using such orifice insert in generating hydrodynamic flow. Turbulence was generated using two sets of inserts, one set of orifices for control (APS, Acrylonitrile Butadiene Styrene induced, $0.17\text{--}0.19\text{ W/m}\cdot\text{K}$) and another set of fractal orifices (Delrin, $0.3\text{ W/m}\cdot\text{K}$), namely, (i) Square orifice (SO), (ii) circular orifice (CO), (iii) square fractal orifice $N = 3$ (SFO), and (iv) Koch snowflake fractal orifice $N = 3$ (KSFO). All fractal orifice inserts are shown in Figure 25 (i-iv). Blockage ratio for all cases was fixed at 0.5 and thickness of inserts at $\delta =$

20mm. SFO comprised of self-duplicating squares arranged in a fashion similar to PSFG in phase one, except the square were “cut-out”, with $L_{max,SFO} = 85.02\text{mm}$ and $L_{min,SFO} = 13.74\text{mm}$. Similarly for KSFO, equilateral triangles “cut-outs” were made to form the orifice, with $L_{max,KSFO} = 112.16\text{mm}$ and $L_{min,KSFO} = 25.08\text{mm}$, and the duplicated “cut-out” were made at the midpoint of each sides. Detailed dimensions for the inserts can be found in *Table 7*. Experimental centreline velocities were collected along the lee from the inserts to be verified with present numerical calculations.

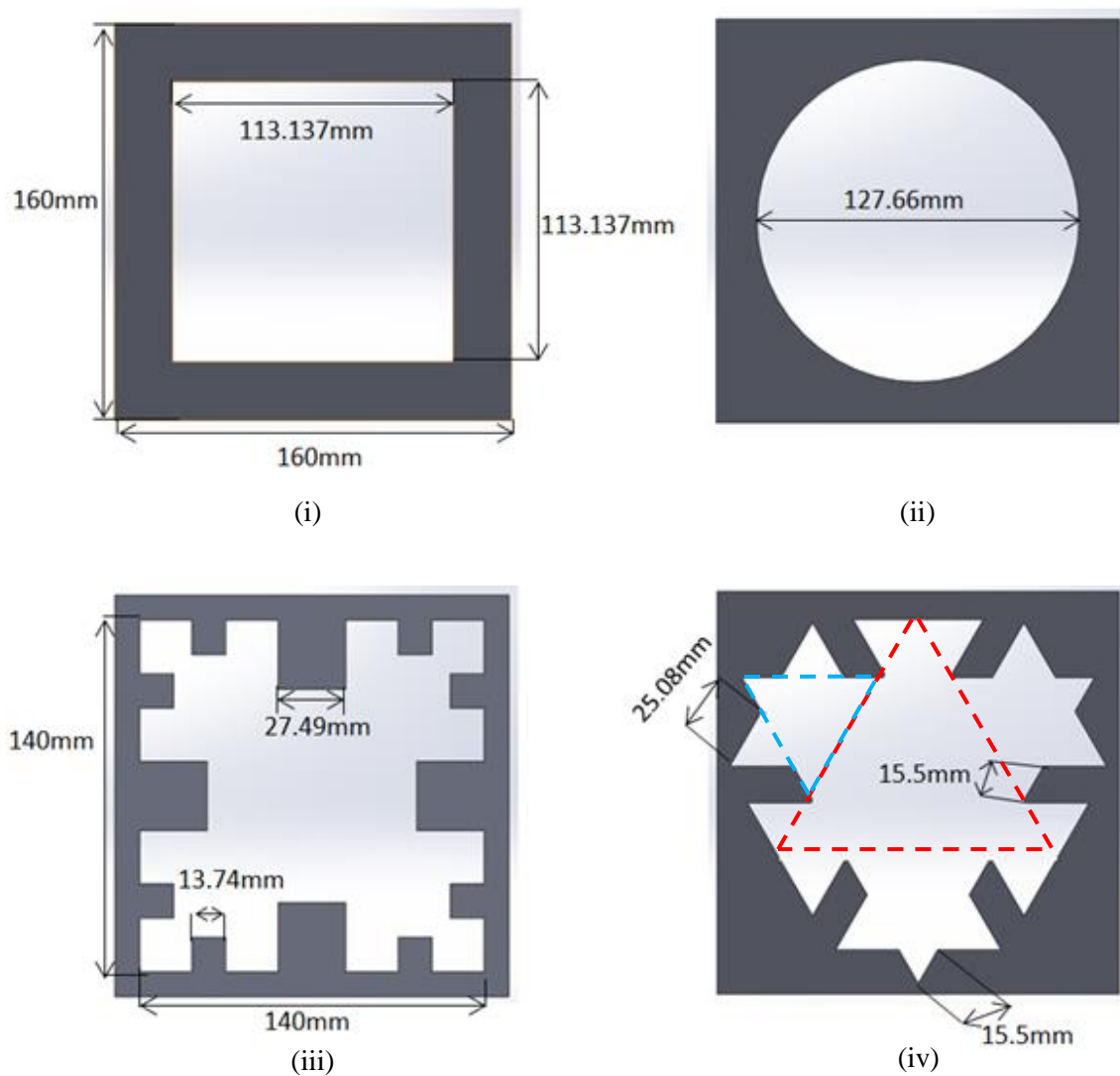


Figure 25. (i) Square orifice (SO), (ii) circular orifice (CO), (iii) square fractal orifice, (iv) Koch fractal orifice (KSFO); red dotted line represents triangle “cut-out” at $N = 1$ and cyan dotted line represents $N = 2$

Table 7. Dimensions for regular orifices and fractal orifices

Grid type	N	D_{eq} (mm)	$L_{max}, I = 1$ (mm)	Length at $I = 2$ (mm)	$L_{min}, i = 3$ (mm)
SO	1	144.05	113.14	-	-
CO	1	127.66	127.66	-	-
SFO	3	318.32	85.02	27.49	13.74
KSFO	3	256.46	112.16	56.08	25.08

Following on, the numerical study was conducted using $k-\varepsilon$ turbulence model and compared with experimental result. Grid independent test were performed for all cases, which were SO, CO, SFO, KSFO, and smooth channel. The resulted computational domain was about 2.0×10^6 elements with tetrahedral grids, and further emphasis around the 20mm inserts were made using higher resolution mesh. Convergence criteria for all cases except KSFO were set at 10^{-4} for mass balance, velocities, k and ε , whilst 10^{-6} for energy. For the case of KSFO, second order accuracy was used with the exception of energy equation for the simulation carried out. Convergence criteria for mass balance, velocities, k and ε were set at 10^{-3} and energy at 10^{-6} . The method of result analysis was similar to the previous phases.

CHAPTER 4 – RESULTS AND DISCUSSION : PHASE 1

Thermal mixing enhancement of a co-axially inlets with a 2D space filling inserts

This chapter presents the results for phase one of the present studies. To start off the studies of this project, it is easier and clearer to evaluate the effectiveness of thermal mixing using different insert designs with symmetrical temperature differential inlets. By identifying which type of inserts could give the best thermal mixing performance and the working mechanism which contributes to the enhancement, these information could contribute towards more insights when giving constructive suggestions toward the next phase of studies.

Validation of numerical results

3D, steady-state incompressible RSM and transient LES models were validated against the experiment results acquired by [Morrison et al. \(1993\)](#) and [Mazellier and Vassilicos \(2010\)](#). The former studied the flow field for the turbulence generated by an orifice insert, whilst the latter investigated the turbulence generated by a 2D planar $N = 4$ square fractal grid. *Figure 26* shows the variation between numerical simulations for steady-state RSM and transient LES with experimental results at various points taken downstream of the insert. Steady-state RSM (solid circle) shows very close agreement with the experimental results. Although the results for transient LES seems to differ from experimental results, it is worthy to note that the blue diamond in *Figure 26* actually indicates the average velocities of the whole numerical duration i.e., 1 second, and the bars represents the standard deviation of the velocity fluctuation, which representing the extent of insert induced velocity fluctuations. Wider bar could indicate how large a fluctuation, i.e. wider bar indicates a higher velocity fluctuation and vice versa for the shorter one.

As a result, the calculated centreline velocity obtained via LES modelling is in close agreement with experimental results before $x / x_* = 0.2$ when the fluctuation is small. Likewise for numerical validation against [Morrison et al. \(1993\)](#) experimental data, the result suggests that steady-state

RSM is as well in good agreement with experimental data for both centreline velocity and pressure predictions.

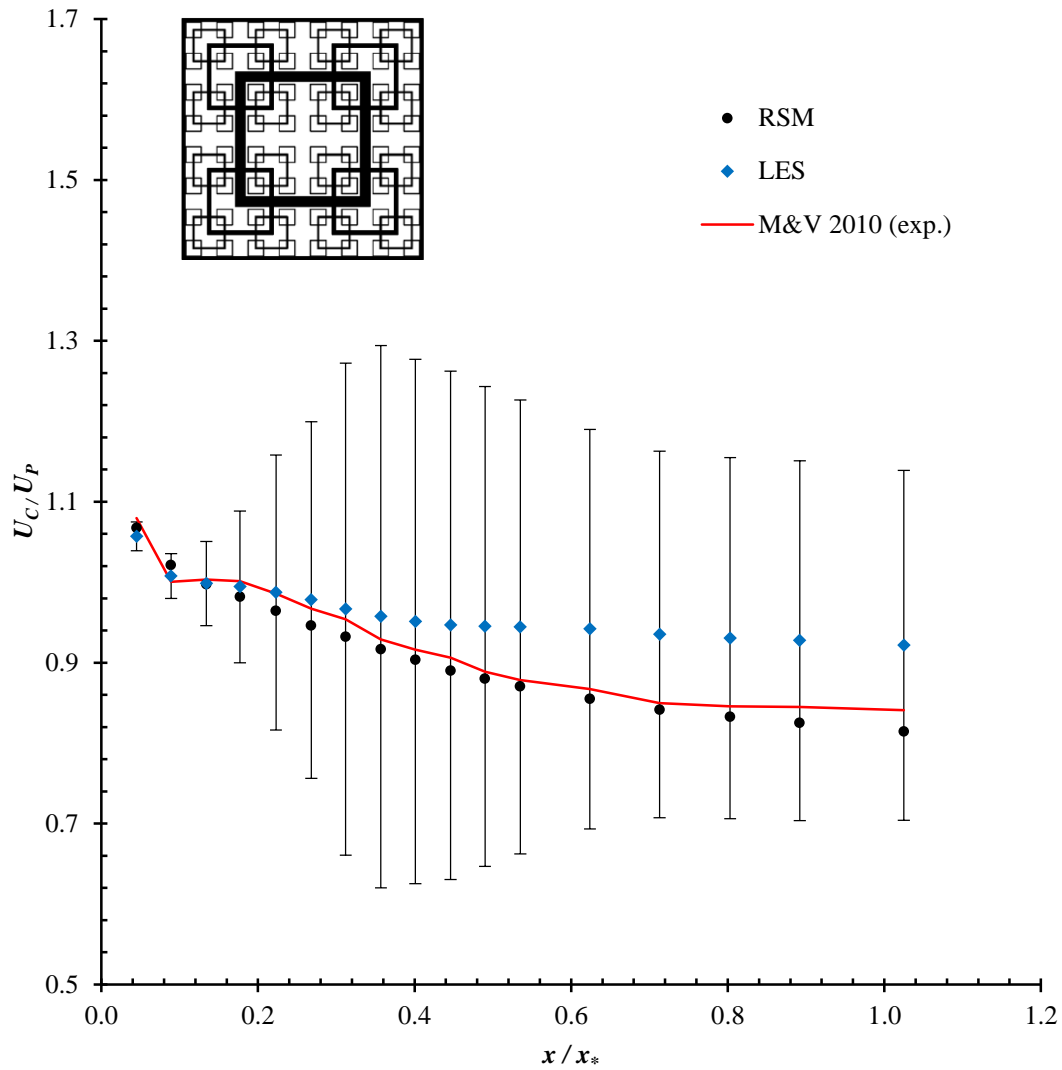
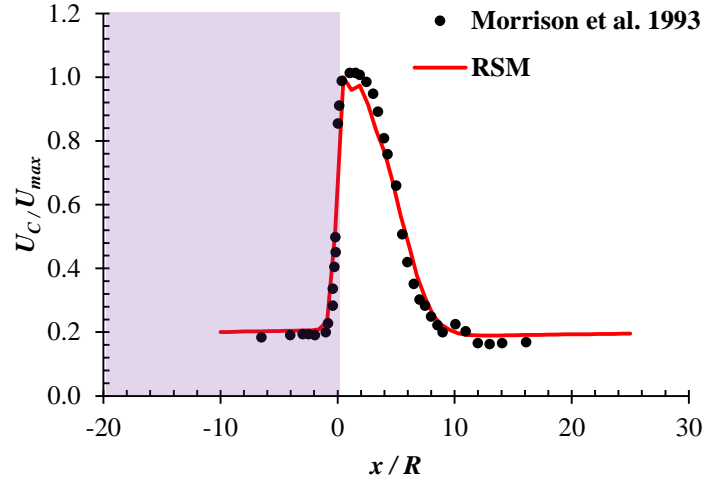
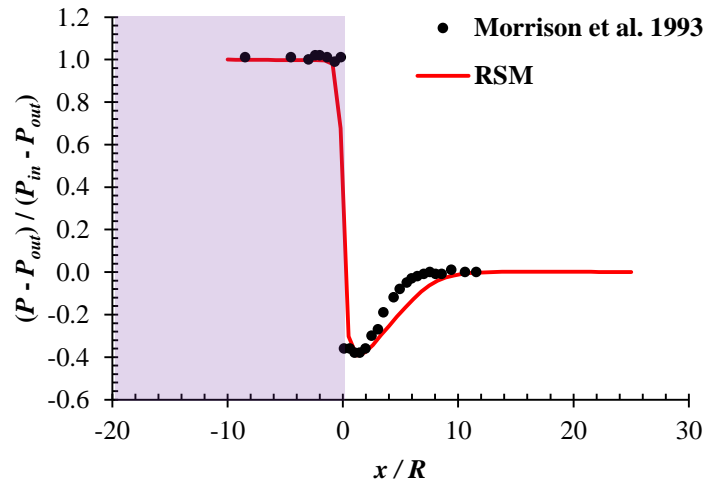


Figure 26. Variation of normalised centreline velocity U_C / U_P of $N = 4$ SFG17 with thickness $\delta = 5\text{mm}$ in the lee of the insert: numerical validation



(a)



(b)

Figure 27. Comparisons of the present numerical model with earlier reported experimental data for orifice insert: (a) U_C / U_{max} and (b) $(P - P_{out}) / (P_{in} - P_{out})$

Effects of different inserts and thickness on normalised centreline velocity

It is well known that different type of inserts is able to generate different characteristics of turbulence downstream of the channel, and in fact, these would affect the thermal mixing ability of a particular system [Suzuki, Nagata, Sakai, and Hayase \(2010\)](#). *Figure 28* shows the centreline velocity normalised by the inlet velocity U_C / U_∞ in the lee of the insert along x / H for all the inserts and EC (empty channel) in the present study. The result suggests that the variation of insert thickness do not have significant impact in the normalised centreline inlet velocity of RG, and their normalised centreline velocity immediately follows the profile of an EC. It could be explained by the method of symmetrically aligned and equal thickness of the bar on RG produces small scale homogeneous turbulence immediately after the RG insert. These perturbations cannot sustain for a longer period of time and decay immediately at a short distance $x / H = 0.625$ downstream. Hence, the different thicknesses of the RG insert do not have any significant effect on the centreline velocity. On the other hand, normalised centreline velocity for SG and CO type are quite similar, in which they show a rapid velocity increment until a sharp peak immediately after the insert at $x / H < 1$, before slowing down to a plateau at $1.5 < x / H < 5$, and returning to the profile of an EC further downstream of the insert at $x / H > 5$. The reason for SG and CO to follow such a velocity profile could be due to the similarity in blockage area and porosity surrounding the centre of the insert, as shown in *Figure 22(b)* and (c). Clearly, SG has more bars surrounding the centre on the inserts, especially the bars L_0 and L_1 . These bar thicknesses contribute towards the increase in blockage area surrounding the centre, or in another word, less porous for air to flow through when compared to the centre section of the insert. Hence, a majority of flow would pass through the middle section, forming a nozzle-like jet leeward of the centre of the insert. Similarly to SG, CO has blockage area at the side and surrounds the centre of the insert. However, in the case of CO, the blockage area is not porous-liked, which may direct more mass to flow through the centre area and this might be the cause to the higher centreline velocity than SG.

Moreover, in the case for SG and CO, the different insert thicknesses $\delta = 5\text{mm}$ and 40mm do affect the centreline velocity in the lee of the insert to some degree. It is interesting that the

calculated result suggests the centreline velocity for SG exhibits earlier reduction for $\delta = 5\text{mm}$ than for $\delta = 40\text{mm}$, and centreline velocity for $\delta = 5\text{mm}$ is slightly less than $\delta = 40\text{mm}$. It seems that the less porous outer area surrounding the centre area coupled with the higher air resistance of the non-shearing wall effect of the thicker insert, may have contributed towards the more energetic centreline velocity, as air would tend to flow through the path of less resistance. On the other hand, numerical results point out that the centreline velocity for CO follows the same profile as SG, except the results show the opposite thickness effect of SG, i.e. centreline velocity for $\delta = 5\text{mm}$ is higher than $\delta = 40\text{mm}$ at about $1.5 < x/H < 5$ downstream of the channel.

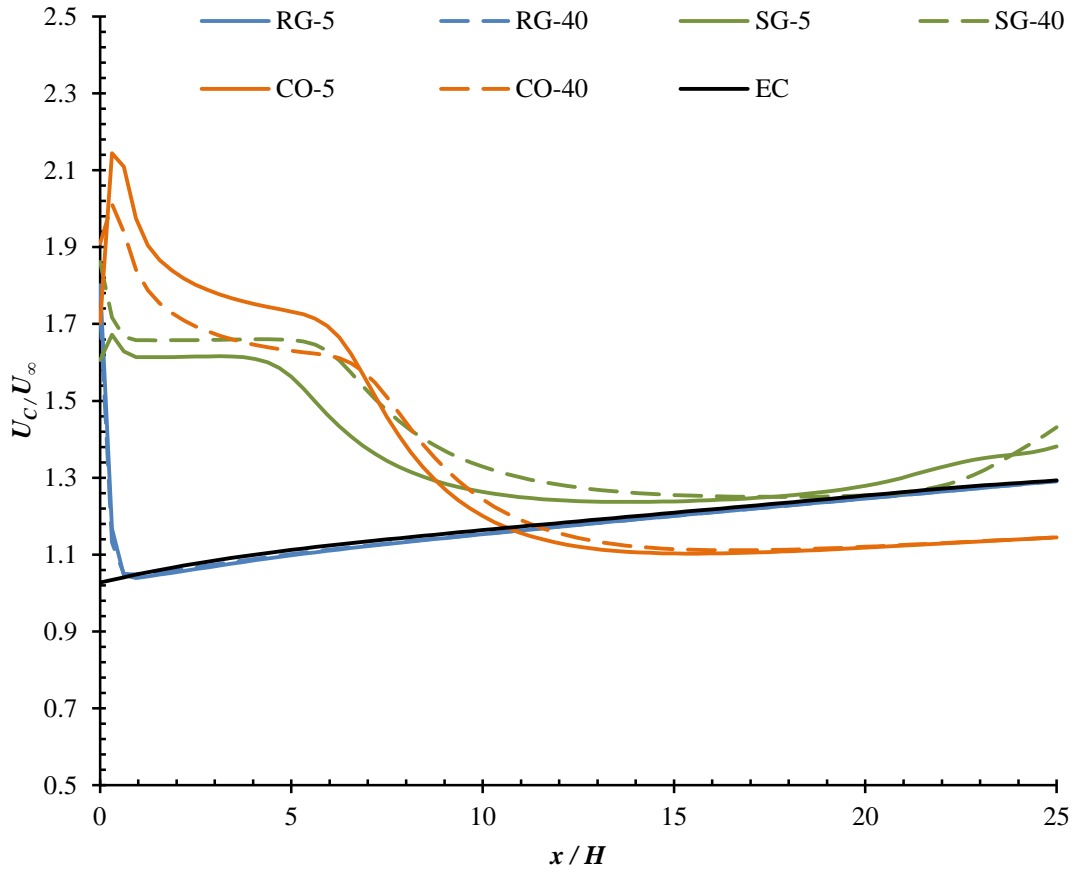


Figure 28. RSM calculated steady-state normalised centreline velocities U_C / U_∞ between RG-5, RG-40, $N = 3$ SG-5, $N = 3$ SG-40, CO-5, CO-40, and EC leeward of the insert

Thermal mixing performance of the various plates

The characteristics of a good thermal mixing are defined by the uniformity of the cross-sectional velocity and temperature leeward of the insert (Chiou, 1978; Mishra, Das, & Sarangi, 2008). Maximum cross-sectional temperature difference $\Delta\theta$ (see Eqn. 8) is used to show the evolution of temperature distribution within the cross-sectional area downstream from the insert. It is defined as the difference between the highest and lowest temperature across a single y - z plane $T_{A,max} - T_{A,min}$ and normalised with the temperature difference of the two inlet temperatures $T_H - T_C$. Low $\Delta\theta$ indicates a favourable mixing outcome as the temperature difference in an area is small. Figure 29(a) shows the comparison of $\Delta\theta$ between the different inserts used in the present study. The results point out that CO possesses the favourable lowest temperature difference across the cross-sectional area at the furthest recorded position downstream at $x / H = 21.875$, which is followed by SG, then RG. It is obvious that EC possesses the highest temperature difference across a cross-sectional area because of the absence of an insert to perturb the incoming fluid flow and to stimulate the formation of turbulence, which in turns promotes the interaction of the different streamlines required in the mixing action. RG, SG, and CO show about 28%, 88%, and 98% lower in temperature difference compared to EC at the furthest position acquired downstream, respectively.

At the distance $x / H < 6.875$ leeward of the insert, the trend follows as what was described previously for the downstream $\Delta\theta$, i.e. $\Delta\theta$, closer to the insert is lower for CO, follows by SG, then RG, and lastly the EC. The premixing for SG is not as significant as what CO could achieve, as the SG insert is porous, hence allowing a certain portion of the air to flow through. In the case for RG, the bars are symmetrically aligned and the area facing the incoming flow is homogeneous, thus the incoming air prior to the insert is not redirected towards the middle.

Figure 29(b) portrays θ for all inserts and EC, in which all cases show very similar cross-sectional averaged temperature along the downstream of the channel. Θ (see Eqn. 9) takes the cross-sectional averaged temperature into account using $T_H - T_{A,ave}$. It is clear that an outstanding hydrodynamic and thermal mixing is not only be characterised by the smaller cross-

sectional temperature difference, but also the larger reduction in warm air inlet temperature in the cross-sectional averaged temperature. Numerical results for Θ [see *Figure 29(c)*] indicate that CO possesses the best thermal mixing performance downstream of the insert when compared to EC, which the average of both thicknesses at about 5046% higher, followed by SG averagely at about 761% higher, then RG averagely at 40% higher at $x / H = 21.88$. More importantly, the results also reflect the fact that the thermal mixing of insert at $\delta = 5\text{mm}$ is about 47% better than at $\delta = 40\text{mm}$ for CO.

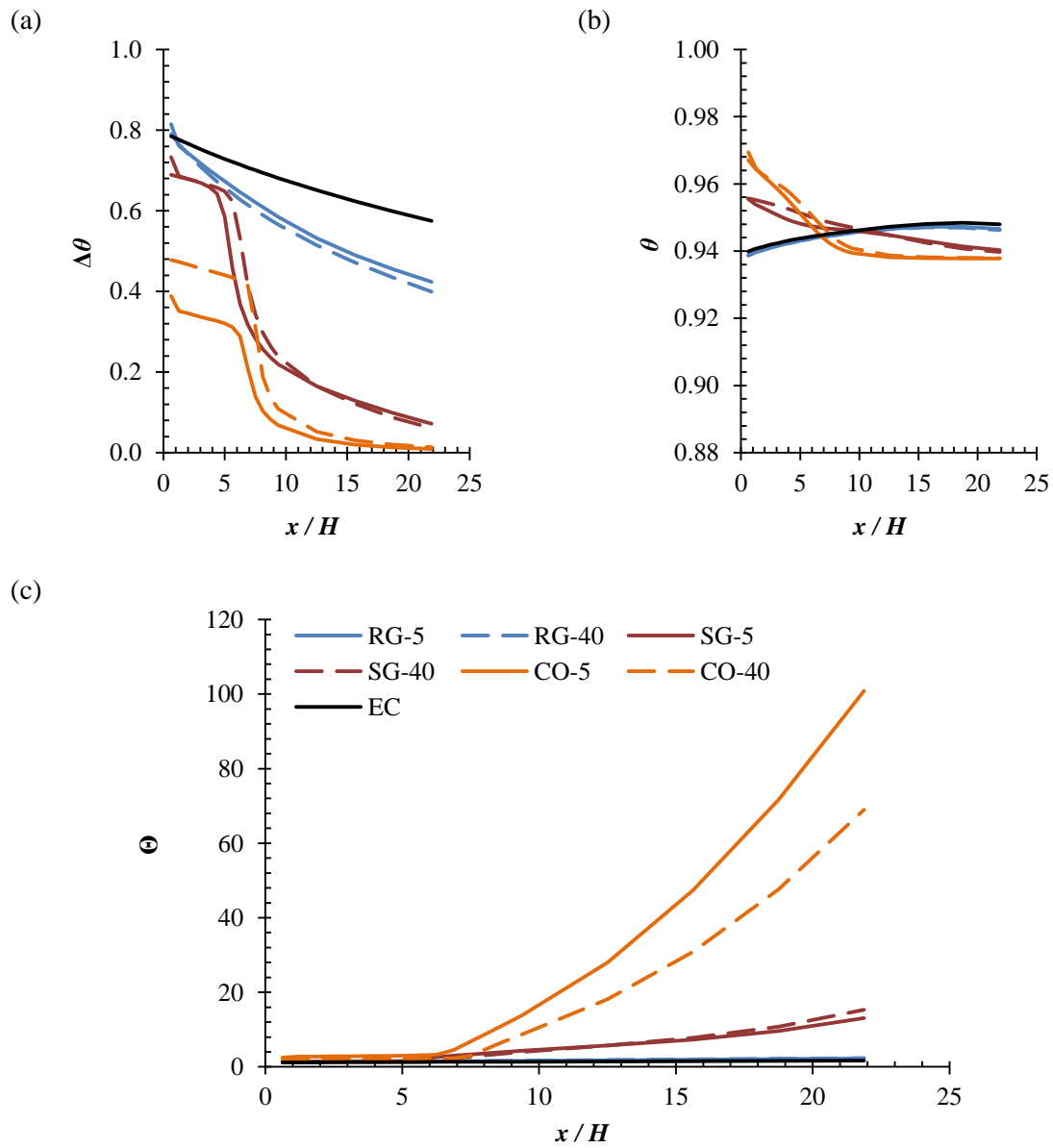


Figure 29. Comparisons of thermal mixing performance level among different inserts

Influence of turbulence kinetic energy on thermal mixing performance

To understand the effects and relationships between thermal mixing performance and turbulence kinetic energy, cross-sectional averaged turbulence kinetic energy at various locations leeward of the inserts are recorded and compared. *Figure 30* shows the cross-sectional averaged turbulence kinetic energy for all inserts normalised to EC (*Eqn. 10*). The turbulence kinetic energy for CO is higher in the region at $x/H < 15$, SG comes second in tow, and RG have the weakest turbulence kinetic energy among the inserts. It seems that the indicators to achieve higher thermal mixing performance are, (i) more energetic turbulence kinetic energy, and (ii) the ability to sustain high turbulence kinetic energy further downstream, such as those shown by CO and SG.

To better understand the influence of turbulence kinetic energy, histograms for cross-sectional turbulence kinetic energy of the two outperform inserts (SG and CO) are acquired and can be found in *Figure 31*. Comparisons are made using $\delta = 5\text{mm}$. At $x/H = 0$ (at the immediate leeward of the insert), SG seems able to produce more energetic turbulence kinetic energy over a wider band (maximum value at 0.381 J/kg) when compared to CO (highest value 0.153 J/kg). Due to the presence of criss-crossing mesh on SG insert, which in turn, create a lot of wake turbulence leeward of the insert, which is more clearly shown in *Figure 32(c)*. Conversely, CO insert does not have any blockage area around the centre to produce wake turbulence. Hence, CO appears to show lack of wake generation immediately in the lee from the insert. However, at a small distance downstream of the insert at $x/H = 3.13$, the circumstances change for both SG and CO. The cross-sectional area turbulence kinetic energy generated by the CO insert becomes more energetic than SG, by which the upper band extends to 0.436 J/kg for CO insert when compared to 0.124 J/kg for SG. This cross-sectional area turbulence kinetic trend remains similar at the distance $x/H = 6.25, 9.38$, and 21.88 downstream of the channel, where the cross-sectional area-averaged turbulence kinetic energy for both inserts are dissipated to nearly the same level, i.e. the turbulence kinetic energy spans from 0.024 to 0.068 J/kg. At $x/H = 21.88$, SG shows slightly higher level of turbulence kinetic energy than CO, which [Mazellier and Vassilicos \(2010\)](#) described the phenomena as wake interaction between the bars of different thicknesses in a fractal. Hence, the current numerical results is able to determine the influence of each insert

induced turbulence kinetic energy on the hydrodynamic and thermal mixing performances, i.e. the higher in value and wider in histogram range of the generated turbulence kinetic energy, the stronger the insert thermal mixing capability in sustaining or propagating turbulence further downstream of the mixing chamber.

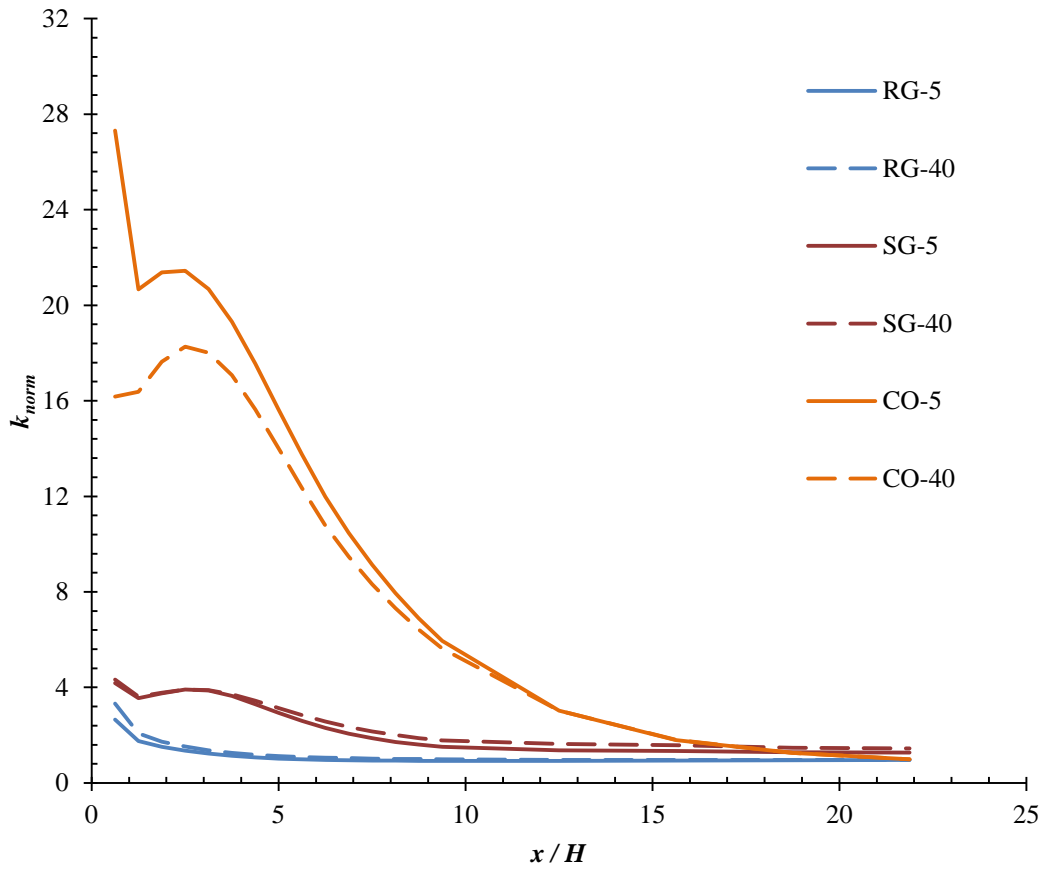


Figure 30. Comparisons of area-averaged turbulence kinetic energy between the various inserts using steady-state RSM model

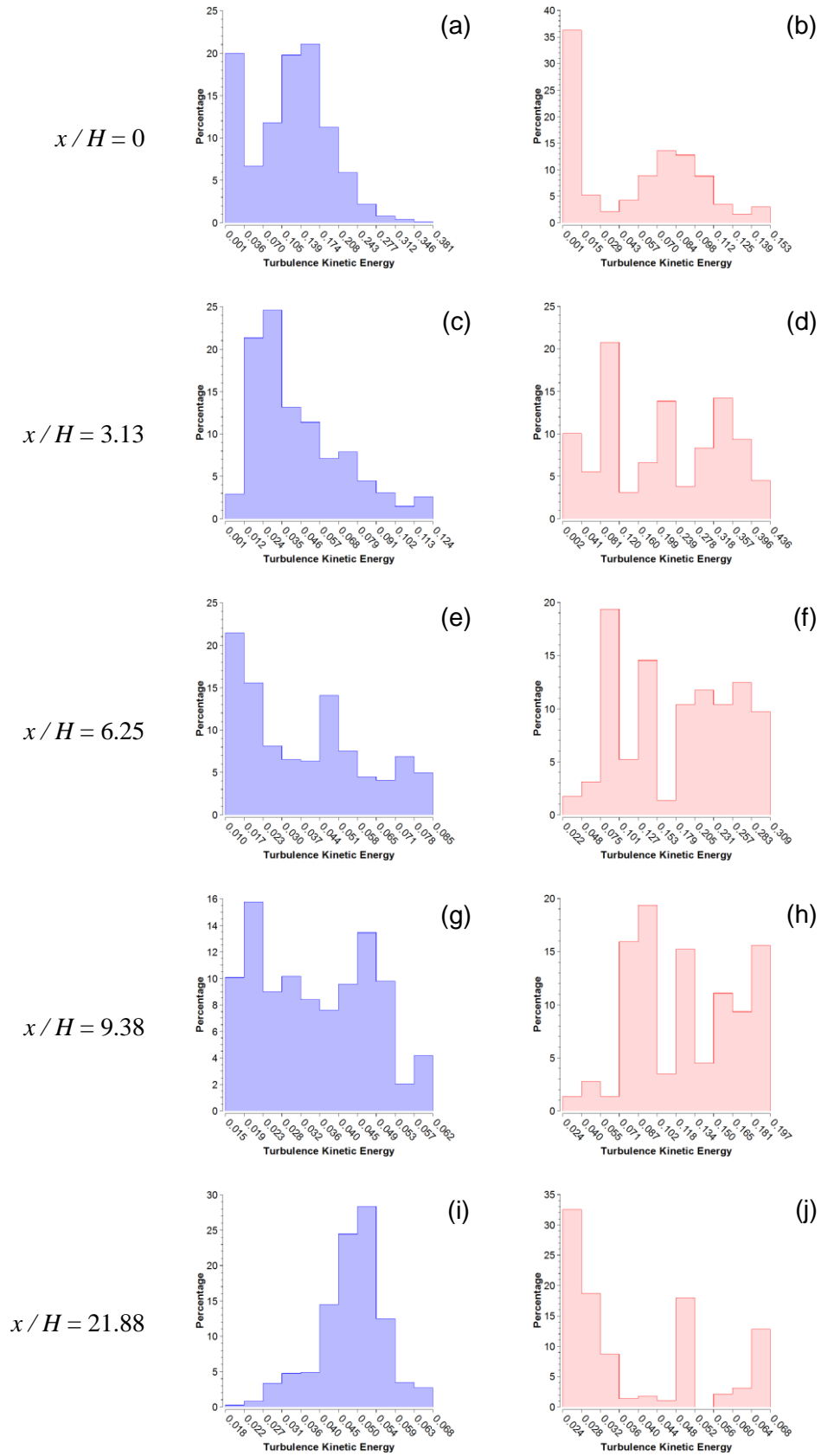


Figure 31. Planar turbulence kinetic energy histogram for SG-5 (a, c, e, g, i) and CO-5 (b, d, f, h,

j)

Stream-wise cross-section temperature, turbulence kinetic energy contour, and velocity streamline plot

To better explain the probable contribution of CO towards higher turbulence kinetic energy, which in turn enables better thermal mixing performance, diagonal cross-sectional contour plot for turbulence kinetic energy and temperature, as well as velocity streamline are plotted and presented as *Figure 32* (diagonal line 1 – 1' for cross-section). *Figure 32*(a), (b), (c), and (d) represents EC, RG, SG, and CO, respectively, and the thickness for all inserts $\delta = 5\text{mm}$.

Both EC and RG have almost identical temperature contour due to the inability of RG insert to induce thermal mixing [refer to *Figure 32*(a) & (b)]. The evenly aligned bars of the same thickness in RG do not encourage much interaction among the different streamline. Hence, it behaves more similarly to a turbulence inducing flow straightener, rather than a mixer. On the other hand, as previously discussed, both of the numerical results suggested that SG and CO possesses the ability to induce thermal mixing by generating stronger turbulence kinetic energy and further sustaining it. Temperature contour plot for SG [*Figure 32*(c) [top]] shows thorough mixing towards the end of the channel at $x/H = 21.88$. [Mazellier and Vassilicos \(2010\)](#) described the wake interactions between the thickest and subsequent thinner bars in their investigations, and these wake interactions do complement in sustaining the turbulence kinetic energy further downstream in the present study [see *Figure 32*(c) [middle]]. As previously discussed, the area around the centre of the insert is surrounded by bars and forms a finite porosity, which is able to redirects some of the incoming flow towards the more porous centre area, forming a higher velocity region. *Figure 32*(c) [bottom] shows the velocity streamline plot for SG, and it portrays more clearly that the centre portion leeward of the insert has higher velocity when compared to the sides. CO also displays good thermal mixing performance, which is shown in *Figure 32*(d) [top] temperature contour plot. It also depicts evenly distributed temperature approaching the end of the test section at $x/H = 21.88$. Interestingly, high turbulence kinetic energy regions exist starting from the lee of CO, and joining up a distance downstream at about $x/H = 7.81$ (see *Figure 32*(d) [middle]). Seemingly, the high turbulence kinetic energy region is produced by the

large recirculating eddies in the lee of CO, which can be clearly observed in velocity streamline plot {see *Figure 32(d)* [bottom]}.

The diagonal temperature and velocity distributions downstream at $x / H = 21.88$ are closely scrutinised for both SG and CO and portrayed as *Figure 33*. It is clear that the temperature profile for CO is more evenly distributed, i.e. temperature difference between maximum and minimum value is small, at $x / H = 21.88$, when compared to SG. CO also produces more uniform velocity profile, i.e. flatter profile in the middle section, in comparison with SG. One probable explanation to SG insert performs poorly when compared to CO insert is the thickness of the wake generation bars found on SG, of which the bar thickness spans from 10mm, 5mm, and 2.5mm for the thinnest bars, and the porosity embedded with the design of SG. Meanwhile, CO has larger blockage areas located closer to the corners of the inserts, which produce the larger wake. The energetic recirculating streamlines forms large eddies which are instrumental to the promotion of mixing between different streamlines. The thermal mixing is noticeable when comparing the cross-sectional temperature contour plot between SG and CO {see *Figure 32(c)* [top] and *Figure 32(d)* [top]}, of which CO could achieve thorough thermal mixing at a shorter distance as compared to SG.

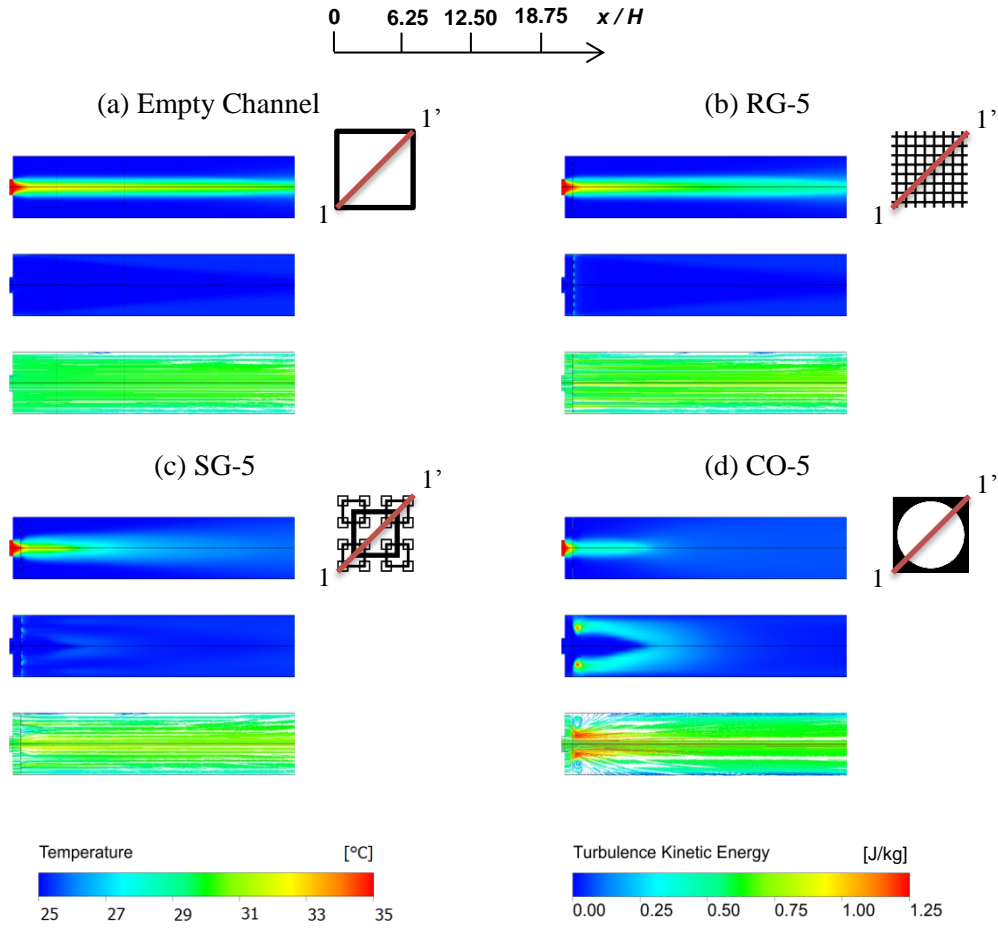


Figure 32. RSM calculated steady-state 45° diagonal section 1-1' temperature distribution (top), turbulent kinetic energy (middle), and velocity streamline (bottom) contour plot for (a) empty channel, (b) RG-5, (c) SG-5, and (d) CO-5, respectively – Scaling in $y/H : x/H = 1 : 2.5$

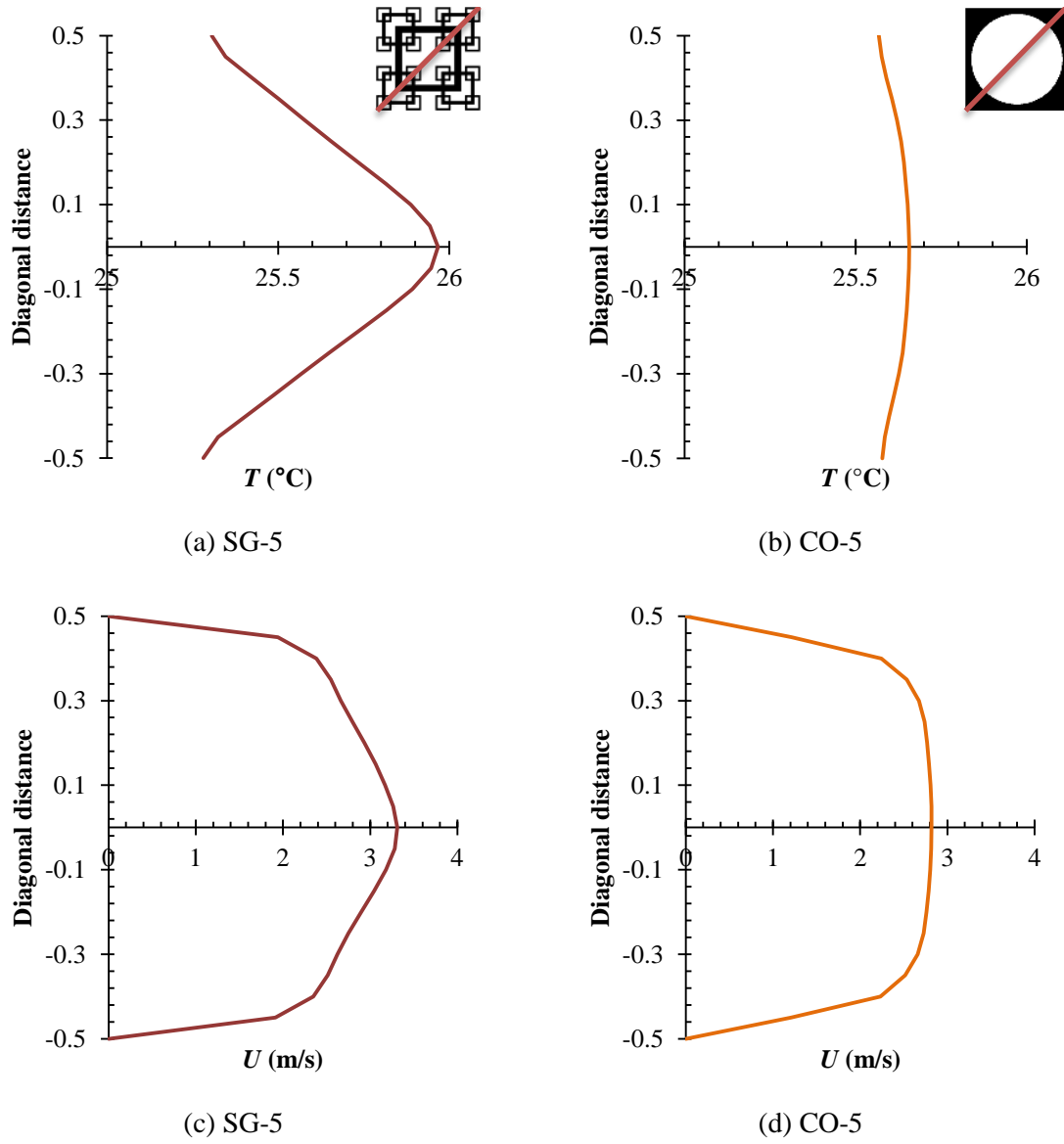


Figure 33. 45° diagonal temperature distributions and velocity profiles in the lee of the insert of (a) SG-5 and (b) CO-5 at downstream distance $x/H = 21.88$

LES simulated velocity fluctuation using CO-5 insert

Transient LES is conducted as an extension to the previous steady-state RSM investigation. LES instantaneous velocity data are taken diagonally from the insert at y/H and $z/H = 0, 0.125$, and 0.313 , respectively. The fluid flow fluctuation along the diagonal locations can be best described at (i) the centre of the insert, (ii) the boundary between the two inlets, and (iii) the insert blockage boundary in the lee of the CO, respectively. Seven locations downstream are taken, i.e. $x/H = 0, 3.13, 6.25, 9.38, 12.50, 15.63$ and 21.88 . Data were collected over a total time duration of $\Delta t = 1$ second with 2×10^5 number of time steps. The numerically calculated results are presented in *Figure 34*. The mean velocity for transient LES is represented in solid diamond symbols and the error bars express the standard deviation of the hydrodynamic fluctuation. The results show that transient LES could still predict the mean velocity, to certain degree of accuracy, when compared to the predicted velocity using steady-state RSM (red line). As previously discussed, the mean velocity predictions for LES could differ from the steady-state prediction of RSM or experimental results if the statistical data are lacking and statistical convergence could not be reached when taking the mean value. Computational resources are not sufficiently available to carry out longer prediction in time as it is not periodically feasible for this study. Nevertheless, the velocity matches well when the fluctuation is homogeneous enough to gain statistical convergence within such a short data capture timeframe. Eventually, the hydrodynamic fluctuations are clearly seen to dissipate at a long distance downstream of the channel.

Transient LES results clearly indicate the presence of large hydrodynamic fluctuations immediately in the lee of the CO and these fluctuations is much more energetic than those closer to the centre of the insert. It strongly supports the findings of the steady-state RSM prediction, of which the turbulence kinetic energy is stronger near the blockage boundary of CO due to the presence of the larger fluctuation in velocity. To gain a clearer picture on the velocity fluctuations, component velocities u_x , u_y , and u_z are normalised against instantaneous velocity U (not averaged total velocity) as presented in *Figure 35*. Instantaneous velocity U can be described as the velocity at a certain time step. This normalising method brings out the ratio of componential instantaneous velocity to the total velocity at the same time step. It seems that the

numerical results [see *Figure 35(g-i)*] suggest the flow fluctuates vigorously at $x/H = 3.13$ in the lee of the CO insert at y/H and $z/H = 0.313$ (red line), than other locations downstream of the channel, as well as at locations nearer the centre of the CO insert. It tallies well with the correlation of high turbulence kinetic energy with high fluctuation velocities in all x , y , and z direction.

Standard deviation for u_x / U , u_y / U , and u_z / U is used to compare the fluctuations at all data collecting locations, of which the results are tabulated from *Table 8* to *Table 10*. The highest fluctuations occurs at location $(x/H, y/H, z/H) = (3.13, 0.313, 0.313)$ with standard deviation = ~ 0.271 away from the mean for u_x / U , ~ 0.141 for u_y / U and ~ 0.126 for u_z / U . Meanwhile, other locations downstream of the channel have lower standard deviation (or fluctuations) from the mean.

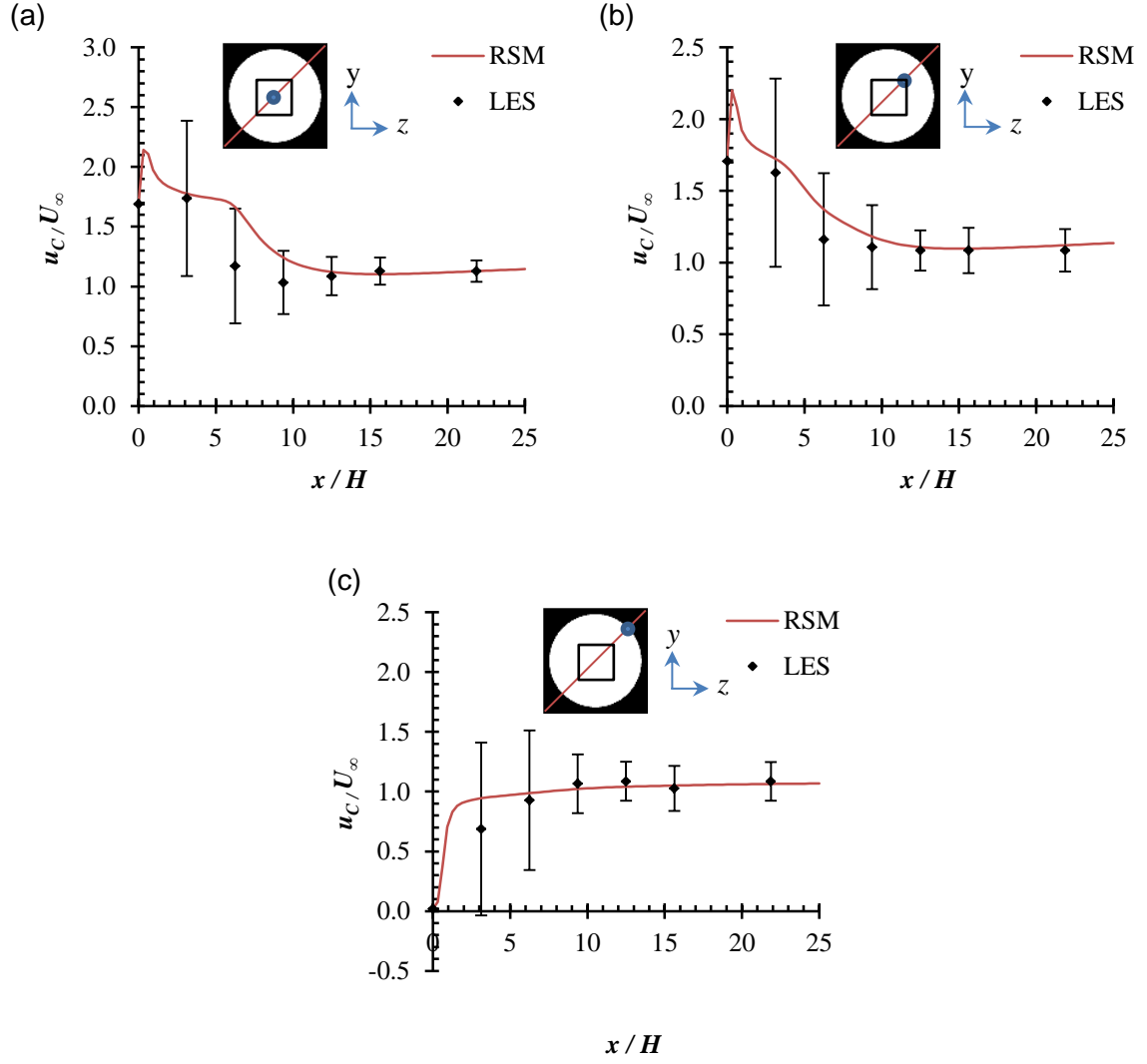


Figure 34. U_c / U_{in} velocity fluctuations between steady-state RSM and transient LES simulation ($\Delta t = 1$ s) for CO-5 along the diagonal distance of $y/H = z/H$ i.e., at (a) $z/H = 0$, (b) $z/H = 0.125$, and (c) $z/H = 0.313$

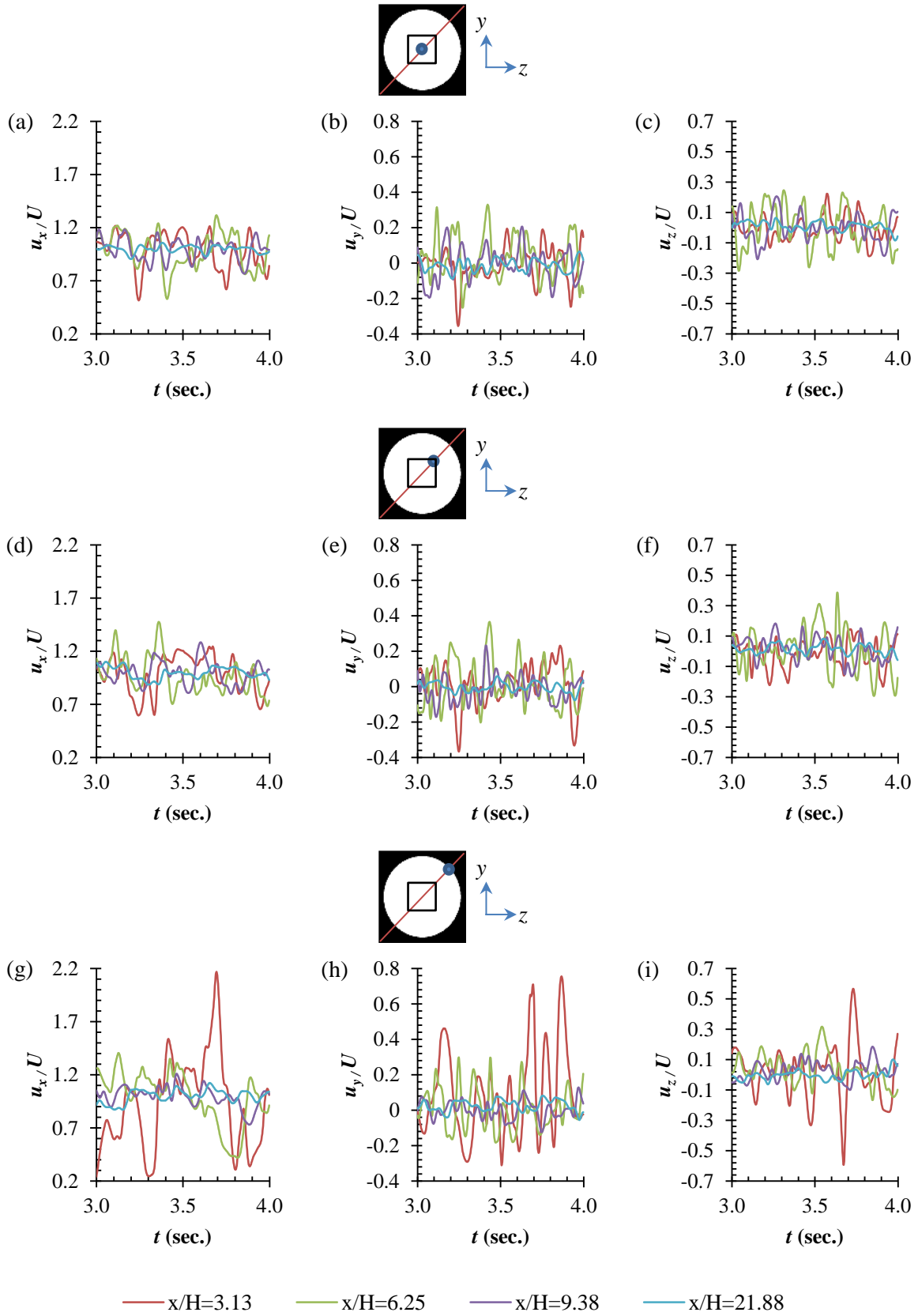


Figure 35. Velocity components u_x / U , u_y / U , and u_z / U in the lee of CO-5 at $x / H = 3.13, 6.25, 9.38$, and 21.88 , along the diagonal distance i.e. y / H & $z / H = 0$ (top, a-c), 0.125 (middle, d-f), and 0.313 (bottom, g-i)

Table 8. Standard deviation for u_x / U , u_y / U , and u_z / U at y / H & $z / H = 0$

Standard deviation	$x / H = 3.13$	$x / H = 6.25$	$x / H = 9.38$	$x / H = 21.88$
u_x / U	0.162	0.117	0.099	0.031
u_y / U	0.081	0.075	0.042	0.018
u_z / U	0.075	0.072	0.041	0.016

Table 9. Standard deviation for u_x / U , u_y / U , and u_z / U at y / H & $z / H = 0.125$

Standard deviation	$x / H = 3.13$	$x / H = 6.25$	$x / H = 9.38$	$x / H = 21.88$
u_x / U	0.166	0.121	0.079	0.044
u_y / U	0.074	0.058	0.044	0.018
u_z / U	0.077	0.074	0.044	0.014

Table 10. Standard deviation for u_x / U , u_y / U , and u_z / U at y / H & $z / H = 0.313$

Standard deviation	$x / H = 3.13$	$x / H = 6.25$	$x / H = 9.38$	$x / H = 21.88$
u_x / U	0.271	0.133	0.092	0.044
u_y / U	0.141	0.050	0.038	0.018
u_z / U	0.126	0.058	0.033	0.012

Pressure drop and system performance of the various inserts

It would be meaningful to gauge the thermal mixing performance together with the pressure drop induced by the inserts, as it would not make sense in both economically and environmental-friendliness, to promote turbulence generating insert with significantly high pressure drop which requires a lot more pumping power. *Figure 36* shows the planar-averaged pressure drop induced by the various inserts used in the present study. Numerical results point out that CO inserts perform the best among the inserts in terms of thermal mixing performance, followed by SG, then RG, and the differences between the various inserts are small (about 0.5Pa on average). Numerical results suggests the pressure drop for CO of thickness $\delta = 5\text{mm}$ is larger than $\delta = 40\text{mm}$, which was also observed in [Fossa and Guglielmini \(2002\)](#). However, pressure drop evaluation shows the opposite trend of thermal mixing performance, whereby RG possesses the lowest pressure drop, followed by SG, then CO. Although RG are more favourable in this evaluation, nevertheless the merit gained by lower pressure drop could not offset its shortcoming in the thermal mixing performance (see *Figure 37*).

Figure 37 shows the system performance η of the various inserts, of which η is defined previously in *Eqn. 12*. It shows CO has the highest system performance among the inserts, leading SG inserts by about 5.6 \times , and almost 33.6 \times higher than RG.

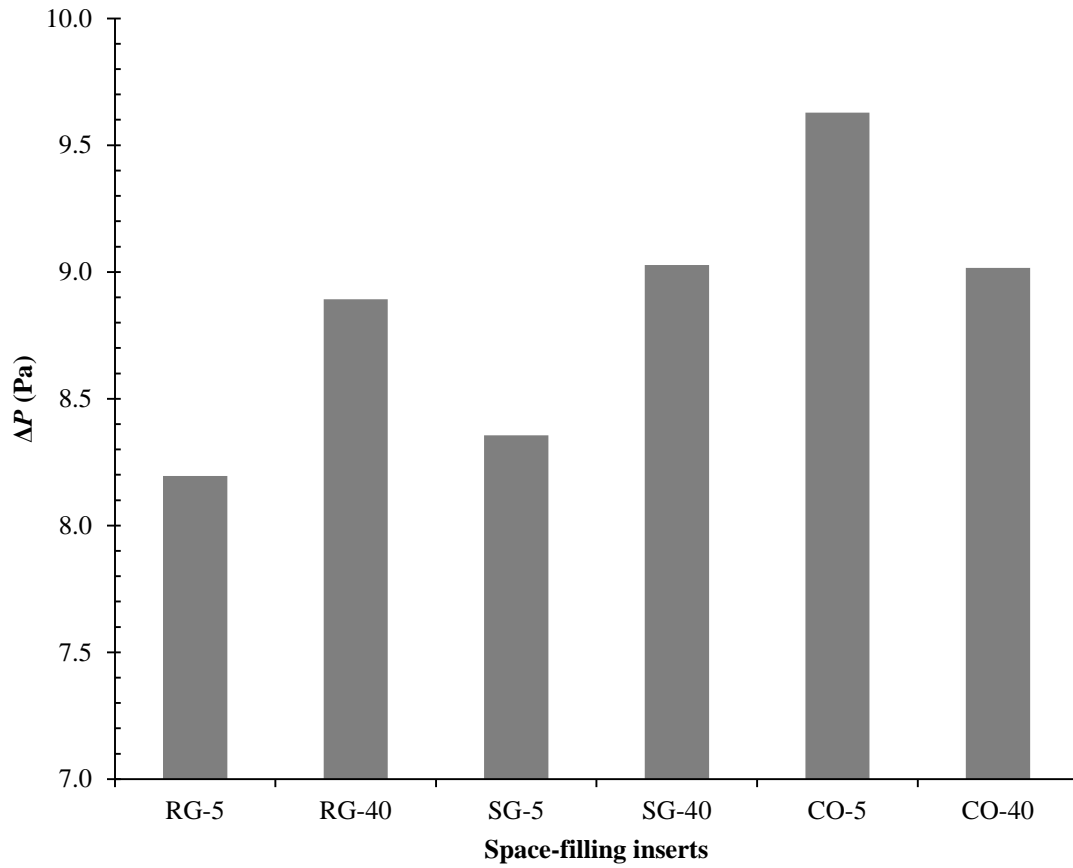


Figure 36. Numerically examined pressure drop of each insert with RSM modeling

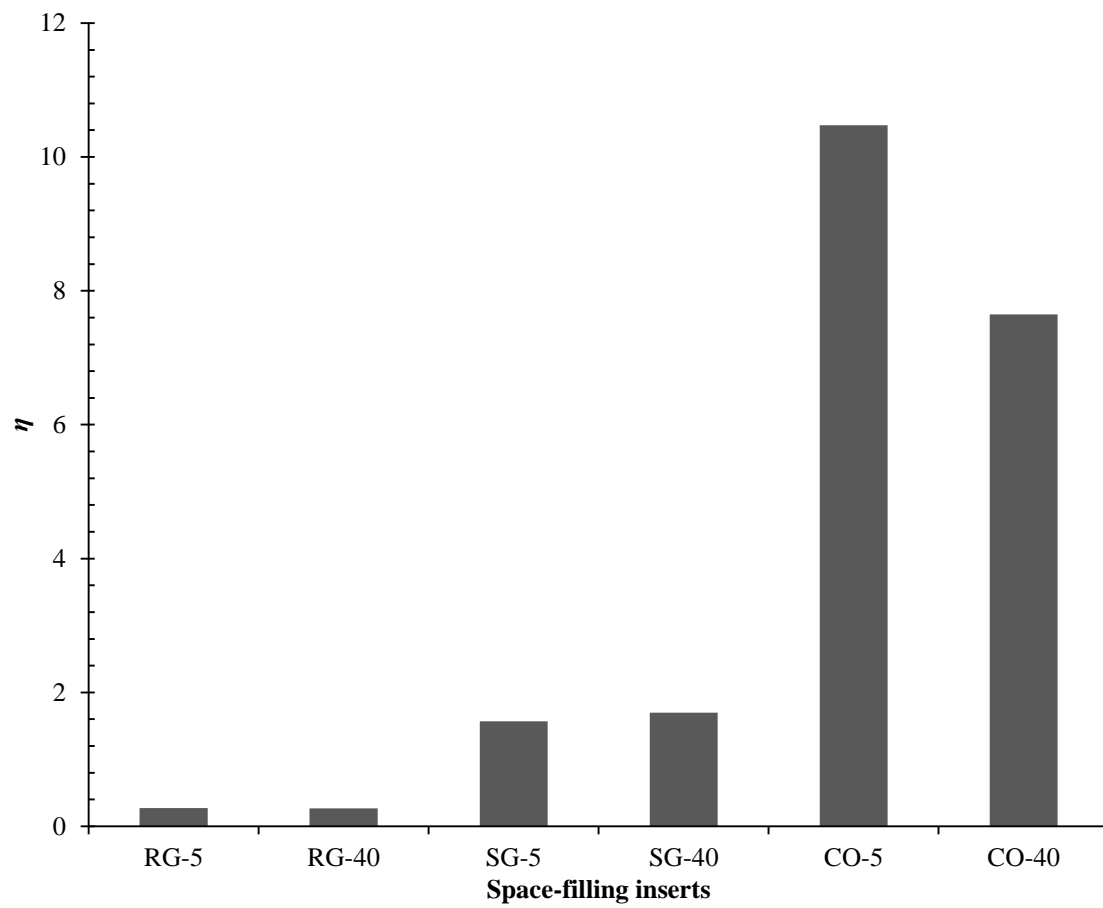


Figure 37. Overall system performance level for the present study

Chapter summary

This study is carried out to evaluate and to select the highest system performance among RG, SG, and CO turbulence generating inserts. Most importantly, a 3D steady-state and incompressible thermal mixing performances induced by various inserts of different configurations have been investigated. The chapter can be summarised as follows:

1. Numerical validations of the current employed turbulence models are in good agreement with experimental data reported by other researchers.
2. CO is able to generate higher η among other inserts, which effectively balance between the thermal mixing at a relatively lower pressure drop. The presence of larger blockage in CO allows the formation of larger wakes in the lee of the insert. In the meantime with the flow recirculation falling into the regime of higher turbulence kinetic energy, such unique characteristics are able to predominantly promote hydrodynamic and thermal mixing. As a result, large flow recirculation is desirable to achieve better thermal mixing performance.
3. The study opened up the new alternative and possibility into using insert of various geometries to generate the effective hydrodynamic fluctuations to further enhance the thermal mixing performance. The identified configurations may then be applied onto the free-cooling section of a heating, ventilation and air-conditioning (HVAC) system in terms of long-term waste energy sustainability, as well as waste energy management.

PART B: Suggested Declaration for Thesis Chapter 5

[This declaration to be completed for each conjointly authored publication and to be placed at the start of the thesis chapter in which the publication appears.]

Monash University

Declaration for Thesis Chapter 5

Declaration by candidate

In the case of Chapter 5, the nature and extent of my contribution to the work was the following:

Nature of contribution	Extent of contribution (%)
Main author, contributes constructive comments, insights, and analysis towards results and discussion of this paper.	50%

The following co-authors contributed to the work. If co-authors are students at Monash University, the extent of their contribution in percentage terms must be stated:

Name	Nature of contribution	Extent of contribution (%) for student co-authors only
Siow Yong Hoi	Undergraduate, numerical works, introduction and methodology section.	50%

The undersigned hereby certify that the above declaration correctly reflects the nature and extent of the candidate's and co-authors' contributions to this work*.

**Candidate's
Signature**

	Date 14/09/2015
---	------------------------

**Main
Supervisor's
Signature**

	Date 14/09/2015
---	------------------------

*Note: Where the responsible author is not the candidate's main supervisor, the main supervisor should consult with the responsible author to agree on the respective contributions of the authors.

CHAPTER 5 – RESULTS AND DISCUSSION : PHASE 2

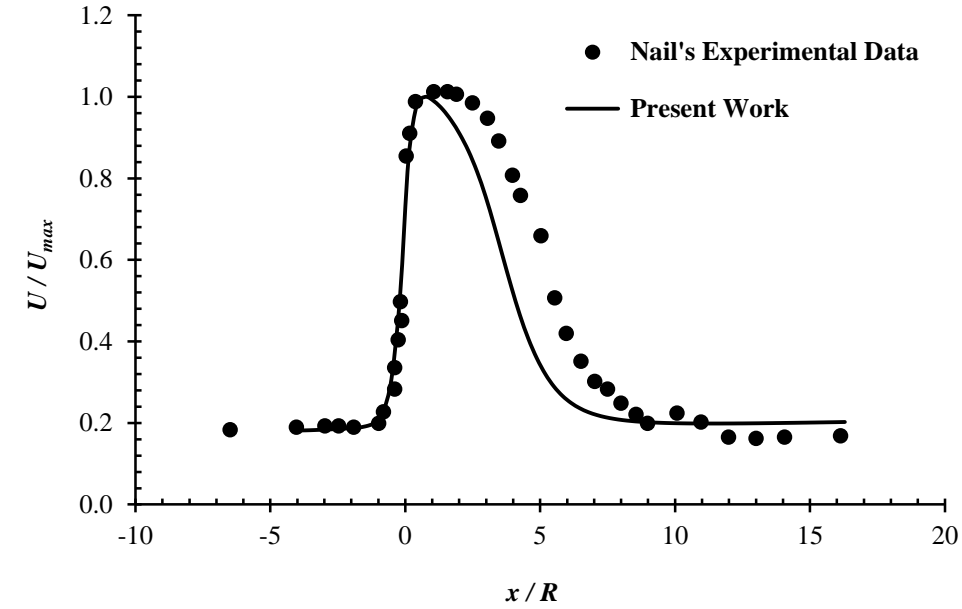
Thermal mixing enhancement after a *T*-duct with a 2D space filling insert

This chapter presents the results for phase two of the present studies. To better incorporate the findings into applications in the real world, the inserts are evaluated on the effectiveness of thermal mixing using different insert designs with asymmetrical temperature differential inlets. This kind of asymmetrical inlets can be found in free-cooling system (economisers) in HVAC applications. The studies in the present chapter also incorporate the effect of tilting of the inserts to generate larger wakes, which are important to the enhancement of thermal mixing performance mentioned in the previous chapter.

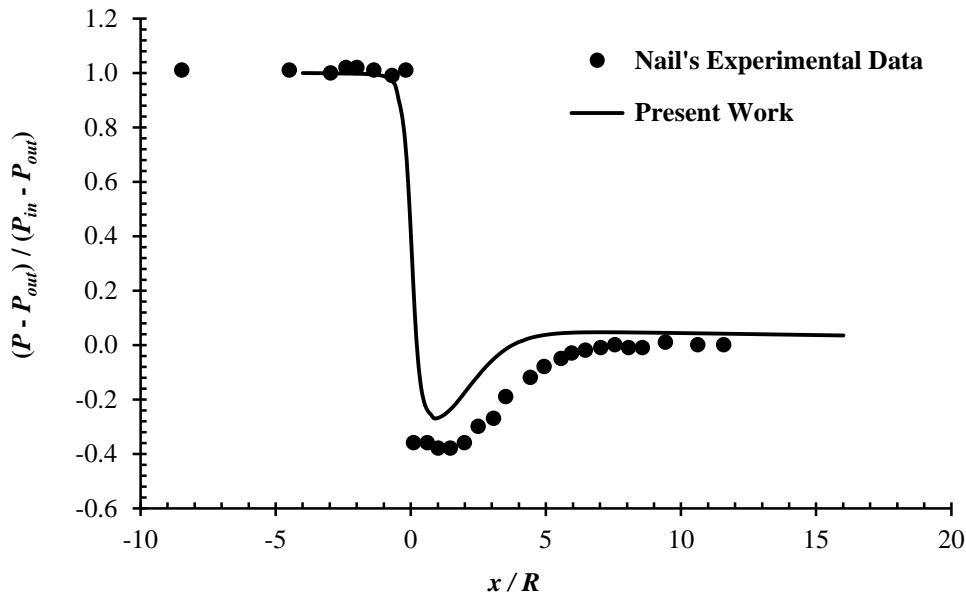
Validation of numerical simulations

The experimental results recorded by Nails [cited [Morrison et al. \(1993\)](#)] and [Mazellier and Vassilicos \(2010\)](#) are used to validate the current 3D, steady-state computational model. An orifice meter is emphasised on the flow field induced by the former, whereas the latter focused on using 2D $N = 4$ space filling fractal square grid to generate turbulent fluctuations. *Figure 38* shows the comparisons between experimental normalised centerline velocity and pressure distributions results by Nails with the present simulated results. Measurements are denoted by solid circular symbols and solid lines are the computed outcomes. Clearly, good agreement between the experimental observations and numerical predictions are noted in the numerical validations indicate good agreement. The existence of the minor deviation from the experimental data may be caused by the high blockage ratio ($\sigma = 0.75$) of a diffuser-like orifice meter induced jet diffusion downstream of the tube from $x / R = 3.0$ to 6.5, of which [Shaaban \(2014\)](#) noted the numerical model may have difficulty to accurately determine such high jet diffusion. The comparison between [Mazellier and Vassilicos \(2010\)](#) normalised centerline velocity distribution and the current predicted data immediately in the lee of the insert from $x / x_{Meff} = 0$ to further downstream, are shown in *Figure 39*. The experimentally recorded data are denoted by unfilled triangles and solid line stands for the calculated results. The purpose for introducing fractal

geometry is to interrupt the upstream flow. It is safe to claim that the current model could predict the velocity changes induced by the complicated 2D space-filling $N = 4$ fractal square grid with blockage ratio $\sigma = 0.25$.



(a)



(b)

Figure 38. Numerical validation between the present work and experimental results by Nail

(Shaaban, 2014) (a) Normalised centreline velocity, and (b) normalised static pressure

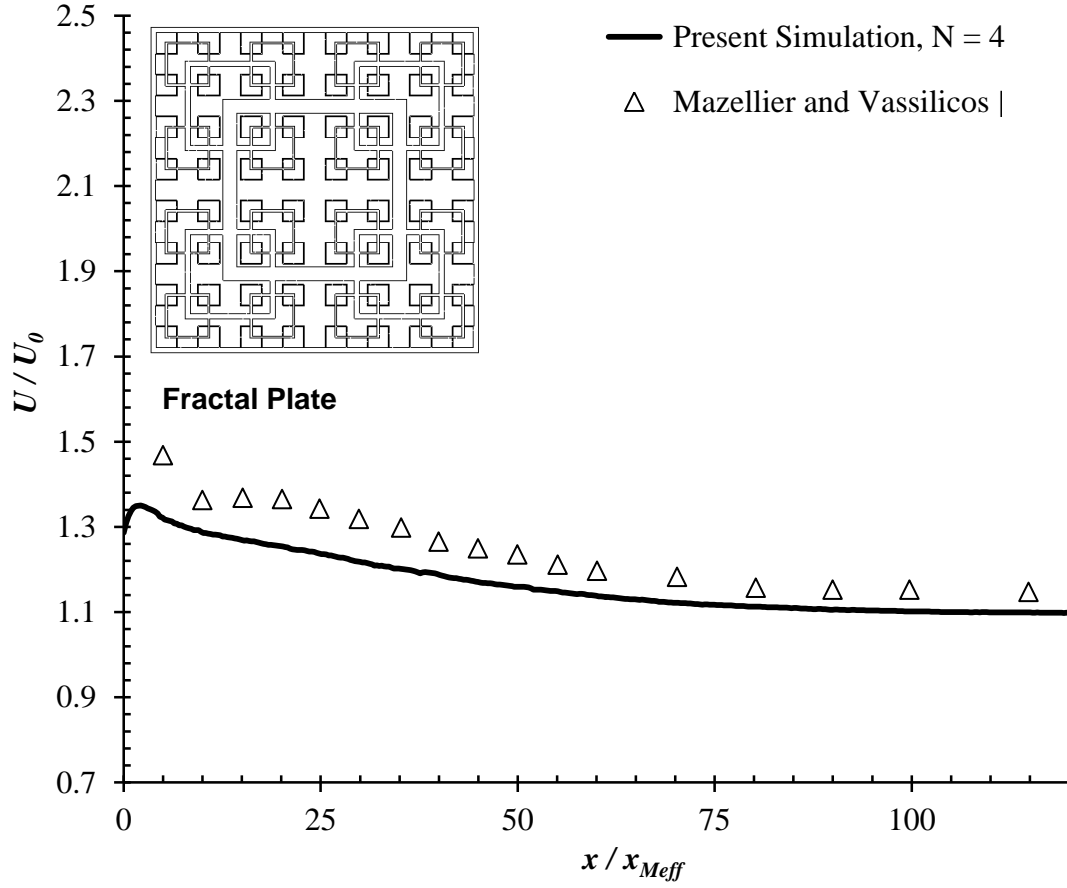


Figure 39. Numerical validation using normalised centreline velocity distributions of 2D space-filling positive square fractal grid $N = 4$ between turbulence model used in present work and experimental results (Mazellier & Vassilicos, 2010)

Effects of various inserts and tilted angle on thermal mixing performance

Calay and Wang (2013) found that in most developed countries, energy consumption for building usage could use up to 40% of the overall accessible energy. In order to address the depleting natural resources and to reduce greenhouse gas (GHG) emission, the introduction of macro-scale thermal mixing of HVAC incorporated economiser may be necessary to prevent the non-uniformity in temperature or flow to deteriorate the downstream heat exchanger thermal dissipative performance (Mishra et al., 2008). Figure 40 shows the normalised maximum and minimum temperature difference $\Delta\theta$ within each cross-section downstream of CO, PSFG, NSFG and the smooth channel without insert at different tilt angle β . Thermal mixing effectiveness for tilted space-filling inserts increases as the $\Delta\theta$ decreases downstream of the channel and the distributions are lower. Apparently, most of the space-filling inserts have improvements over the control empty channel (solid line) except for PSFG at $\beta = 0^\circ$ where $\Delta\theta$ is higher. The $\delta = 20\text{mm}$ PSFG may act as a flow regulator instead of a turbulence generator due to its higher $\Delta\theta$. It is also found that CO at $\beta = +45^\circ$ has the lowest change in $\Delta\theta$ downstream of the evaluated inserts, where it is 4.6, 17.2, and 21.7 times lower than NSFG at $\beta = +45^\circ$, PSFG at $\beta = +45^\circ$, and the smooth channel without insert, respectively, at $x / H = 4.2$ downstream of the insert. The dimensionless temperature difference attains the lowest i.e. $\Delta\theta = 0.009$ for CO tilted at $\beta = +45^\circ$, whereas it is only 0.250 and 0.047 for PSFG and NSFG at the same β , respectively, at the furthest downstream $x / H = 16.7$. It seems the flow recirculation induced by the hydrodynamic fluctuations leeward of CO may serve as one of the important factors in the promotion of thermal mixing.

The thermal mixing performance Θ characterises the ratio of the relative averaged cross-sectional temperature reduction with respect to the recycled warm air over the maximum temperature changes of the same cross-section. Thus, the smaller difference in temperature and the larger reduction of temperature would yield higher Θ . Figure 41 shows the thermal mixing performance of the present 2D planar space filling inserts with different tilted angles at $Re_H = 2.19 \times 10^4$. From Figure 41(a-c), Θ increases downstream of the mixing chamber for empty channel, CO, PSFG, and NSFG. Results show the thermal mixing performances for titled inserts are higher when compared to non-tilted plates and empty channel. Hence, tilted inserts are able to provide higher turbulent mixing. Without a doubt, thermal mixing is greater with tilted and non-tilted CO,

followed by NSFG, PSFG and the empty channel. For CO and NSFG insert with $\beta = +45^\circ$, the thermal mixing is more effective because of the empowered direct interaction at upstream of the channel of the drawn in cooler air and the blocked recycled warm air to proceed further downstream. However, for CO and NSFG inserts with $\beta = -45^\circ$, the performance are solely dependent on the effects of space filling configuration and 2D planar plate orientation in generating turbulent fluctuations downstream of each plate to achieve major thermal mixing. The σ of CO and NSFG at $\beta = \pm 45^\circ$ increase 13% compared with that at $\beta = 0^\circ$, and it is 64% larger for PSFG (see *Table 11*). It is important to note that the original space filling configurations remain even though the inserts have been tilted. Thus, the increased blockage area closer to the channel wall allows further intensification of the existing flow recirculation and also generates the corresponding turbulent fluctuations leeward of the inserts. Correspondingly, such effects by plate tilting may be used as an alternative to reinforce the hydrodynamic and thermal mixing performance of a 2D planar space filling plate.

Table 11. Space filling inserts blockage ratios

Grid type	σ at $\beta = 0^\circ$	σ at $\beta = \pm 45^\circ$
CO	0.692	0.782
PSFG	0.314	0.515
NSFG	0.692	0.782

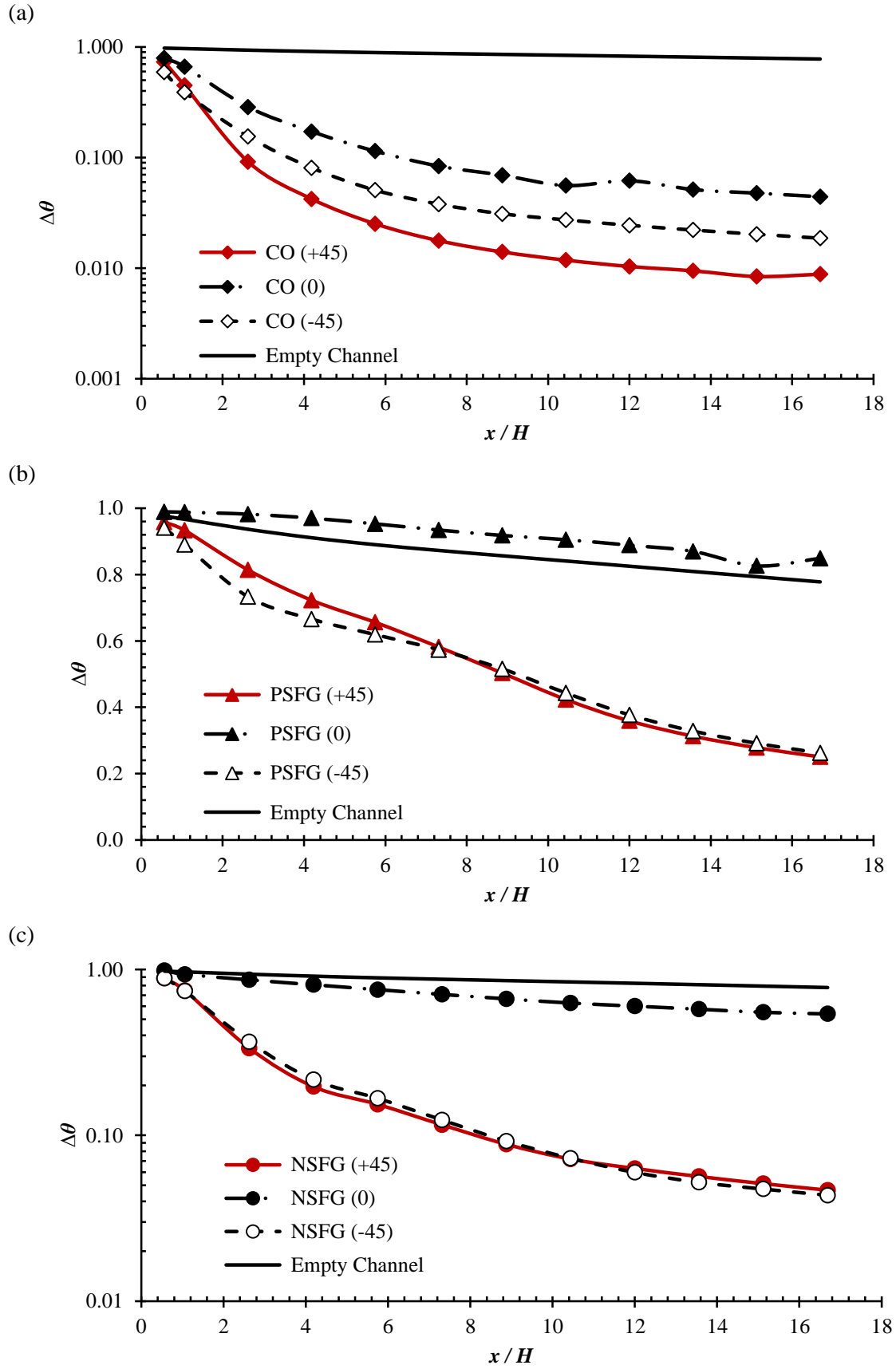


Figure 40. Dimensionless temperature differences among different inserts (a) CO, (b) PSFG, and (c) NSFG at different tilting angles β

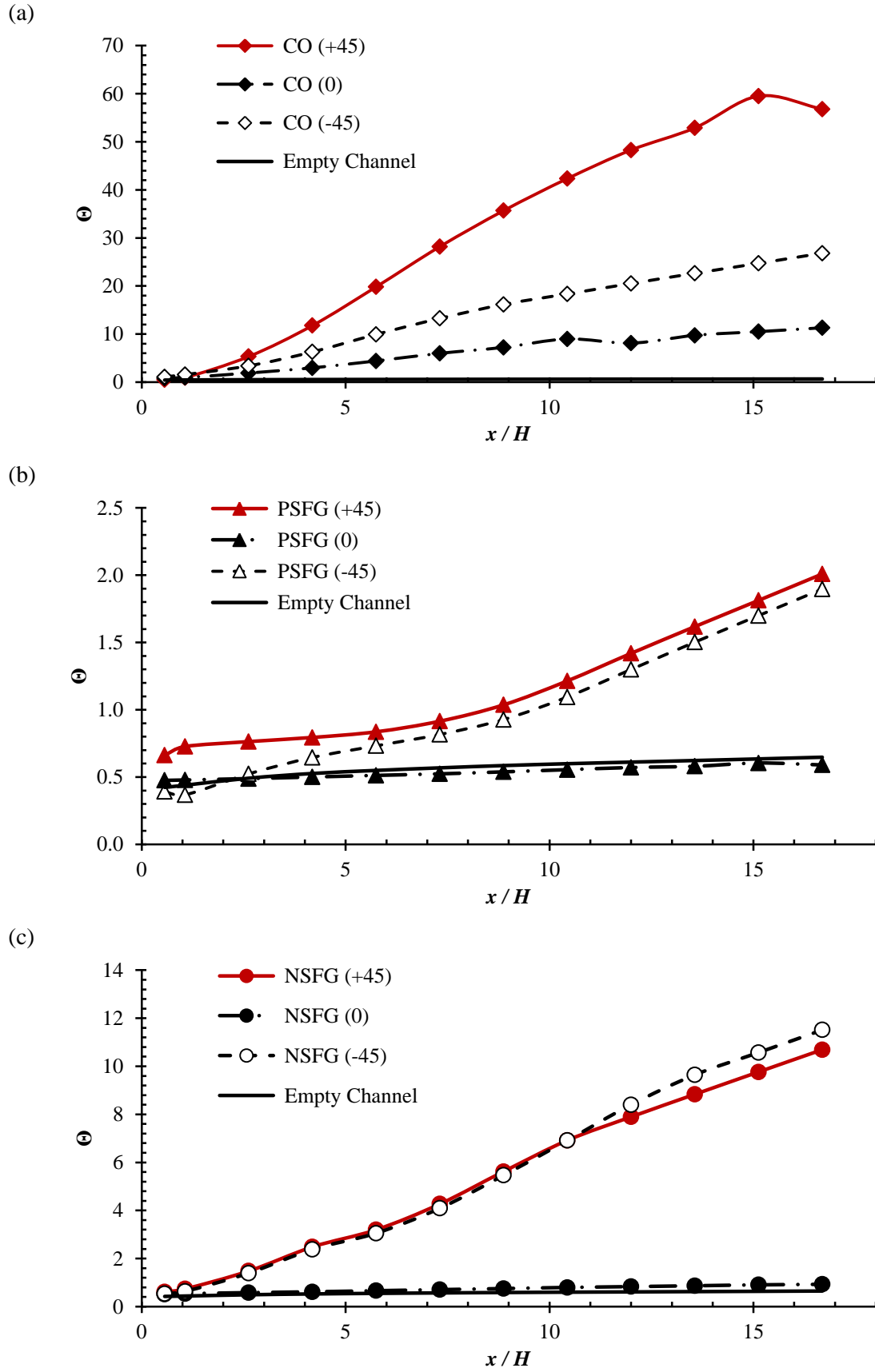


Figure 41. Thermal mixing performance among different inserts (a) CO, (b) PSFG, and (c) NSFG at different tilting angles β

Influence of turbulence kinetic energy with different space-filling inserts and tilting configurations

2D planar space filling insert geometry and the insert orientation play critical roles in shaping the thermal mixing capability of a HVAC free cooling or heating system. In order to quantify the insert induced hydrodynamic fluctuations upon thermal mixing, the present study numerically pairs the standard k - ε turbulence model with energy equation. Therefore, the generated turbulence energy i.e. the turbulence kinetic energy k can be known. The effects of space filling geometry with different tilt angles of the insert are numerically calculated and cross-sectional averaged k_{ave} as a function of x / H are compared and shown in *Figure 42*. The k_{ave} for an empty channel decreases immediately from $x / H = 0$ to further downstream, such effect is solely due the fluid flow interaction at the Tee. Undoubtedly, the k_{ave} for CO, NSFG, and PSFG at all β are higher than that in the empty channel, except for $\beta = 0^\circ$ PSFG which is most probably behave like an flow straightener, of which k_{ave} reduces 28% compared with the empty channel at $x / H = 0.6$. The k_{ave} for CO and NSFG at $\beta = 0^\circ$ increase from $x / H = 0$ to $x / H = 1.1$ and 2.6 respectively, which are then followed by decreasing k_{ave} further downstream. Remarkably, the positions of the maximum k_{ave} are rather consistent for all the titled cases, i.e. at $x / H = 2.6$. Such effects might be due to the typical increase in tilted plate area for each insert, which universally introduces equivalent order of flow recirculation with the correlated turbulent fluctuations. These flow recirculation are attached either along the upper or bottom region of the channel, and in the lee of every insert. Most importantly, observations show that the k_{ave} for all cases at $\beta = -45^\circ$ is greater or almost equivalent than inserts positioned at $\beta = +45^\circ$, albeit the opposite consequence was shown earlier with Θ . Thus, this strongly confirmed that channelling of the cooler air toward the warmer stream with $\beta = +45^\circ$ has very effective thermal mixing abilities. The k_{ave} for CO is the highest among all the 2D planar space filling plates positioned at $\beta = +45^\circ$, which is 234%, 579%, and 2817% higher compared with NSFG, PSFG, and the empty channel, respectively at location $x / H = 2.6$ downstream of the inserts.

The cross-sectional histograms for k at $x / H = 2.6$ and $Re_H = 2.19 \times 10^4$ with the three different insert tilted angles for CO (area shaded in red), PSFG (area shaded in blue), and NSFG (area shaded in green), are presented as *Figure 43*. CO is able to produce the highest and largest range of k , which is followed by NSFG and then by PSFG. Such outstanding turbulence generation capability by CO might be due to the reason that the circular geometry orifice is allocated toward

the central region of the channel cross-section, which permits the upstream flow to be rather selective while flow pass through. More importantly, the build-up of flow recirculation around CO greatly promotes higher fluid flow fluctuations, thus higher k . Consequently, CO is more effective than the fractal geometries inserts used in this phase of the study, albeit that NSFG is having the same σ as CO. Remarkably, the extracted histogram can be considered as the unique characteristic for each 2D space filling insert in turbulence generation. *Figure 43* shows the generated histograms patterns for PSFG and NSFG are almost similar. Above all, the generated flow fluctuations are enhanced at $\beta = \pm 45^\circ$. Moreover, by comparing with PSFG, CO and NSFG are able to generate higher k once tilted. Therefore, such effects proven that by tilting the insert, thermal mixing performance for all the present cases can be restructured or be enhanced.

In spite of the exact spatial locations of higher k , the area-averaged turbulence energy generated, as well as the induced k scaling in terms of size and range across the channel cross-sections have been discussed in *Figure 42* and *Figure 43*. *Figure 44* represents the space filling inserts induced flow recirculation at the vertical mid-section i.e. $z / H = 0.5$ together with the associated turbulence kinetic energy and the calculated results of CO and NSFG at $\beta = 0^\circ$ and $+45^\circ$ are compared. The two bars below represent the value bar for velocity (a-d) and turbulence kinetic energy (e-h) respectively. Noticeably, due to the disturbance at the T -duct, the generated flow recirculation is non-symmetrical. As displayed in *Figure 44(a-h)*, it is key to note that there is a direct relationship between the insert induced flow recirculation with the higher turbulence kinetic energy produced, of which the latter is involved closely with former. Furthermore, turbulent intensity are greater in higher k coverage for non-tilted CO, which is followed by CO positioned at $\beta = +45^\circ$, then by NSFG at $\beta = +45^\circ$, and lastly the upright NSFG. Interestingly, the k generated leeward of the non-tilted NSFG is greatly restricted by the smaller non-filled slit areas possesses by the fractal geometry, however when tilted by $\pm 45^\circ$ the thermal mixing performance is substantially enhanced. Consequently, this indicates that the gain in extended surface area promotes flow recirculation and hence fortifies the k generation [see *Figure 44(d)* and (h)].

While tilting NSFG, its thermal mixing performance is still much lower than its tilted CO counterpart. Hence, it is vital to observe the flow characteristics along the horizontal mid-plane at $y / H = 0.5$ $\beta = 0^\circ$ and $+45^\circ$ between CO and NSFG, as shown in *Figure 45*. Results suggest that there are two types of flow recirculation being built up in the lee of CO, i.e. the primary and

secondary recirculation regions [see *Figure 45(a)*]. Interestingly, the flow structures are symmetrical, which may result the associated turbulence kinetic energy generated being doubled and attached closely with the primary or larger flow recirculation [see *Figure 45(c)*]. In contrast, as shown in *Figure 45(b)*, NSFG allows the upstream flow to pass through rather smoothly. The higher k as shown in *Figure 45(d)* is merely due to the flow fluctuations generated by the extended surface proximity to the channel wall beneath. Thus, 2D planar space-filling CO, being fully covered by the higher k , resulting its thermal mixing outperforms NSFG.

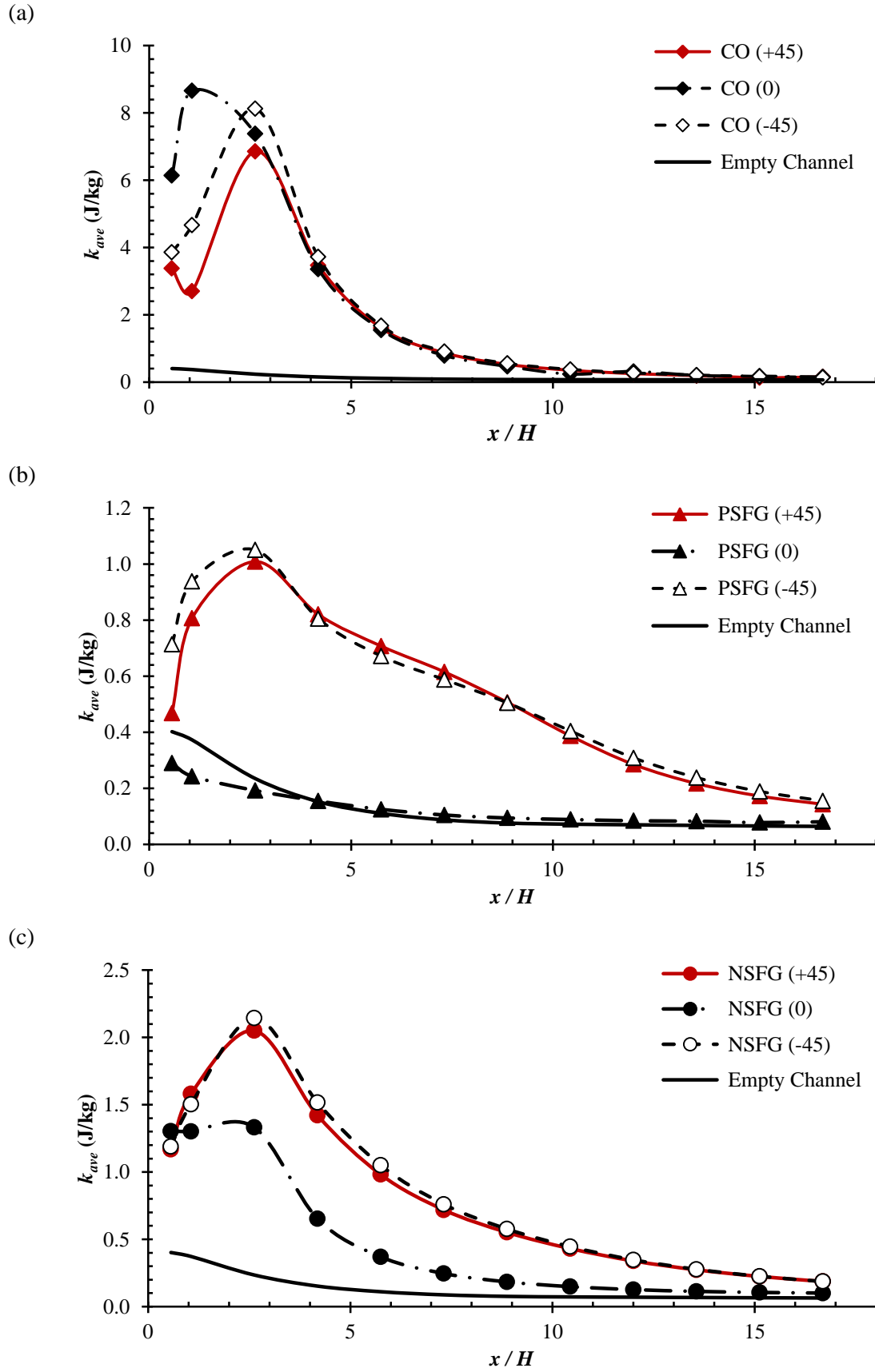


Figure 42. Cross-sectional averaged turbulence kinetic energy among different inserts (a) CO, (b) PSFG, and (c) NSFG at different tilting angles β

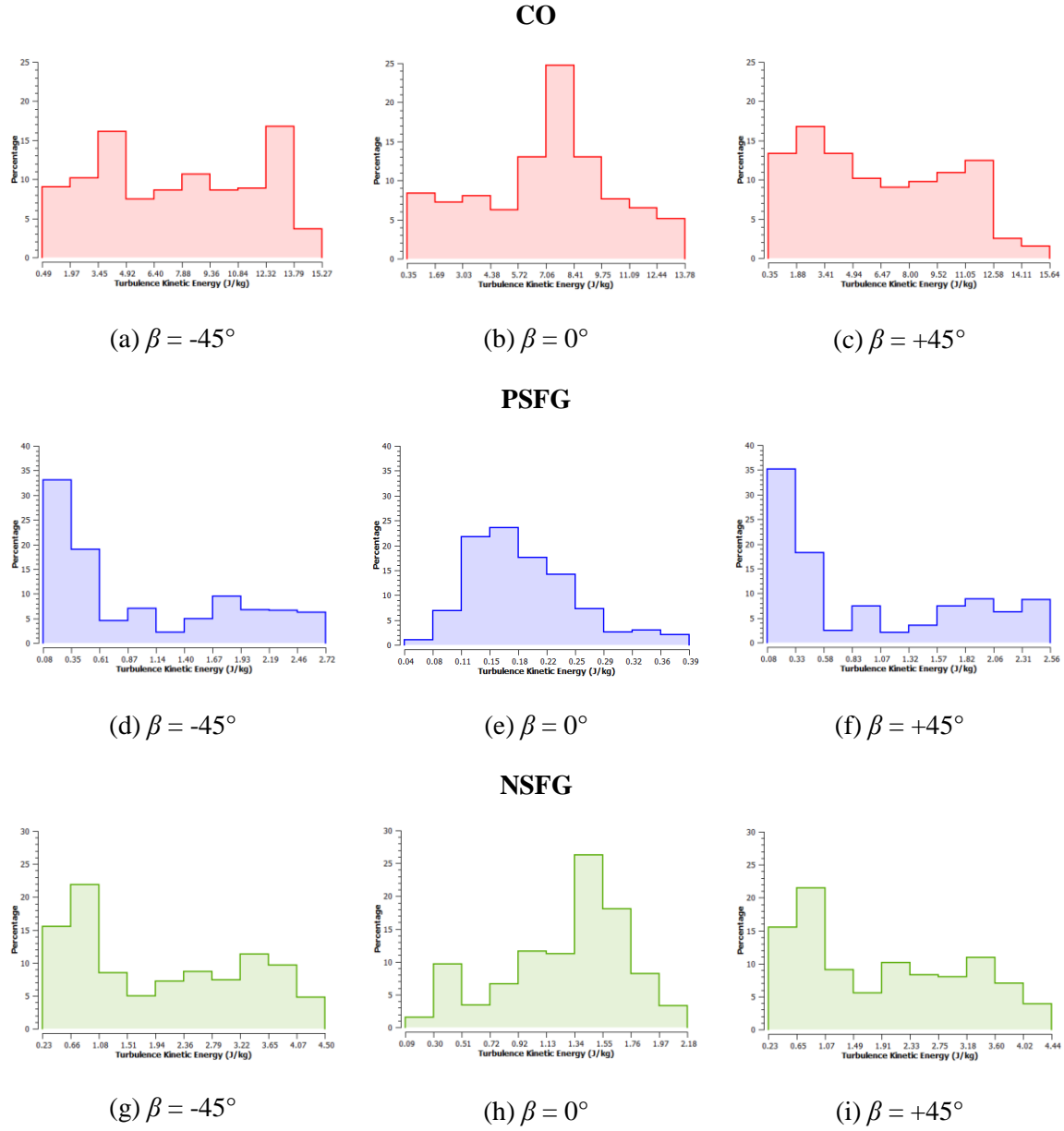


Figure 43. Histogram for cross-sectional turbulence kinetic energy k at location $x/H = 2.6$ for different tilting angle β for CO (a-c), PSFG (d-f), and NSFG (g-i)

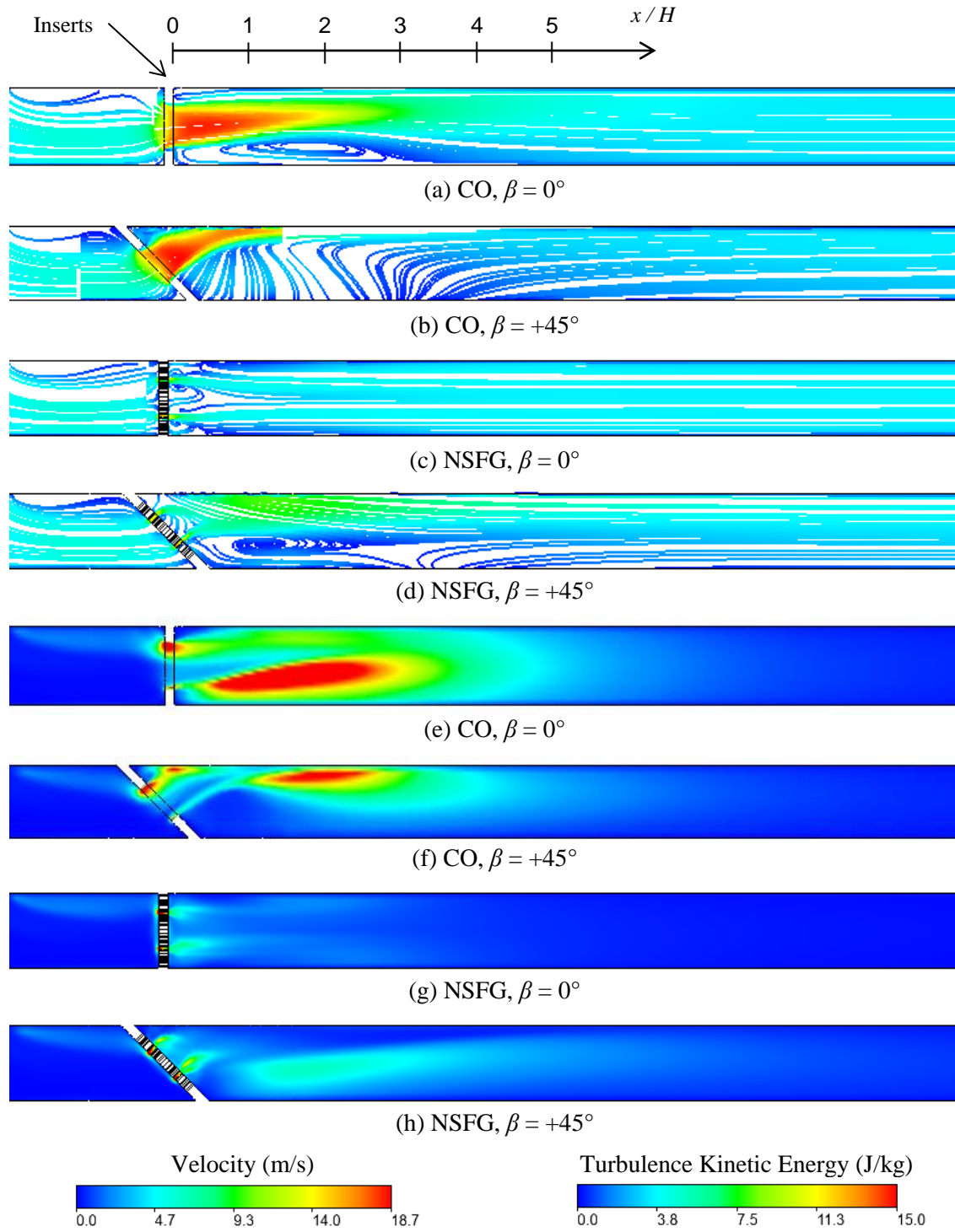


Figure 44. Cross-sectional $z/H = 0.5$ velocity streamline and turbulence kinetic energy in the thermal mixing chamber at for CO (a, b, e, f) and NSFG (c, d, g, h)

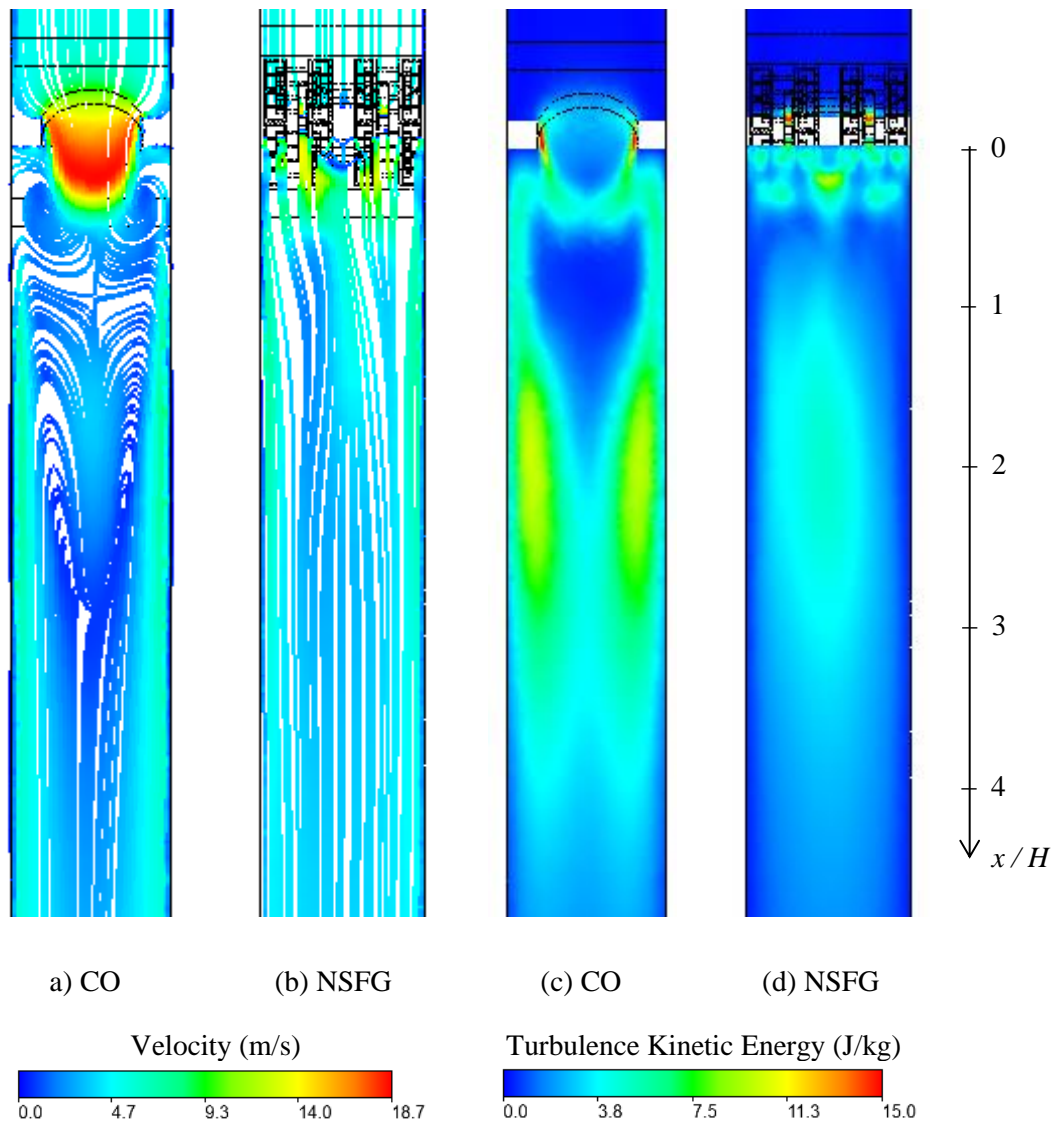


Figure 45. Tilting effect of space-filling inserts on the generation of flow recirculation velocity streamline (a, b) and turbulent kinetic energy k (c, d) in the lee of the inserts at $\beta = +45^\circ$ and $y/H = 0.5$

Vertical velocity profiles at several location downstream at $z / H = 0.5$ for CO and NSFG inserts for all tilting configuration

After the Tee, the flow and temperature profile in a hybrid HVAC free-cooling or heating system are essentially non-uniform and not thoroughly mixed before reaching the HVAC heat exchanger. Such non-uniformities in flow and temperature profile at the inlet of the heat exchanger may lead to performance reduction in the heat exchanger effectiveness and may increase pressure drop (Bury, 2012; L. Z. Zhang, 2009). *Figure 46* and *Figure 47* show the $z / H = 0.5$ normalised vertical velocity and dimensional temperature profiles respectively, at various location along $x / H = 4.2, 7.3, 10.4, 13.6,$ and 16.7 downstream of CO and NSFG. Two different insert tilt angle at $\beta = 0^\circ$ and 45° are discussed. As presented in *Figure 46(a-d)*, the flows are initially non-symmetrical at $x / H = 4.2$, however the flows eventually form fully developed profiles at downstream distance $x / H = 16.7$ for all cases. It seems that even at the furthest downstream $x / H = 16.7$, the velocity profiles for the tilted space filling inserts are not able to attain fully symmetrical. The determination of non-symmetrical flow profile can be justified by comparing the velocity deviation at $y / H = 0.2$ and 0.8 along $z / H = 0.5$. It is found that the fluid flow profile for NSFG at $\beta = 0^\circ$ are well symmetrical, with the velocity deviation at both defined locations are the lowest i.e. 0.2%. It is followed by $\beta = 0^\circ$ CO at 1.0% deviation, then by 11.6% for $\beta = +45^\circ$ CO, and lastly 18.4% for $\beta = +45^\circ$ NSFG. While NSFG at $\beta = 0^\circ$ possesses the most symmetrical flow profiles, it is important to note that the thermal mixing performance Θ of CO at $\beta = 0^\circ$ is 1120% greater than the NSFG. NSFG Θ is able to improve up to 1054% while tiled at $+45^\circ$. However it is still 431% lower than CO at the same β . Thus, the justification of favourable velocity uniformity needs to take into account together with the corresponding thermal mixing performance.

Regarding temperature uniformity, it is evidently shown in *Figure 47(a-d)* that CO with $\beta = +45^\circ$ is able to attain outstanding temperature uniformity downstream the channel at $x / H = 16.7$, with maximum temperature difference at $z / H = 0.5$ along y/H is 0.11K. Additionally, the maximum temperature variation is 0.45 K for $\beta = +45^\circ$ NSFG, 0.55 K for $\beta = +45^\circ$ CO, and 9.2K for $\beta = 0^\circ$ NSFG. Remarkably, $\beta = +45^\circ$ CO could achieve effective temperature uniformity even at $x / H = 7.3$ with a maximum temperature variation of 0.73K, which can also be justified to be the lowest among the other inserts at the same position. By taking into consideration of all the 2D planar

space filling inserts performance with their capabilities in attaining temperature and velocity uniformities downstream of the channel, it is apparent that both CO at $\beta = 0^\circ$ and 45° outperform the rest in effective thermal mixing enhancement.

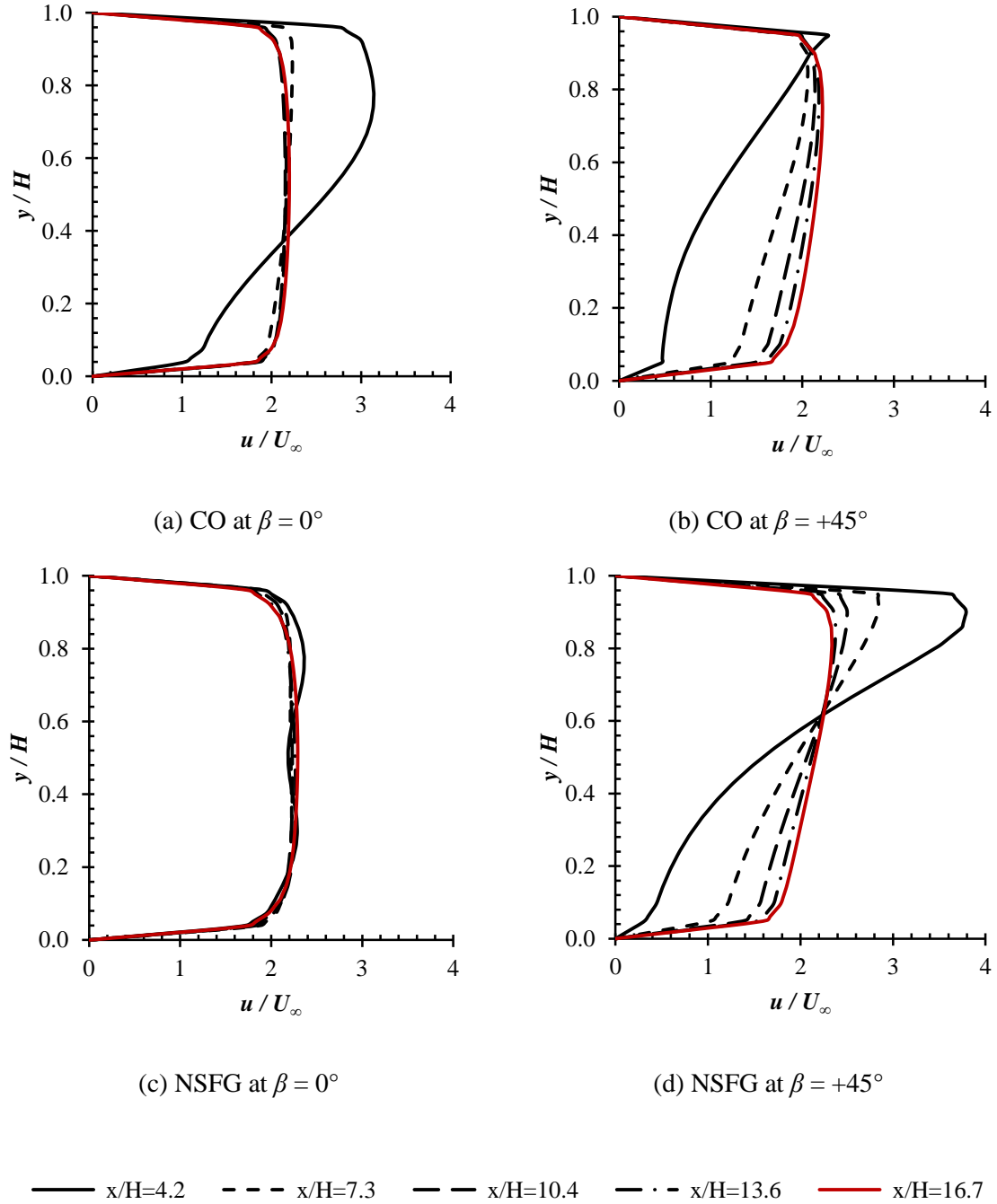


Figure 46. Dimensionless vertical velocity profiles at $z/H = 0.5$ for CO insert (a, b) and NSFG insert (c, d) at tilting angle $\beta = 0^\circ$ and $+45^\circ$

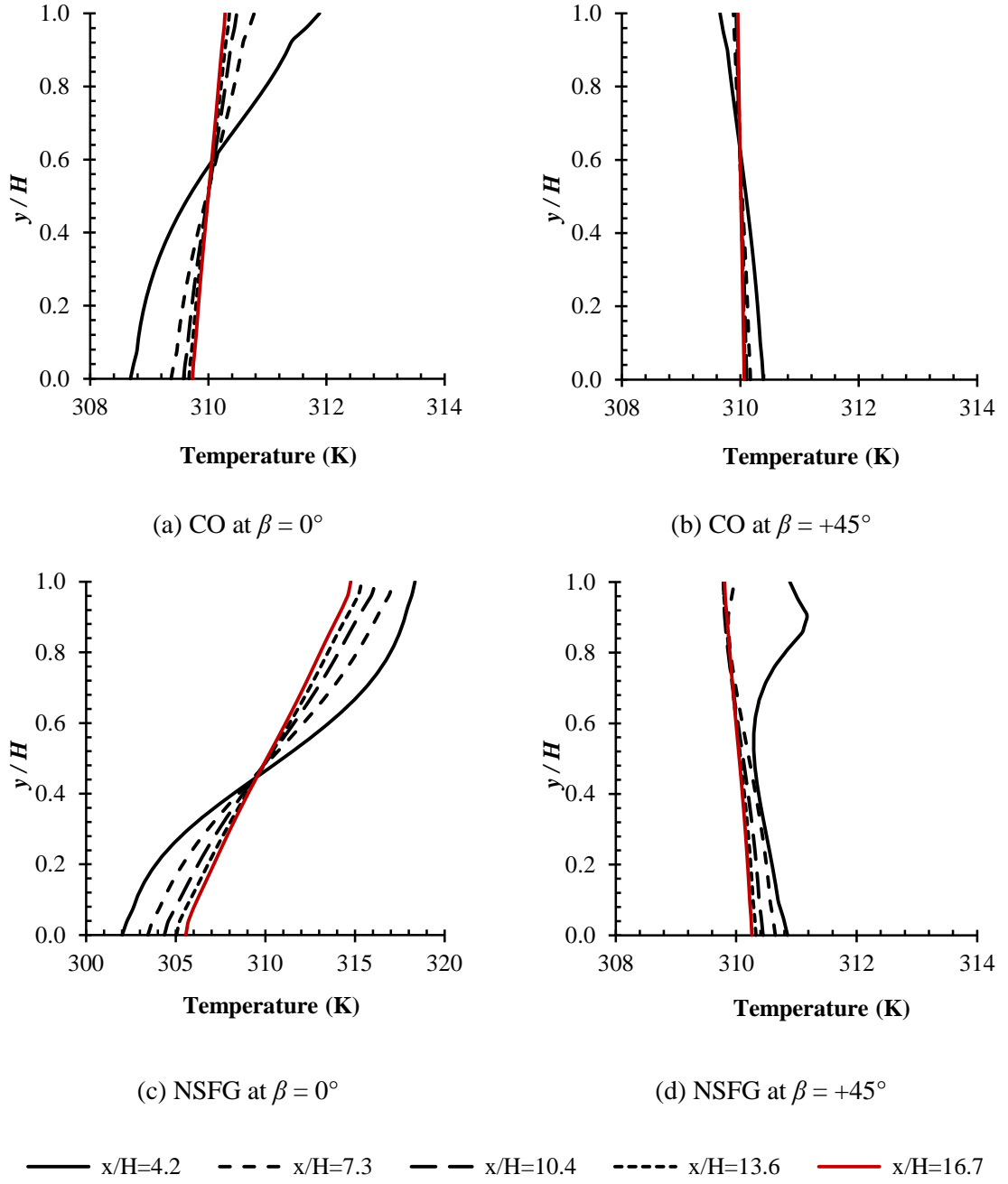


Figure 47. Vertical temperature profiles at $z/H = 0.5$ for CO insert (a, b) and NSFG insert (c, d) at tilting angle $\beta = 0^\circ$ and $+45^\circ$

Pressure drop and system performance of the various inserts

The effective hydrodynamic and thermal mixing can be enhanced by generating a well-controlled turbulence in the flow. However, the pressure coefficient may be affected and subsequently the cost of pumping power increases. In order to attain favourable thermal mixing performance for a hybrid HVAC economiser with considerable economic pumping power, a sustainable space filling configuration is desired. The normalised pressure drop for each insert positioned at 3 different tilted angles are evaluated and is shown in *Figure 48*. ΔP is normalised with respect to the empty channel pressure drop ΔP_{EC} . Visibly, inserts of all types with $\beta = -45^\circ$ possess the highest ΔP compared to their similar counterparts oriented at $\beta = 0^\circ$ and $+45^\circ$. This comes to ΔP is the highest for $\beta = -45^\circ$ CO, followed by NSFG and PSFG of the same tilt angle. Similarly, the same trend can be observed for plates positioned at $\beta = +45^\circ$. On the other hand, the pressure drop for NSFG which is placed at $\beta = 0^\circ$, is higher than CO of the same tilt angle. The increase in ΔP for tilted inserts could be explained due to the increase in blockage area (see *Table 11*) which induce additional flow disturbance. To summarise, the ΔP is 3.6% lower for CO at $\beta = 0^\circ$ when compared to NSFG positioned at the same β , and CO is 6.5% and 6.8% higher than NSFG at $\beta = -45^\circ$, and $+45^\circ$, respectively. Hence, the changes in ΔP for CO are not as significant.

The definition for system performance η of the space filling insert induced thermal mixing can be described as the ratio of Θ over pressure coefficient. The equation defines the relative cost of pressure drop (pumping power) to attain a certain rate of thermal mixing. It is important to note that only cases with outstanding Θ are chosen and compared. the relative overall system performance of 2D planar space filling plate for CO and NSFG at different β are shown as *Figure 49*. Results show that CO outperforms NSFG at all tilted position evaluated in this study, of which the former is $8.7\times$ higher than NSFG at $\beta = 0^\circ$, it is $2.4\times$, and $5.4\times$ higher at $\beta = -45^\circ$ and $+45^\circ$, respectively. Therefore, the current results suggest that maximum system performance can be secured with orifice configuration, and more importantly, the thermal mixing performance could be substantially enhanced via plate tilting in promoting additional turbulent fluctuations.

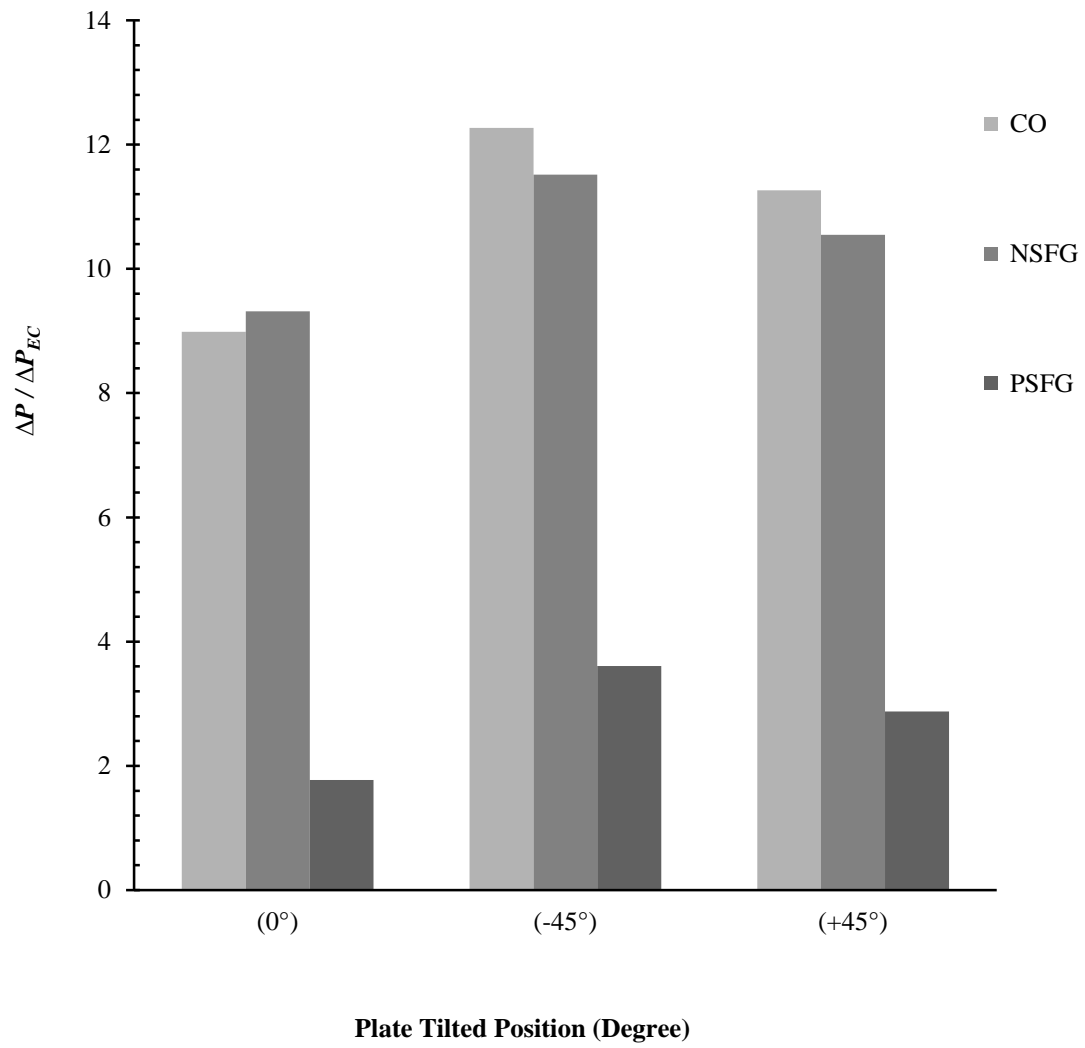


Figure 48. Normalised pressure drop of each inserts over pressure drop of empty channel at $\beta = 0^\circ$, -45° , and $+45^\circ$

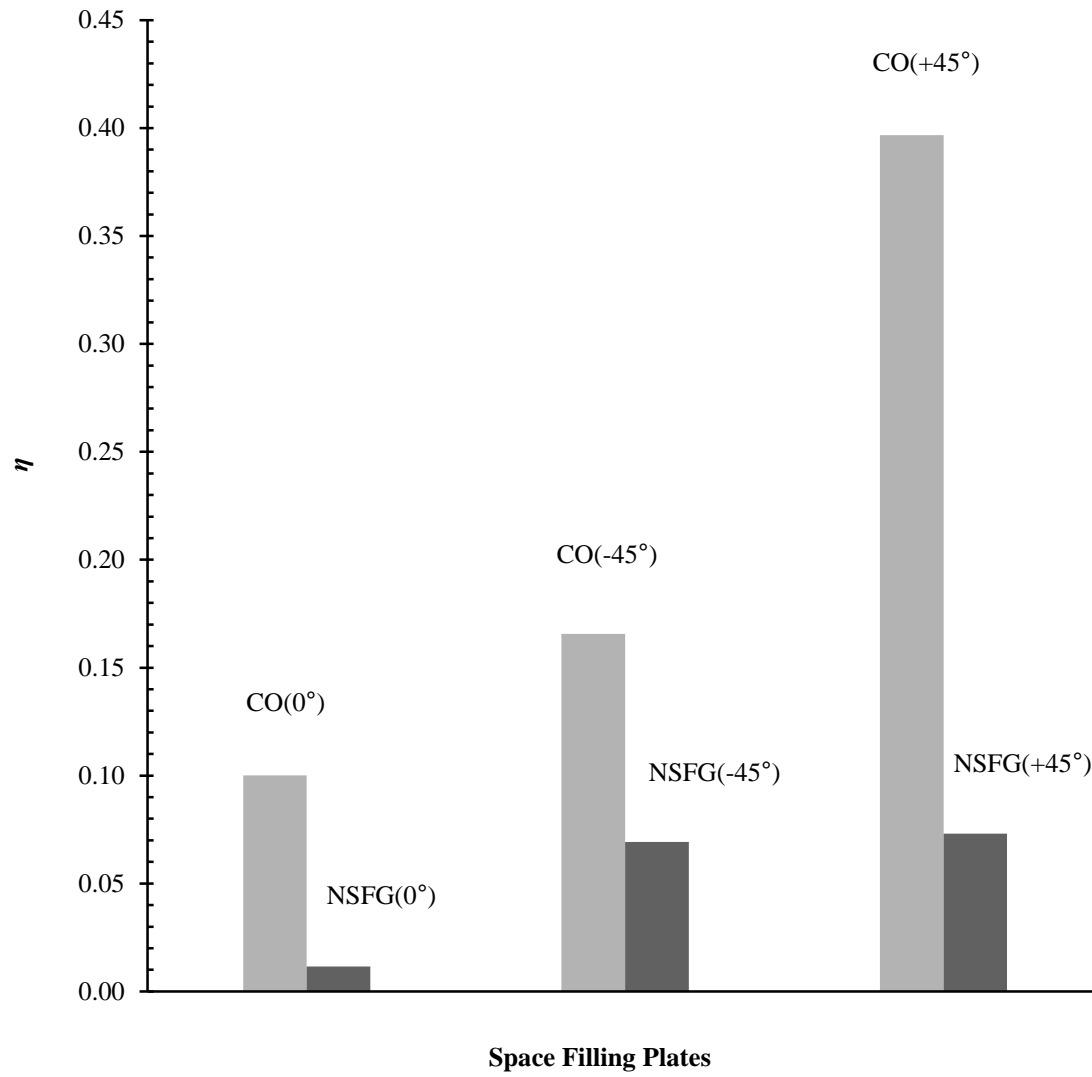


Figure 49. System performance η between CO and NSFG inserts

Chapter summary

3D, steady-state, and incompressible turbulence generated by 2D planar space filling inserts within a T -duct are numerically investigated to evaluate their thermal mixing characteristics at various tilted angles. System performances are compared between circular orifice and space filling square fractal grids. The conclusions of this study are:

1. Higher fluid flow fluctuations or turbulence kinetic energy attached intently with the blockage induced flow recirculation in the lee of the space filling plate. By further increasing the inserts blockage ratio from $\sigma = 0.692$ to 0.782 at $Re_H = 2.19 \times 10^4$ via plate tilting of either $\beta = +45^\circ$ or -45° enables the promotion of turbulence to larger values and wider ranges of flow undulations. As a result, the thermal mixing performance of the 2D planar space filling plate can be greatly enhanced.
2. Although fractal inserts is capable of producing prominent localised fluid flow fluctuations, CO is being fully surrounded by flow recirculation downstream of the insert empowers globalised turbulent mixing. More specifically, the insert-generated primary flow recirculation is able to produce much larger turbulent length scales to amplify the flow undulations. Hence, despite having the same blockage ratio, the $\pm 45^\circ$ tilted CO substantially outperforms the rest of the space filling square fractal plates i.e. PSFG and NSFG in hydrodynamic and thermal mixing.
3. Non-tilted CO possesses lower pressure drop than that for the NSFG. However, once tilted the former ΔP is then higher. It is important to note that the increases in ΔP for all tilted CO are lower than 7% compared with NSFG. Thus, with CO exceptional fluid flow fluctuation characteristics, the system performance η can be substantially strengthened. To conclude, it is crucial to note that apart from CO excellent thermal mixing performance, CO rather simple circular geometry is able to automatically support manufacturing sustainability as well as resource efficiency upon mass production, compared with either of the PSFG or NSFG. In particular, the requirements in electricity consumption, manufacturing duration and production cost invested can be significantly cut down.

PART B: Suggested Declaration for Thesis Chapter 6

[This declaration to be completed for each conjointly authored publication and to be placed at the start of the thesis chapter in which the publication appears.]

Monash University

Declaration for Thesis Chapter 6

Declaration by candidate

In the case of Chapter 6, the nature and extent of my contribution to the work was the following:

Nature of contribution	Extent of contribution (%)
Main author, construction of wind tunnel, compiling results, contributes constructive comments, insights, and analysis towards the results and discussion this paper.	33%

The following co-authors contributed to the work. If co-authors are students at Monash University, the extent of their contribution in percentage terms must be stated:

Name	Nature of contribution	Extent of contribution (%) for student co-authors only
Chin Kee Wen	Undergraduate, experiment results.	33%
Teh Eng Khim	Undergraduate, numerical prediction results.	33%

The undersigned hereby certify that the above declaration correctly reflects the nature and extent of the candidate's and co-authors' contributions to this work*.

**Candidate's
Signature**

	Date 14/09/2015
---	------------------------

**Main
Supervisor's
Signature**

	Date 14/09/2015
---	------------------------

*Note: Where the responsible author is not the candidate's main supervisor, the main supervisor should consult with the responsible author to agree on the respective contributions of the authors.

CHAPTER 6 – RESULTS AND DISCUSSION : PHASE 3

Thermal mixing enhancement after a *T*-duct with a fractal orifice insert

This chapter presents the results for phase three of the present study. Previous two phases have proven orifice type inserts performed better than grid type inserts. Hence, this phase of the study investigates the application of fractal features onto orifice inserts and gauges its thermal mixing performance and system performance against non-fractal orifice inserts.

Validation of numerical validation

Measured centreline velocities from [Nicolleau et al. \(2011\)](#) experimental results are first employed to validate the current CFD $k-\varepsilon$ turbulence model. In their studies, the measurements were made and recorded after the air flow passes through each orifice plate of different premeditated geometries. Most importantly, the hydrodynamic performances of the four different orifice patterns i.e., circular, triangular, s1f1, s1f2, as well as the smooth empty channel were individually investigated within a circular wind tunnel of inner diameter 140.8 mm, blockage ratio 0.66, and inlet velocity 5 m/s. Highly sensitive and accurate hotwire anemometry was employed and used to collect the flow velocities. *Figure 50(a-d)* show the centreline flow velocity changes downstream of the channel induced by a variety of control and fractal orifice plates. Clearly, the present numerically simulated centreline velocity distributions of each insert, as well as the control empty channel, are in good agreement with the earlier experimental measurements.

HVAC free-cooling system is mainly fabricated using rectangular channel and it is also important to note the recycled warm air is always channelled perpendicularly into the main duct. The present numerical study aims to investigate the thermal mixing performance of HVAC free-cooling system with the insertions of static mixing orifice inserts of various geometries at a fixed distance downstream of a *T*-duct (see *Figure 24* for details). , The comparisons between the current experimentally measured and numerically modelled normalised centreline velocity as well as the temperature distributions downstream of the Tee without insert are presented in

Figure 51. The symbols denote the measurements obtained experimentally and lines for the simulated results respectively. Visibly, the air temperature decreases with a gradual increase in calculated velocity downstream of the channel. Good correlations can be made between the experimental data and numerical results. The numerical validations of centreline velocity and temperature distributions for CO, SO, SFO, and KSFO downstream of the channel, based on the time series experimental measurements are presented as *Figure 52* and *Figure 53* – the shaded zones represent the domain upstream of the orifices. It is observed that there are increasing hydrodynamic and thermal undulations when approaching $x = 0$ where $x = 0$ marks the position when working fluid departs from the orifice. Hence, it is reasonable to say the orifice generates fluid flow and thermal fluctuations in both before and after the orifice plate. As portrayed in *Figure 52*, the centreline air velocity escalates to maximum and subsequently decaying further downstream. The calculated maximum velocity for CO, SO, and KSFO falls into about the same regime, although SFO is 24.2% lower than CO. Interestingly, the unique fractal characteristics can be observed in *Figure 53(c)* and (d), whereby both of the experimental and numerical results exhibit unequivocal thermal oscillations immediately after $x = 0$. In addition, the percentage (%) of temperature variations between the mean of each experimentally recorded data and the corresponding numerically predicted results along the thermal mixing channel at $x \geq 0$, are depicted in *Figure 53(a-d)*. Clearly, the differences are mostly far lower than 9.7%. As the results suggest the current experimental and numerical data are well within reasonable agreement with each other in both centreline velocity and temperature distributions.

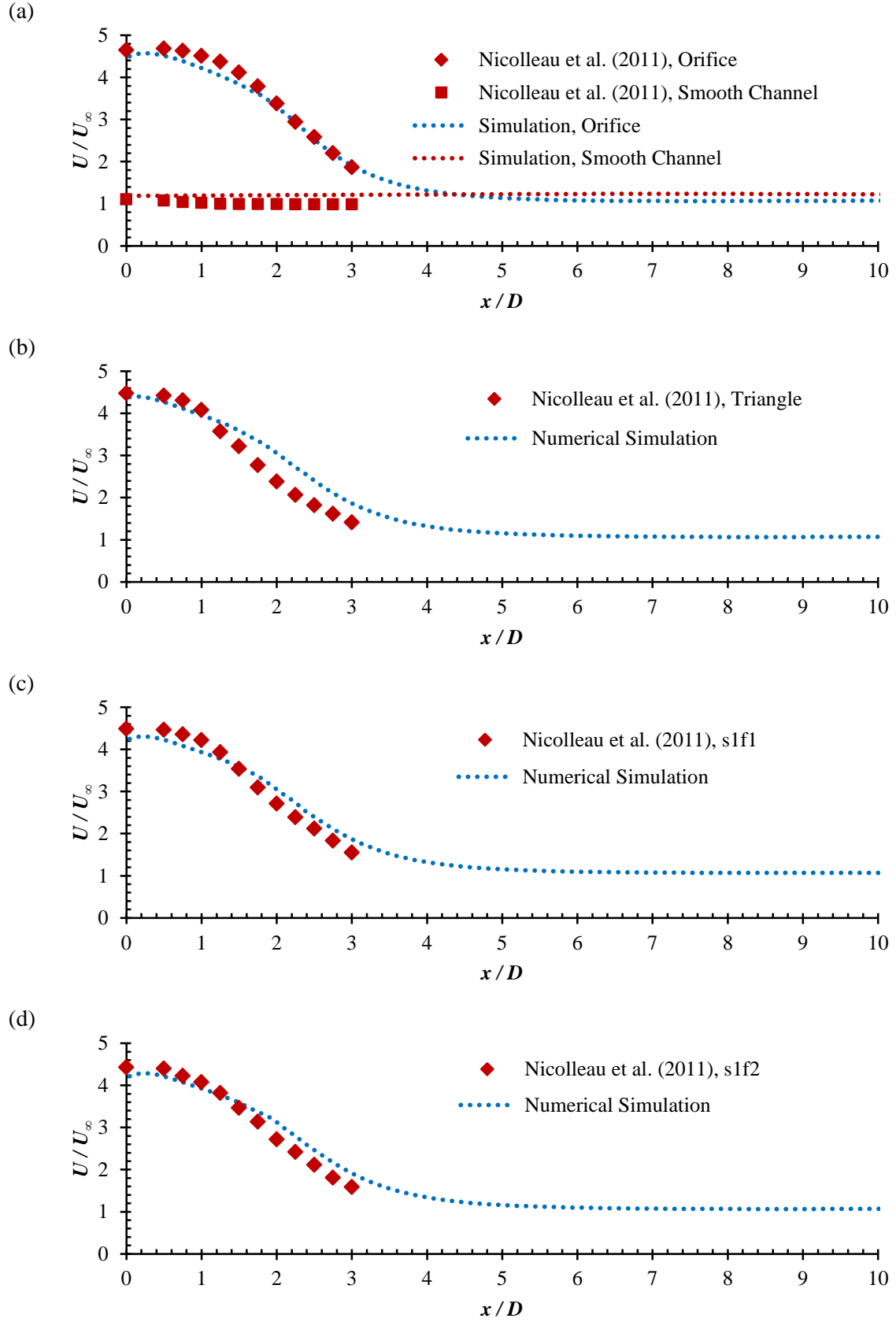


Figure 50. Numerical validation of centreline velocity downstream of each insert using (a) empty channel and circular orifice, (b) triangular orifice, (c) s1f1, and (d) s1f2. (Nicollet et al., 2011)

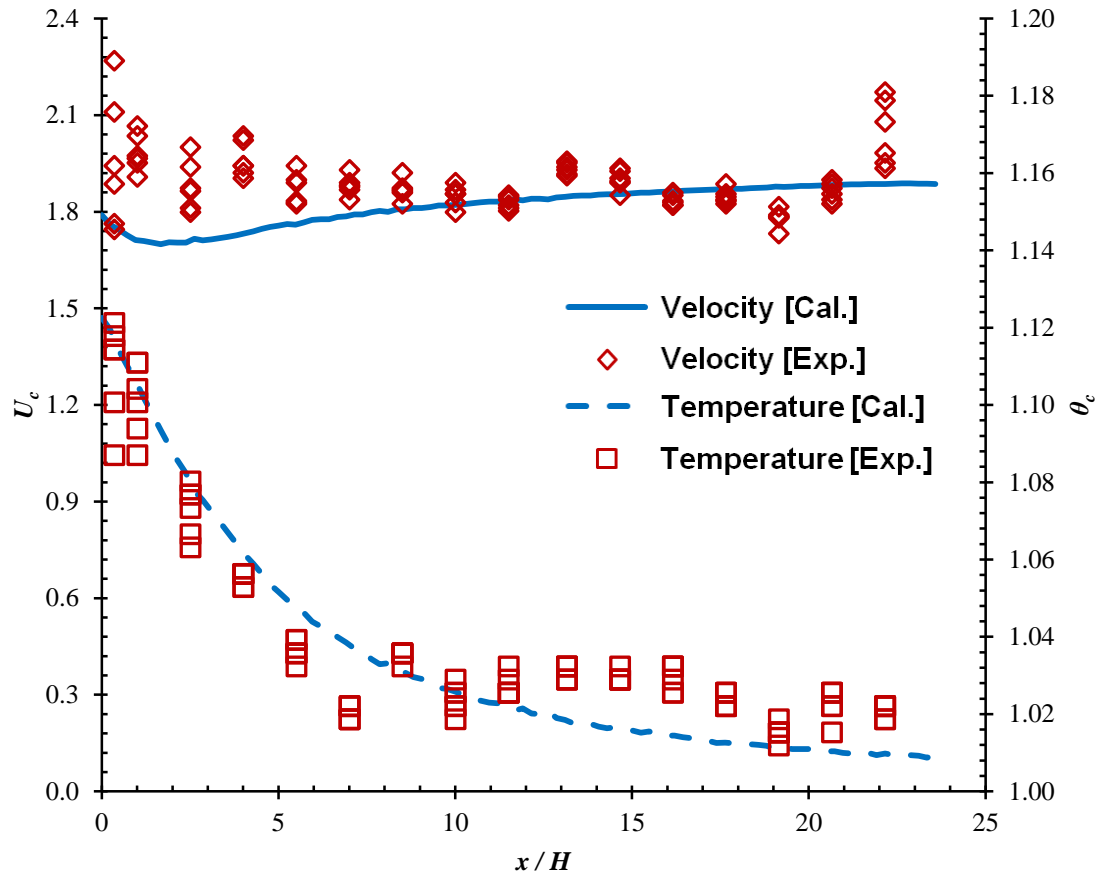


Figure 51. Numerical validation using empty channel centreline velocity and centreline temperature downstream of the Tee joint test section

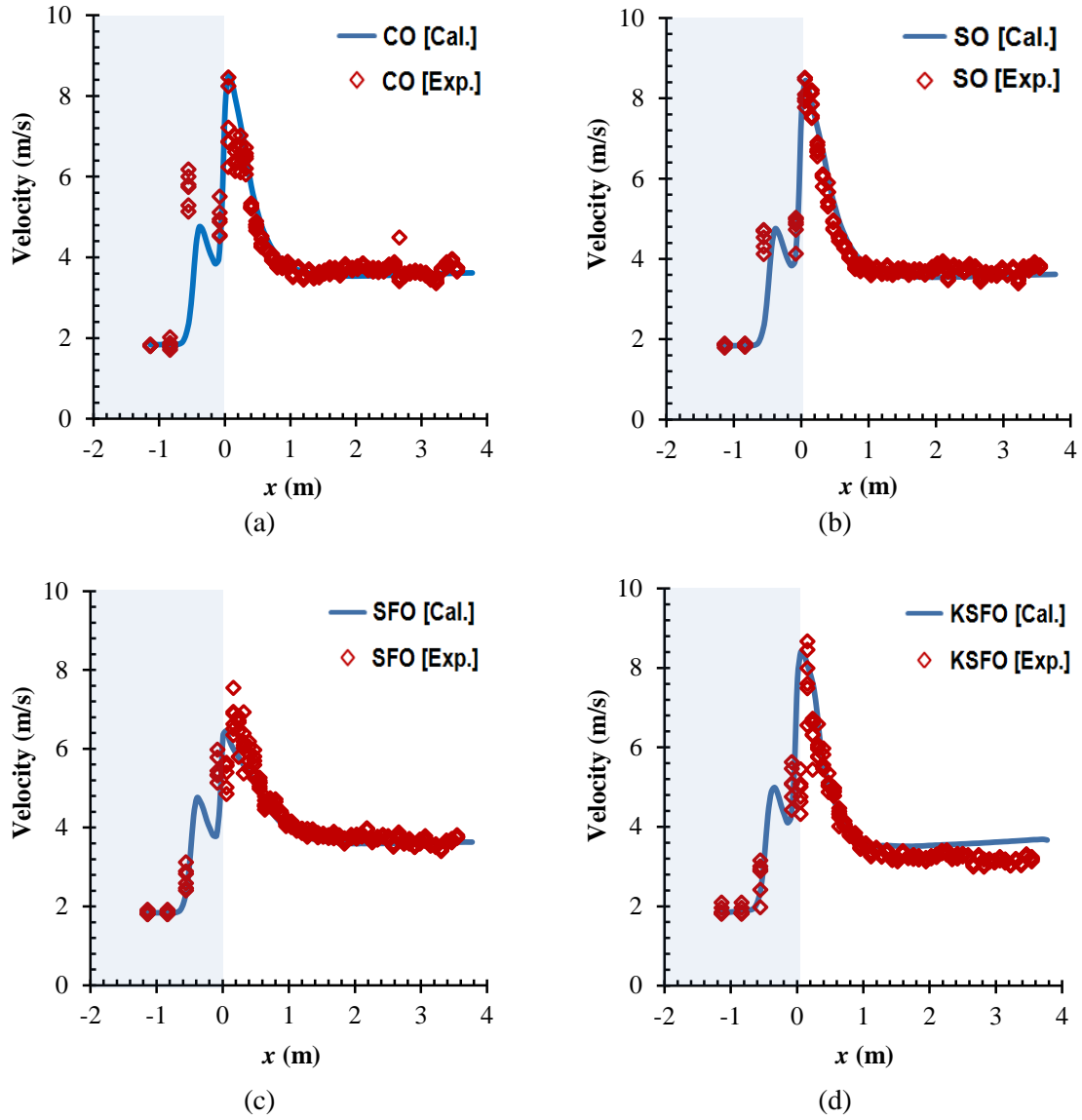


Figure 52. Numerical validation using centreline velocity in the lee of various insets (a) CO, (b) SO, (c) SFO, and (d) KSFO

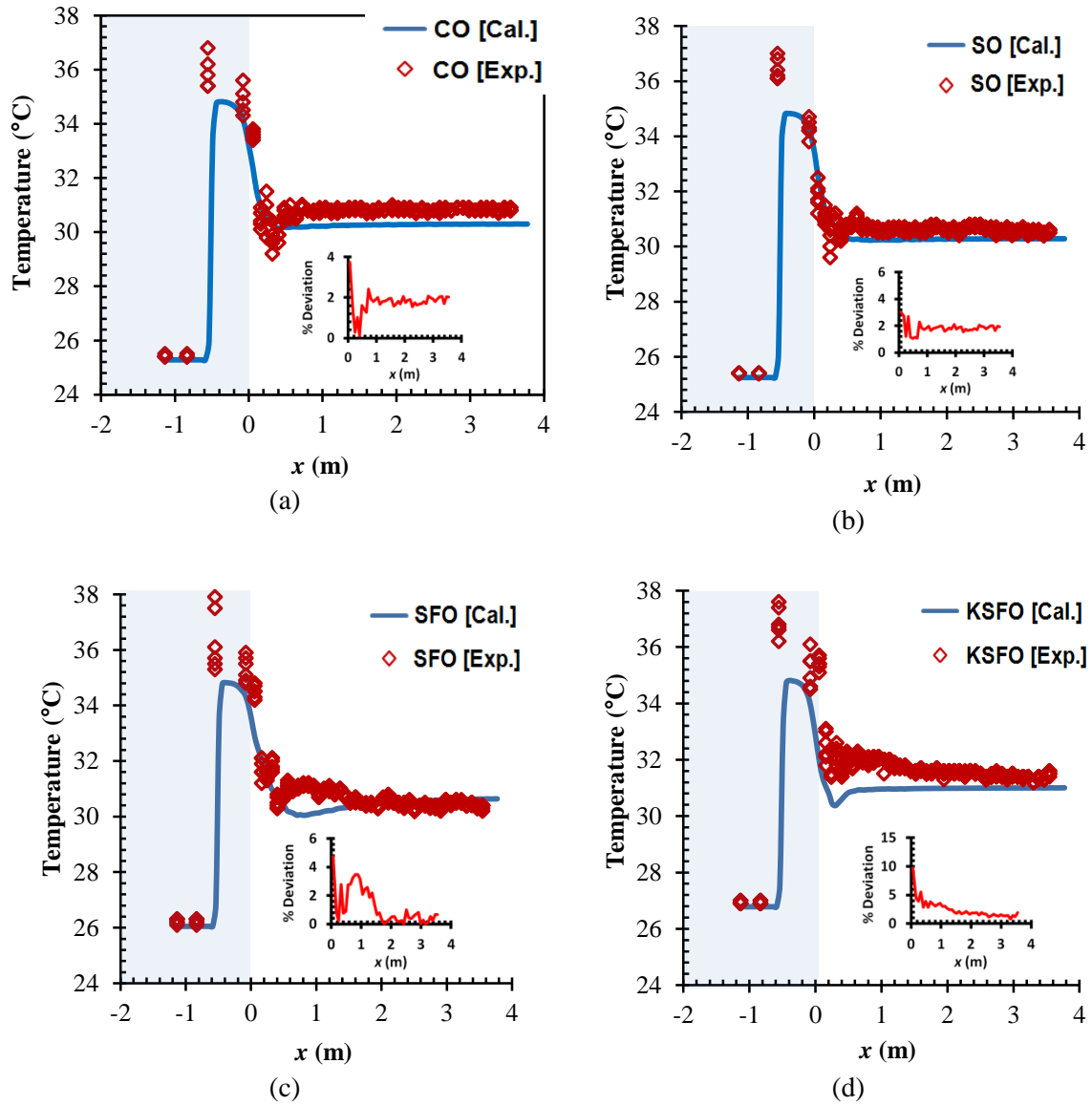


Figure 53. Numerical validation using centreline temperature in the lee of various insets (a) CO, (b) SO, (c) SFO, and (d) KSFO

Thermal mixing performance of the different inserts

In HVAC, indirect airside free-cooling system permits the transfer of thermal energy through air to air heat exchanger, and inhibits the mixing process from disturbing the indoor environment. The quality of premixed working fluid between the recycled warm air and surrounding cooler air is of great importance in order to enhance the heat transfer rate of HVAC heat exchanger. Evidently, a good thermal mixing depends strongly on the realisation of cross-sectional velocity and temperature uniformity downstream of the orifice (Chiou, 1978; Mishra et al., 2008). The normalised cross-sectional area-averaged temperature distributions θ at various locations leeward from each orifice are represented as *Figure 54(a)*. Reasonably, $T_{A,ave}$ is expected to be lower for an outstanding thermal mixing process. Hence, this shall lead to higher θ . As presented in *Figure 54(a)*, CO, SO, and KSFO outperform the rest between $0 \leq x/H \leq 2.6$, whilst beyond $x/H = 2.6$, SFO is higher. Clearly, the results seemingly suggest that SFO edge self-similarity may offer a new approach in generating turbulence, by breaking down of the larger fluid flow recirculation usually found downstream of an orifice into smaller forms. Yet, the effectiveness of SFO may only be at locations nearer to the surrounding walls.

Figure 54(b) represents the normalised maximum and minimum temperature difference $\Delta\theta$ of each cross-section downstream of the orifice. Results show that the $\Delta\theta$ decreases downstream of the channel for all cases. Remarkably, KSFO exhibits the lowest changes in $\Delta\theta$ along the thermal mixing chamber, where the $\Delta\theta$ at $x/H = 2.61$ is 17.1%, 18.7%, 42.9%, and 48.2% lower than CO, SO, SFO, and the empty channel without insert respectively. It is observed on the CO and SO cases, that larger flow recirculation may serve as an important factor to improve the thermal mixing performance. Furthermore, KSFO complex self-similarity edge surrounding the orifice perimeter seemingly is capable of further enhancing the existing large hydrodynamic recirculation usually found around the orifice-liked insert. It seems that the selection of base fractal pattern at $N = 1$ is very important in creating an effective fractal orifice for better thermal mixing.

The definition of thermal mixing performance Θ within a T -duct, is the ratio between the dimensionless area-averaged temperature over temperature difference within the same cross-section. Thus, the smaller the temperature difference reflects larger Θ . the thermal mixing performance of the present orifices along the mixing chamber at $Re_H = 1.94 \times 10^4$ is shown in *Figure 55*. It is observed that Θ increases downstream of the channel for all cases and the Θ for CO, SO, SFO, and KSFO are higher when they are compared to smooth channel. Hence, the inserts evaluated in this study are able to provide reasonably good thermal mixing performance. More importantly, thermal mixing performance can be listed in decreasing order as KSFO, CO, SO, and SFO respectively. Seemingly important to note that the most basis pattern of KSFO at $N = 1$ is well organised at the centre part of insert, comparatively to SFO fractal arrangement, which is widely outspreading and approaching closer to the channel wall. The D_{eq} for SFO is 24.1%, 121.0%, and 149.3% higher compared with KSFO, SO, and CO respectively. Therefore, it seems that the smaller duplication of the complex perimeter is hindering the development of larger flow recirculation leeward from the plate. Even though by having a slightly lower D_{eq} , KSFO complex smaller duplication allows higher hydrodynamics disturbance together with the larger generated wakes around the plate. Consequently, KSFO outperforms the rest in thermal mixing enhancement.

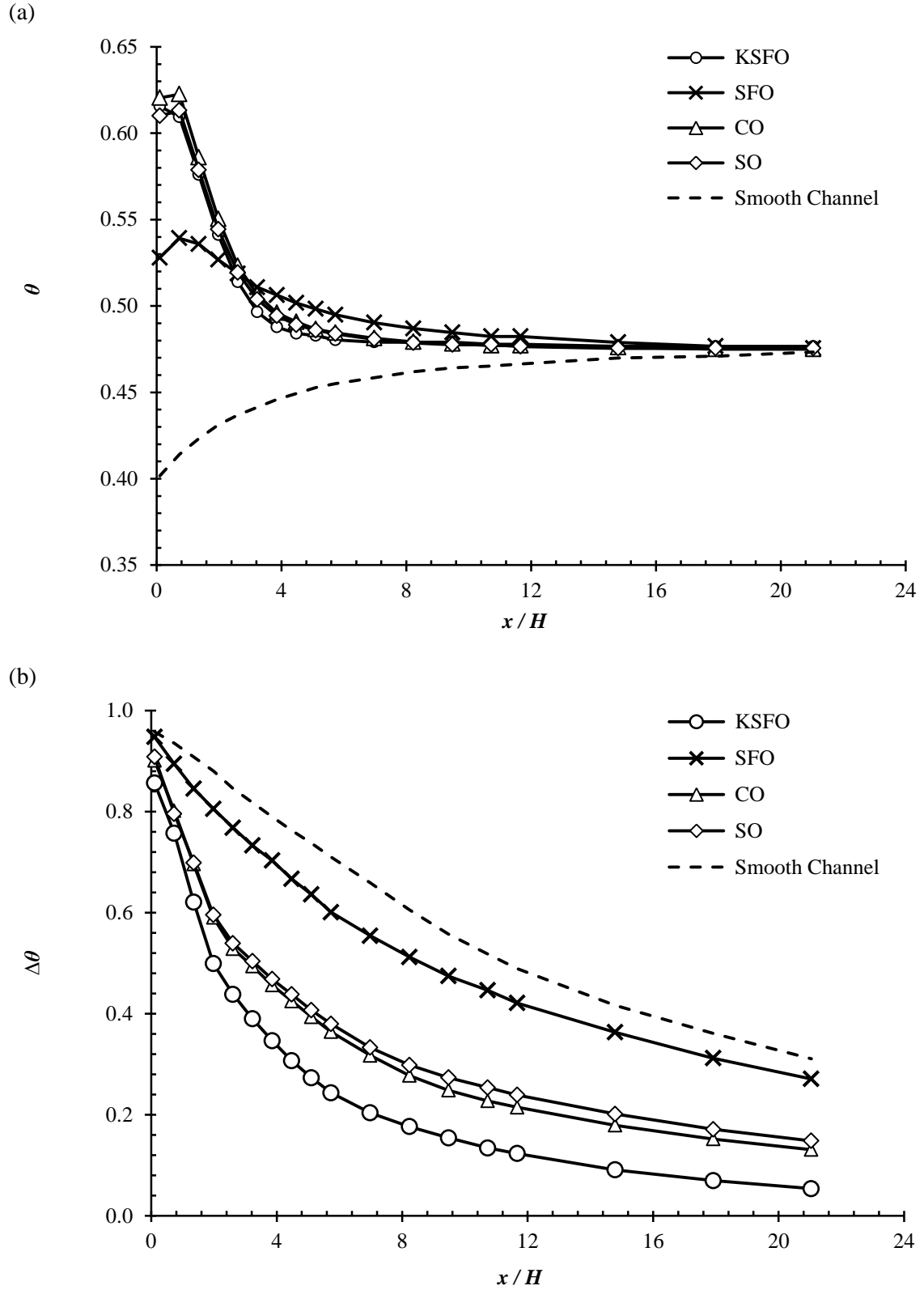


Figure 54. Dimensionless (a) average temperature θ and (b) temperature variation $\Delta\theta$ for the different inserts and smooth channel

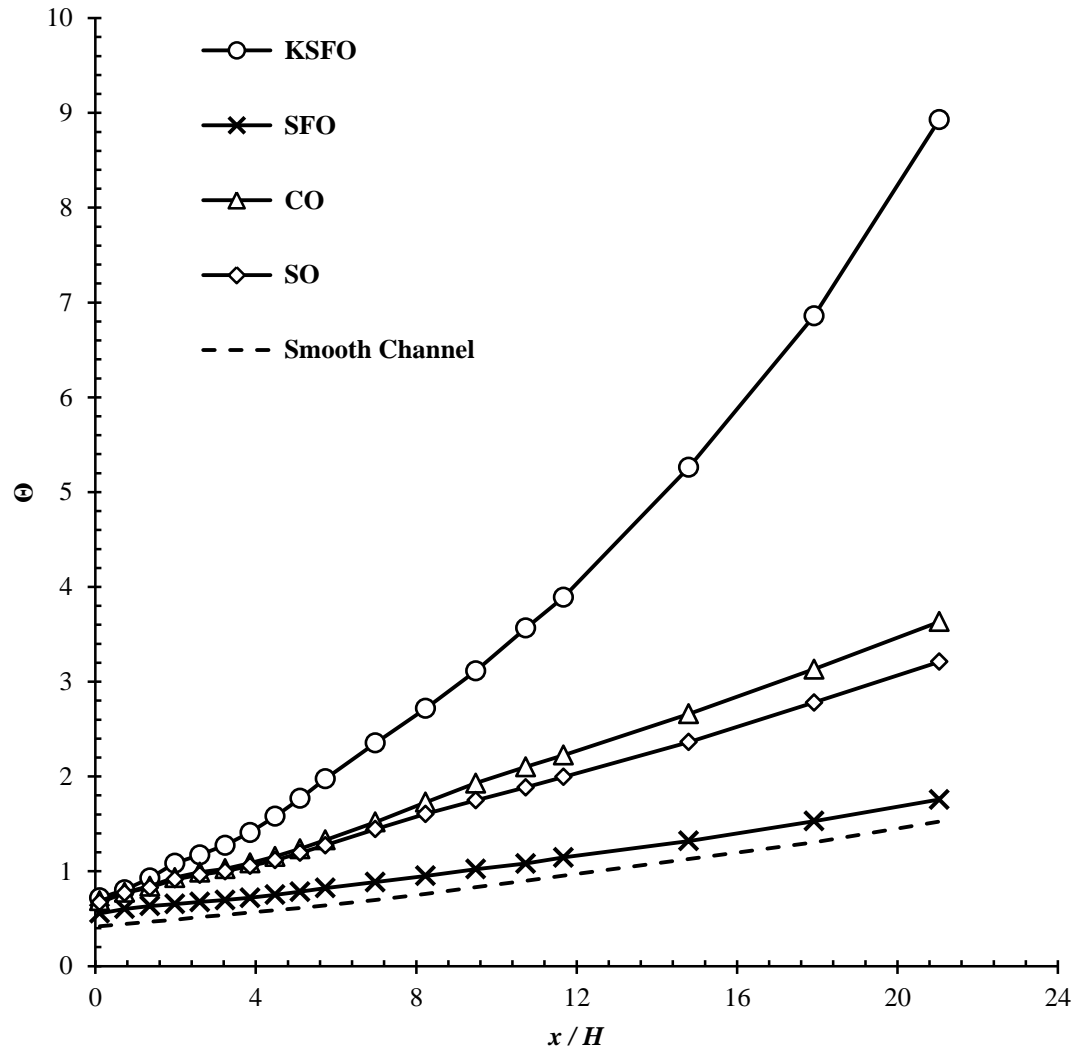


Figure 55. Thermal mixing performance Θ for CO, SO, SFO, and KSFO insert in a Tee joint test section

Influence of turbulence kinetic energy using different orifice inserts

Standard k - ε turbulence model couple with energy equations are used to predict the thermal mixing effect of orifice inserts. Therefore, the energy within the turbulence, i.e. the turbulence kinetic energy k can be directly identified associate with the effectiveness of thermal mixing. Alternatively, k can also be experimentally evaluated using *Eqn. 13* using the transient velocity fluctuations in each component, that is the larger the flow fluctuation the higher the k .

$$k = \frac{1}{2} [\langle (u')^2 \rangle + \langle (v')^2 \rangle + \langle (w')^2 \rangle] \quad \text{Eqn. 13}$$

The effects of orifice geometry on the numerically predicted cross-sectional area-averaged k_{ave} over normalised positions downstream of the inserts, as well as the numerically calculated k_{ave} for the empty channel are compared and portrayed in *Figure 56(a)*. Results show that empty channel has a marginally higher k_{ave} at $x/H = 0$, which is solely due to the T -duct induced flow mixing of the two air streams upstream of the mixing chamber. Meanwhile, for CO, SO, SFO, and KSFO the k_{ave} are much higher to that of the empty channel. The k_{ave} for SO, CO, and KSFO generally increase from $x/H = 0$ to a peak at about $x/H = 0.61$, 0.67 , and 1.36 respectively, then decrease from there onward downstream of the peak locations. However, such distinctive feature are not present in the case of SFO, where k_{ave} reduces immediately and quickly after the insert until $x/H = 1.36$, and beyond $x/H = 1.36$, k_{ave} decreases slowly. Among all the orifices, KSFO has the highest k_{ave} at $x/H = 1.04$, which is 37%, 48%, 371%, and 1454% higher when compared to CO, SO, SFO, as well as empty channel respectively,.

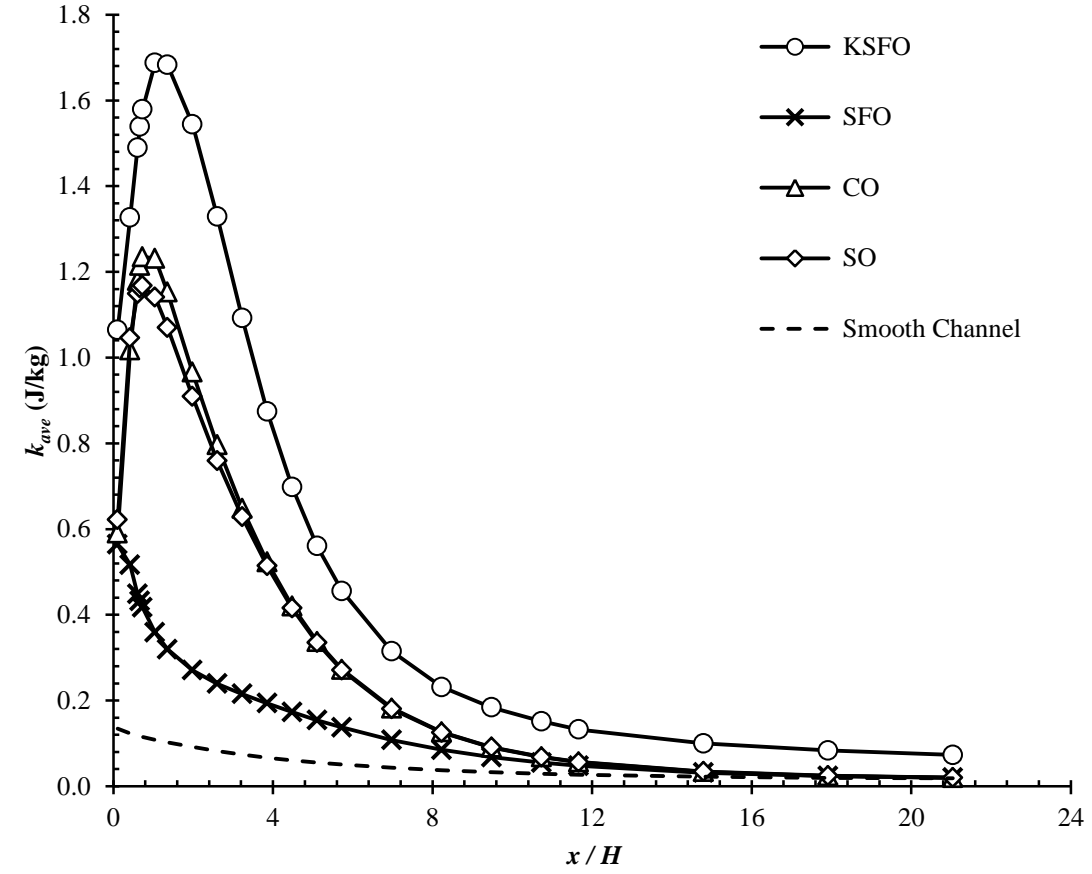
Following on, the centreline turbulence kinetic energy k which is generated by the orifices in the present study are compared with orifice patterns proposed earlier by [Nicolleau et al. \(2011\)](#). [Beforehand](#), numerically validation have been done on the calculated results and portrayed in *Figure 50*. As depicted in *Figure 56(b)* and (c), the observations are made between the dimensionless centreline $k/k_{CO,max}$ from the literature, and centreline $k/k_{KSFO,max}$ for the current orifices, downstream of the circular channel and square T -duct of each cases respectively. Results in *Figure 56(b)* suggest that the circular orifice CO outperforms other orifices, i.e. the $N = 1, 2$, and 3 triangular fractal orifices. On the other hand, the centreline k for KSFO is the highest

among the orifices used in the present study, of which CO is included. Hence, these observations may confirm the thoughts that it is crucial in the selection of a preferred base fractal geometry at $N = 1$, and its capability in keeping the larger flow recirculation downstream of the insert, whilst incorporating higher fractal iterations to strengthen the thermal mixing performance.

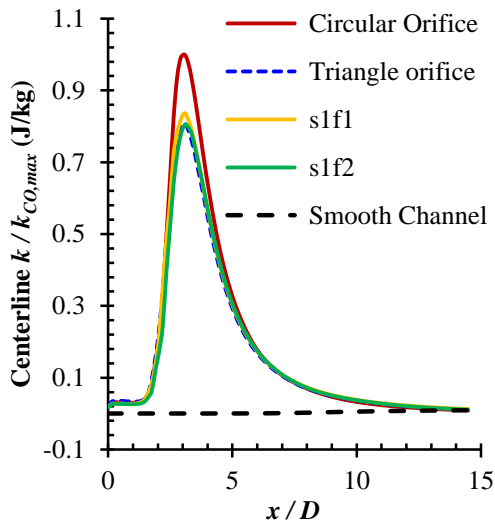
Figure 57 depicts the histograms of the cross-sectional k over continuous developments leeward of KSFO (red), SFO (blue), CO (green), and SO (brown) at $x/H = 0.106, 0.731$, and 3.856 as well as histogram for empty smooth channel (purple) is available for comparison. Results show that KSFO possesses the highest and largest range of k , which is followed by SO, CO, SFO, and the empty channel respectively. Such superb turbulence generation capability displayed by KSFO might be due to its longer equivalent diameter D_{eq} , which enables smaller self-similar scales to build up. It is also important to note that the fractal geometry of KSFO is allocated toward the central region of the insert, which allows the upstream flow to be disturbed at the higher flow velocity regime towards the middle of the channel cross-section. Therefore, this could explain why KSFO is more effective than SFO. Furthermore, the histogram provided by each orifice can be considered unique in terms of hydrodynamic characteristics for each particular inserts in the production of turbulence. As shown in *Figure 57(g-l)*, histogram patterns at $x/H = 0.106, 0.731$, and 3.856 suggest for CO and SO are almost the same, but the former possesses higher k at $x/H = 0.106$ and 0.731 , but slightly lower maximum span value at $x/H = 3.856$, i.e. 1.04J/kg for CO versus 1.08J/kg for SO.

The area-averaged turbulence kinetic energy k_{ave} as well as the orifice induced k scaling in terms of size and range across the downstream channel cross-sections, have been discussed in *Figure 56* and *Figure 57*. The 2D contours plot of and the orifices generated mid-plane flow recirculation and their correlated turbulence kinetic energy distributions are shown in *Figure 58*. Visibly, due to the disturbance at the T -junction upstream of the channel, air flow recirculation is non-symmetric in nature. It is important to note that that higher k possesses stronger correlation with inducing recirculating flow. Therefore, as portrayed in *Figure 58(a)* and (e), both the turbulence kinetic energy and domain covered by the recirculating flow are greatly strengthened by KSFO, which in turn leading to the highest, widest and furthest coverage in k downstream of

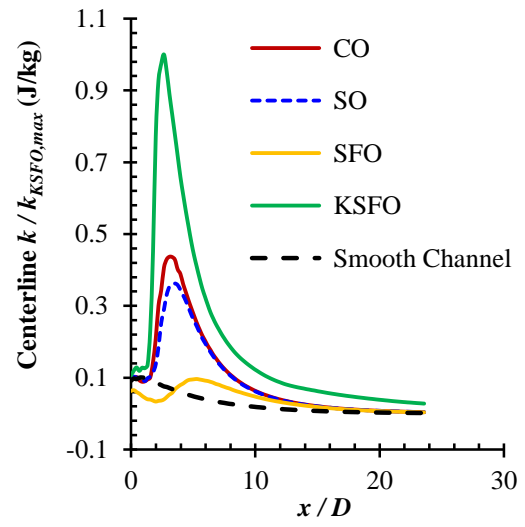
the channel, when compared to other cases, as shown in *Figure 58(b-d)* and (f-h). Hence, thermal mixing can be effectively enhanced with KSFO, followed by CO, then SO. The thermal mixing performance of SFO is noticeably the weakest among the four orifices.



(a)



(b)



(c)

Figure 56. Cross-sectional averaged turbulence kinetic energy among different inserts

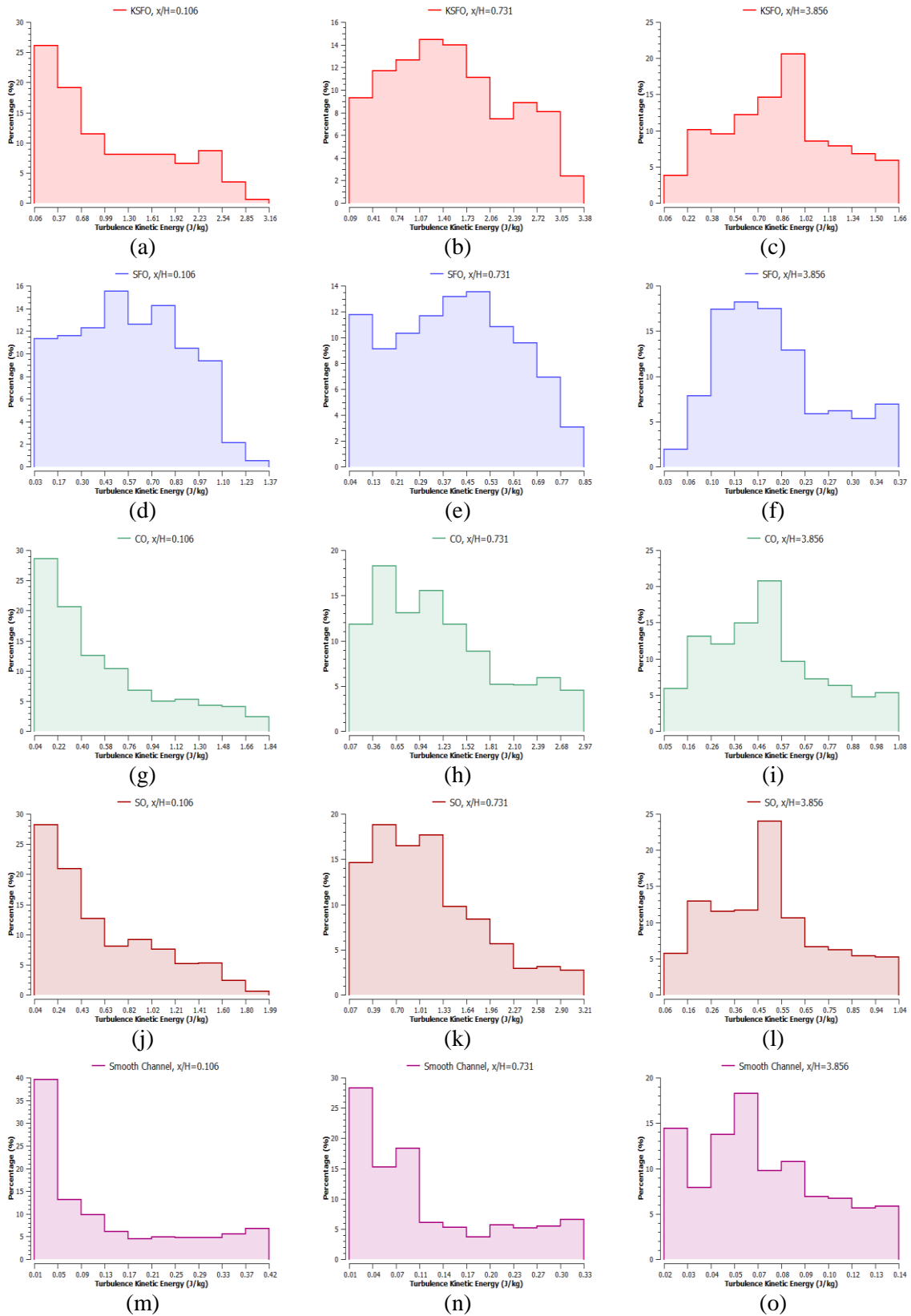


Figure 57. Histogram for cross-sectional turbulence kinetic energy downstream of the insert at $x/H = 0.106, 0.731$, and 3.856 for KSFO (a-c), SFO (d-f), CO (g-i), SO (j-l), and smooth channel (m-o)

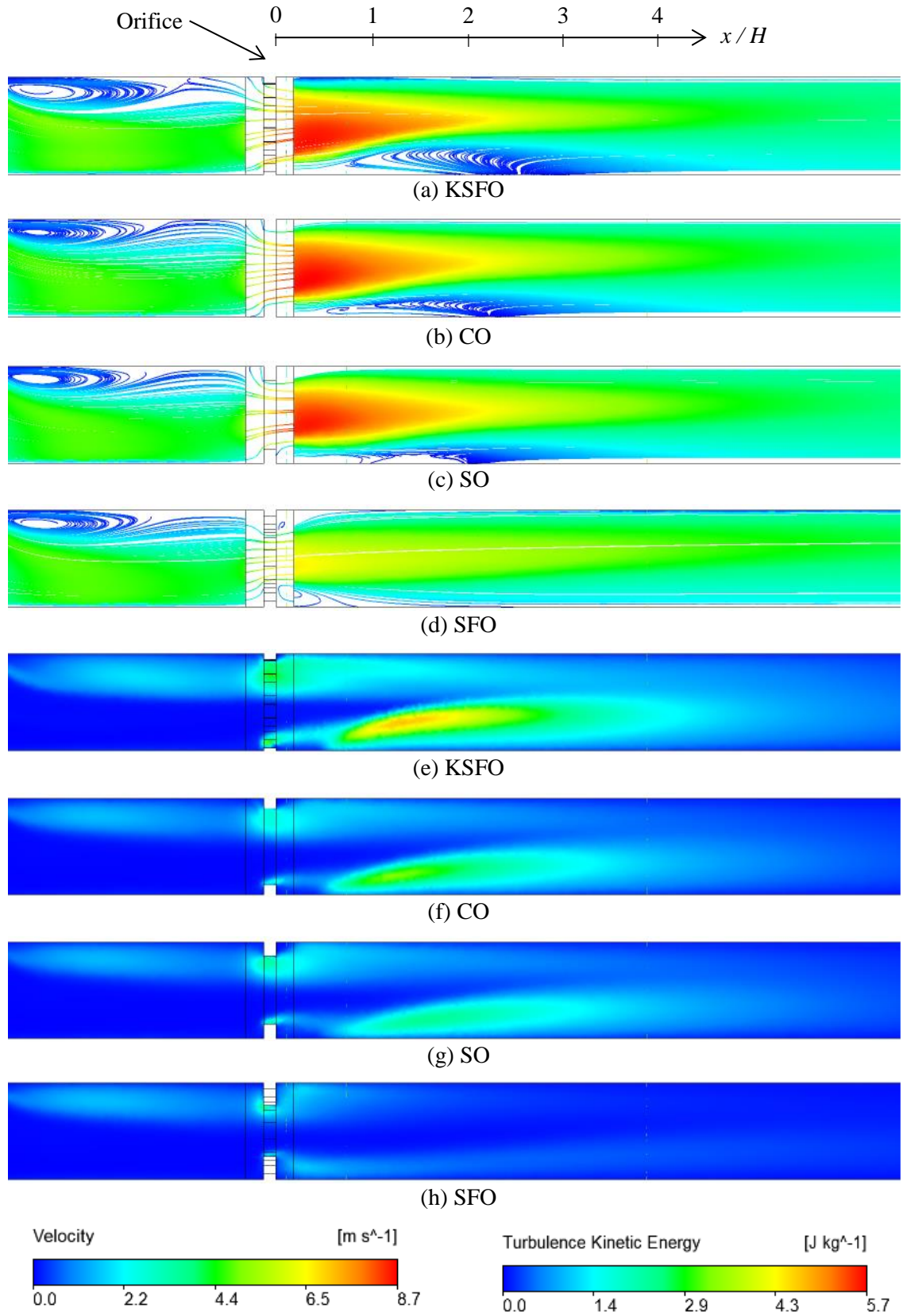


Figure 58. Cross-sectional $z/H = 0.5$ velocity streamline (top four illustrations) and turbulence kinetic energy (bottom four illustrations) for the various inserts

Vertical velocity profiles downstream of the inserts

The temperature and fluid flow distributions of two inlets joint by a Tee typically found within a HVAC free-cooling system are mostly non-uniform, which may lead to unnecessary degradation in performance of air heat exchanger in HVAC system (Mishra et al., 2008). The normalised vertical velocity and temperature distributions leeward from each orifice at various sliced locations namely, from $z/H = 0.5, 0.25$, to 0.125 , are shown in *Figure 59* and *Figure 60*. As portrayed in *Figure 59(a-c)*, the flows started out as non-symmetric at $x/H = 0.106$, but fully developed profiles can be obtained when it reaches far downstream at $x/H = 23.54$ for all cases. It is interesting to note that only SO and CO flow velocity profiles appear to be symmetric at this downstream location, whereas KSFO is unable to attain fully symmetric, of which it may be due to its basic geometry being non-symmetrical in nature, i.e. an equilateral triangle. It is found that the maximum deviation at the position closer to the centre of the channel is about 9.3% compared with SO, and the deviation is less than 3% SO, CO, SFO as well as the empty channel. Moreover, the smaller scale duplication by fractal geometry is able to perturb the working fluid which causes significant flutter in the flow velocity profile. Such an effect can be seen in SFO at $x/H = 0.106$ and $z/H = 0.5$ [see *Figure 59(a)*], and it appears to be more influential while approaching towards the wall of the channel at $z/H = 0.125$ [see *Figure 59(c)*] for both KSFO and SFO. With regards to temperature uniformity, it is clear in *Figure 60(a-c)* that KSFO is able to attain outstanding temperature uniformity leeward of the channel at $x/H = 23.54$. All the calculated KSFO dimensionless temperatures T/T_c are almost upright at all $z/H = 0.5, 0.25$, to 0.125 with an overall discrepancy of about 0.3%. This variation is approximately 1.1% for SO and CO, and between 2 to 2.3% for SFO and empty channel without insert respectively. Interesting to note, KSFO could start to outperforms the rest at the early state of thermal mixing as soon as at $x/H = 0.106$, where the variation in T/T_c is the lowest among all the present cases.

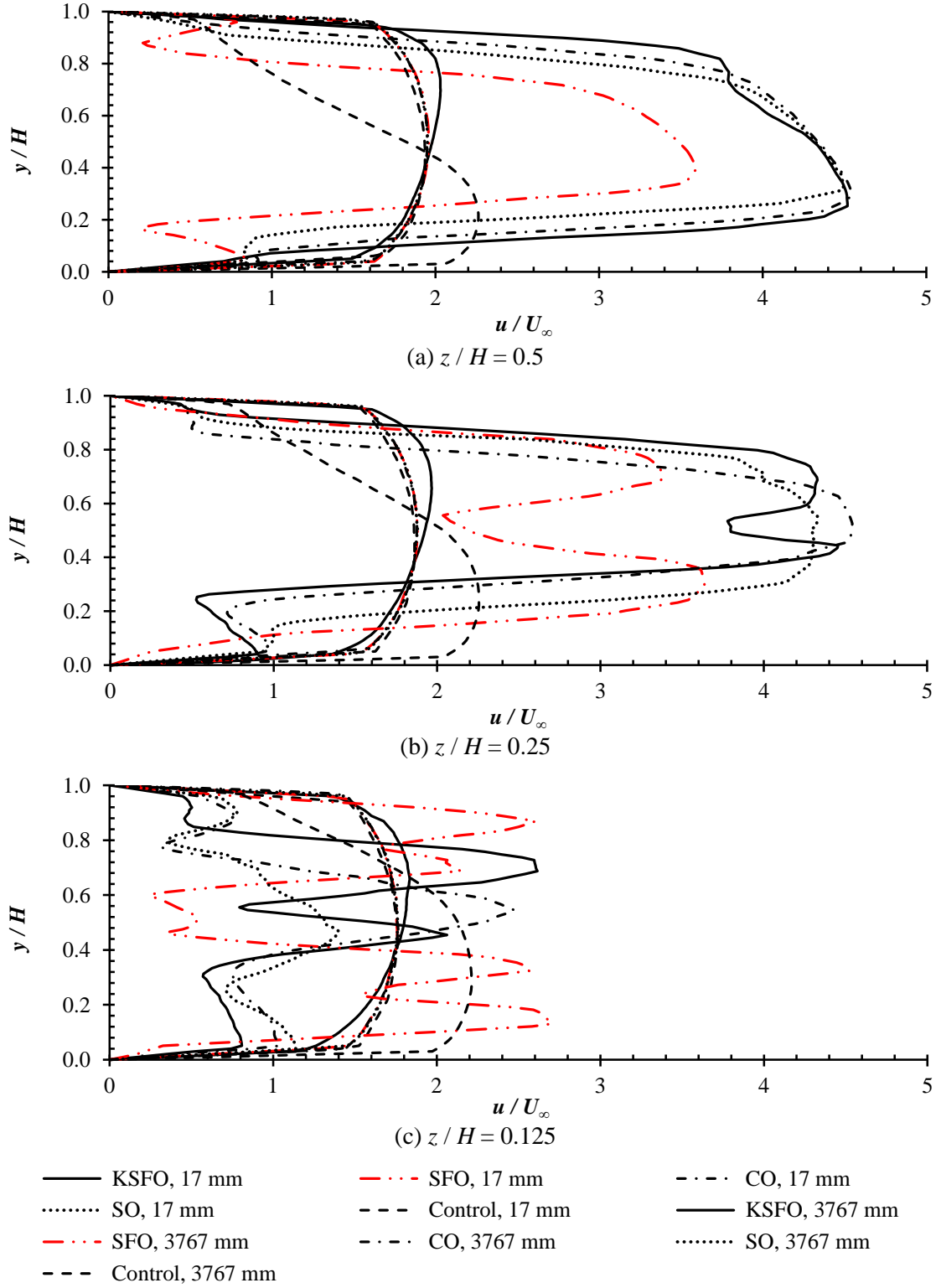


Figure 59. Vertical dimensionless velocity profiles at $x / H = 0.106$ and 23.54 for all inserts and empty channel (control) at different $z / H =$ (a) 0.5 , (b) 0.25 , and (c) 0.125

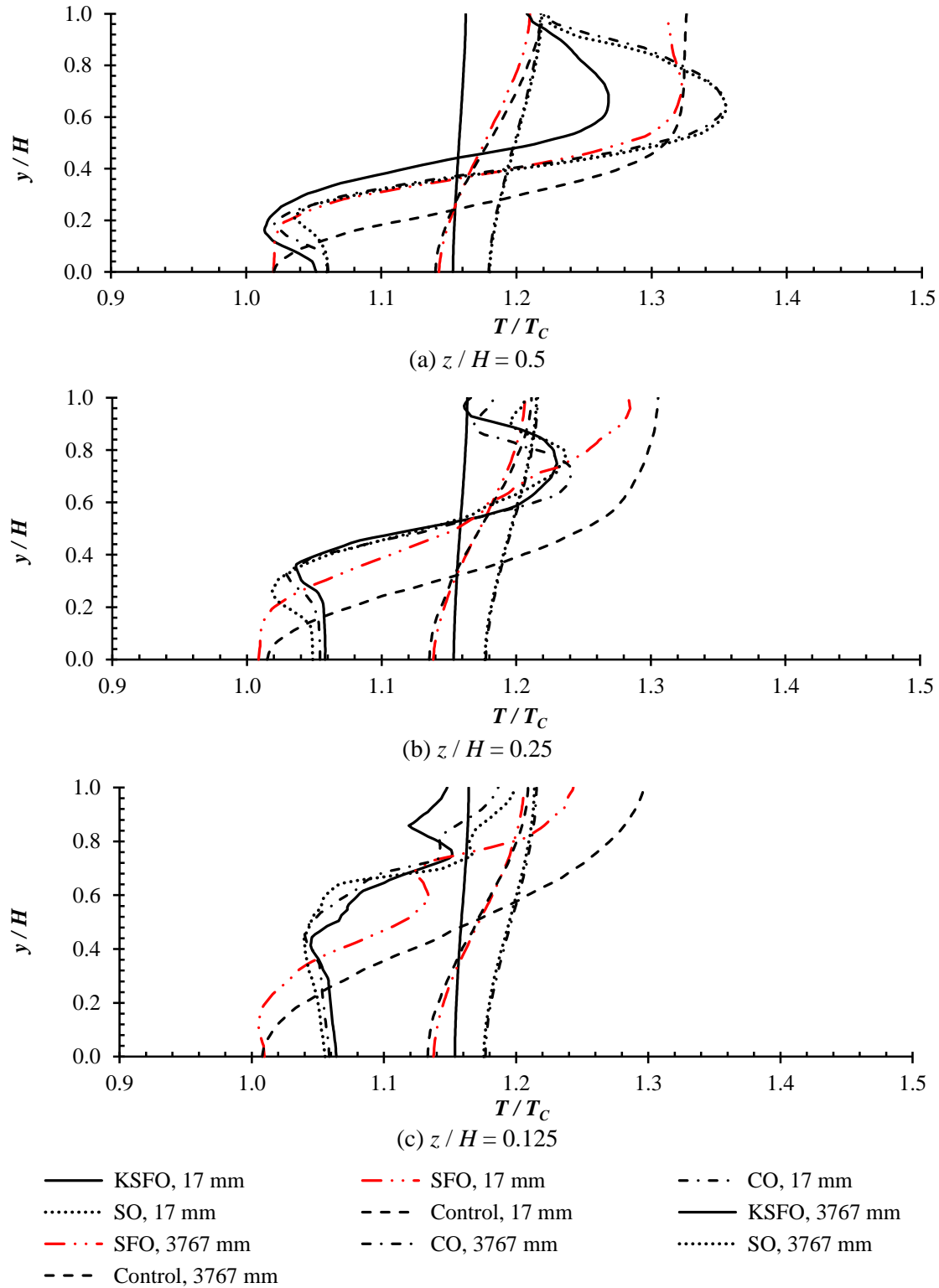


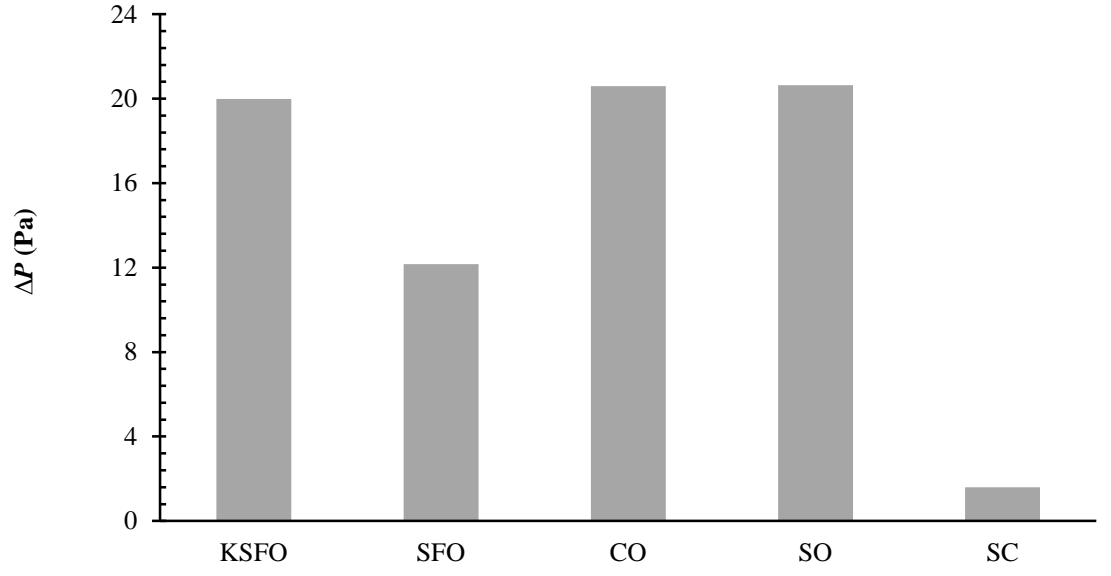
Figure 60. Vertical dimensionless temperature profiles at $x / H = 0.106$ and 23.54 for all inserts and empty channel (control) at different $z / H =$ (a) 0.5, (b) 0.25, and (c) 0.125

Pressure drop and system performance among the various inserts

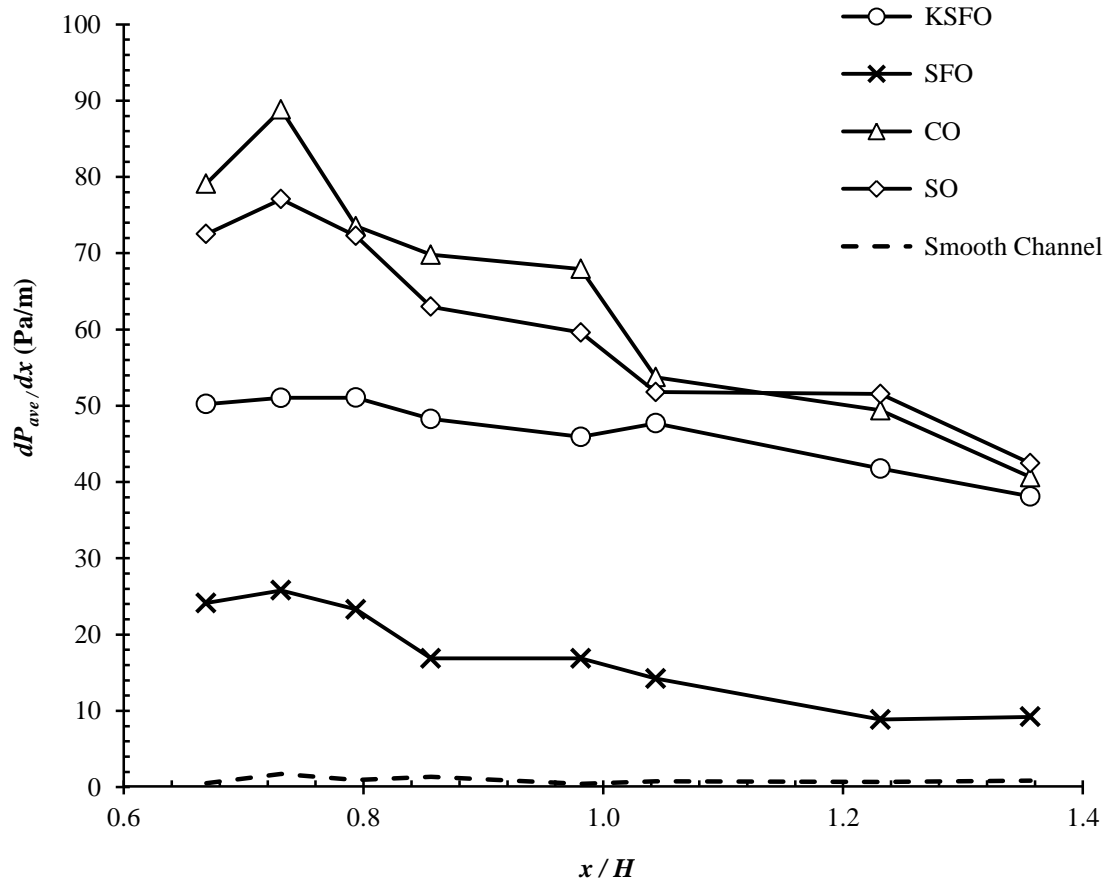
By introducing a disturbance in the fluid flow, the effective thermal mixing can be enhanced,. However, this may also introduce a considerable rise in pressure drop and subsequently increases the cost of pumping power. Therefore, it is important to take pressure drop into account in order to attain desirable thermal mixing performance in HVAC free-cooling system, of which sustainable orifice plate design is favoured. The calculated pressure difference ΔP for each orifice is between $-0.44 \leq x / H \leq 17.92$ and is depicted as *Figure 61(a)*. Clearly, the SO pressure drop is the highest, followed by CO, KSFO, SFO, and the smooth channel in respective order. As shown in *Table 7*, the D_{eq} for KSFO is about 78% and 100.9% larger than SO and CO respectively. This may indicate the fact that the larger equivalent circular orifice diameter assigned to KSFO seems to have an effect on the pressure drop, which is lower than that of the former two orifices, irrespective of the rigorous k generated leeward of the plate. Therefore, some extent of correlation may be brought between D_{eq} and the corresponding pressure coefficient. *Figure 61(b)* portrays the cross-sectional area-averaged pressure gradient dP_{ave} / dx distributions leeward from the inserts. Results show that the rate of change of pressure gradient decreases as a function of the downstream position for all cases. Clearly, the pressure gradient is not only relies on D_{eq} , but also strongly depends on the base geometry and its respective fractal configuration. It seems that the KSFO pressure gradient decreases more gradually when compared to CO and SO, even though the ΔP is lower. Therefore, the corresponding critical physical parameters can be mathematically regulated by carefully implementing the fractal-shaped orifice configuration, in order to provide a better and long term sustainable thermal mixing performance.

The definition for system performance η of the orifice induced thermal mixing can be described as the ratio Θ over pressure coefficient. It terms the relative cost of pressure drop (pumping power) in order to achieve certain rate of thermal mixing. Most importantly, only cases with outstanding Θ are selected and compared. Obviously, KSFO system performance is 1.8× and 1.9× higher than CO and SO respectively, as shown in *Figure 62*. Therefore, it reiterates the

importance in selecting base fractal geometry at $N = 1$ and its subsequent D_{eq} to obtain maximum system performance.



(a)



(b)

Figure 61. (a) Pressure drop and (b) cross-sectional averaged pressure gradients of the various inserts and smooth channel

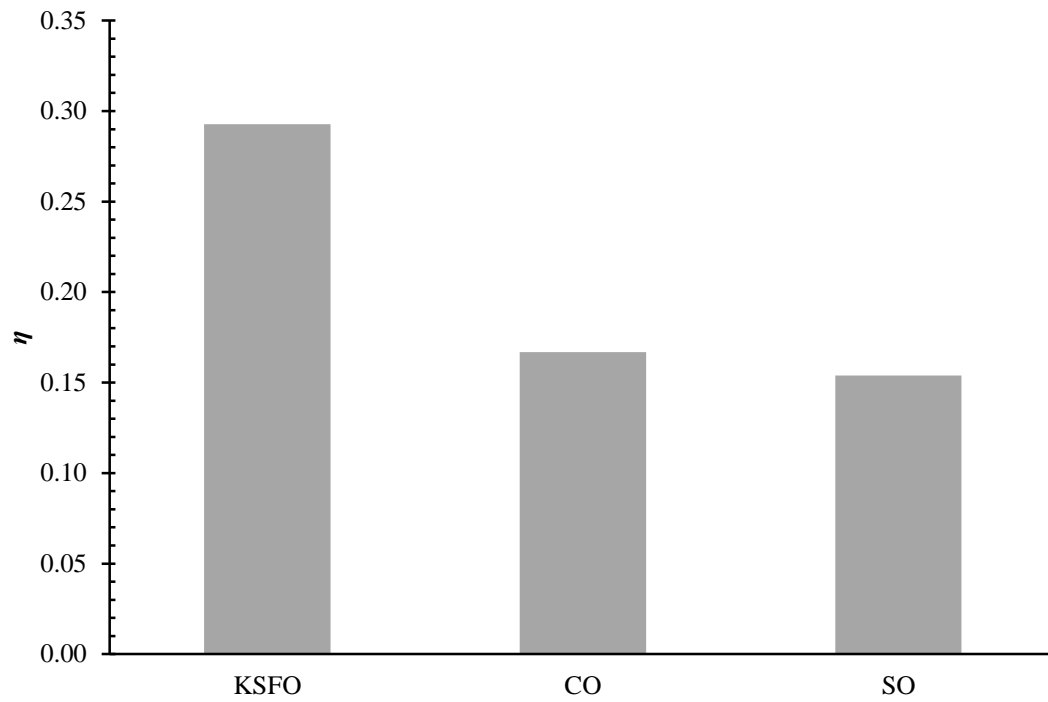


Figure 62. System performance among KSFO, CO, and SO inserts

Chapter summary

3D, steady-state, specific orifices induced turbulence in a T -duct have been investigated numerically to quantify their thermal mixing characteristics. System performances are compared between control and fractal-shaped orifices. The conclusions of this study are:

1. Flow recirculation leeward of the control orifice at $\sigma = 0.5$ and $Re_H = 1.94 \times 10^4$ is one of the main factors in promoting effective thermal mixing. Upon the design of fractal-shaped orifice, it is crucial to retain the existing flow recirculation with an appropriate fractal geometry at $N = 1$, in the meantime, introducing smaller edge self-similarity with complex duplication around the orifice perimeter to provide a greater hydrodynamic fluid flow interaction with the existing one. As a result, a combination of multi-iterations orifice-liked fractal geometry enable effective thermal mixing enhancement downstream of the channel.
2. KSFO creates the highest and widest range of k followed by SO, CO, SFO, and the empty smooth channel. The outstanding capability in producing turbulence with KSFO may due to the longer D_{eq} that constitutes the smaller scale duplication, as well as the orifice allocation which enable higher flow speed slicing. As a result, regardless of KSFO slightly tilted fully developed velocity profiles at $x / H = 23.54$, it is able to achieve prominent temperature uniformity with an overall variation of about 0.3%.
3. ΔP across the orifice plate is smaller with KSFO and SFO due to the higher D_{eq} . The fractal orifice configuration may allow critical physical parameters to be mathematically optimised in providing a better and long term sustainable thermal mixing performance. Maximum system performance may be obtained using fractal-shaped orifice, provided that the D_{eq} and fractal geometry of $N = 1$ have been wisely selected. Among the present proposed cases, KSFO offers the best thermal mixing at a lower pressure drop.

CHAPTER 7 – CONCLUSION AND RECCOMENDATIONS

The present study concludes the main impact observed from the three proposed physical scenarios in employing insert as an effective turbulence generator, in order to have a better understanding in fractal-induced turbulence, and most importantly, the capabilities in thermal mixing enhancement.

1. The capability of an insert in producing larger flow recirculation leeward from the insert is always accompanied with predominant hydrodynamic fluctuation, thus higher turbulence kinetic energy can be seen. One of the critical parameters observed in effective turbulence control is the geometry and area surrounding the orifice insert.
2. Numerical results suggest that good thermal mixing could be associated with evenly distributed and wider range (minimum and maximum) turbulence kinetic energy histogram, which could also indicate the presence of eddies from the smaller localised scale to the larger global scale.
3. Tilting of inserts may achieve larger hydrodynamic recirculation which is beneficial to thermal mixing, provided the blockage ratio is sufficiently large to redirect the flow, i.e. NSFG. However, tilting may cause non-uniform velocity profile even at considerable distance downstream of the insert. Unless the intended application does not require uniform velocity distribution downstream, tilting the insert can be viewed as a viable option for thermal mixing applications. It is found that at $\beta = +45^\circ$ and at $x / H = 4.2$, the thermal mixing performance of CO is about 1382% and 374% higher than PSFG and NSFG respectively.
4. At $\beta = 0^\circ$, orifice-liked inserts such as CO, generally could better enhances thermal mixing, when compared to grid type inserts, i.e. RG, PSFG, and NSFG. Among orifice-liked inserts evaluated in the present studies, KSFO could give the best thermal mixing, when compared to CO, SO, and SFO.

Due to limited time and resources available for the present study, the author proposes recommendations to further expand this study by experimentally study KSFO insert into the free-cooling system in HVAC system or on chemical mixing and reaction enhancement. Moreover,

detailed studies can be made on how the fractal geometry could enhance or diminish the large recirculating wake generated by an orifice insert. Although thermal mixing by grid type inserts could not perform as good as their orifice inserts counterparts, nevertheless grid type inserts could induce a lot of small wakes, which may be important in the mixing process which involves chemical reactions. Last but not least, it is possible to apply the static inserts used in the present studies into active-stirrer mixer.

REFERENCES

- Aly, A. A. E.-A., Chong, A., Nicolleau, F., & Beck, S. (2010). Experimental study of the pressure drop after fractal-shaped orifices in turbulent pipe flows. *Experimental Thermal and Fluid Science*, 34, 104-111. doi:10.1016/j.expthermflusci.2009.09.008
- Antonia, R. A., Lee, S. K., Djenidi, L., Lavoie, P., & Danaila, L. (2013). Invariants for slightly heated decaying grid turbulence. *Journal of Fluid Mechanics*, 727, 379-406. doi:10.1017/jfm.2013.217
- Azad, M., Quinn, W. R., & Groulx, D. (2012). Mixing in turbulent free jets issuing from isosceles triangular orifices with different apex angles. *Experimental Thermal and Fluid Science*, 39, 237-251. doi:10.1016/j.expthermflusci.2012.01.028
- Bury, T. (2012). Impact of a Medium Flow Maldistribution on a Cross-Flow Heat Exchanger Performance. In J. Mitrovic (Ed.), *Heat Exchangers-Basic Design Applications* (pp. 117-142).
- Caffero, G., Discetti, S., & Astarita, T. (2014). Heat transfer enhancement of impinging jets with fractal-generated turbulence. *International Journal of Heat and Mass Transfer*, 75, 173-183. doi:10.1016/j.ijheatmasstransfer.2014.03.049
- Calay, R. K., & Wang, W. C. (2013). A hybrid energy efficient building ventilation system. *Applied Thermal Engineering*, 57(1-2), 7-13. doi:10.1016/j.applthermaleng.2013.03.042
- Chiou, J. P. (1978). Thermal Performance Deterioration in Crossflow Heat Exchanger due to the Flow Nonuniformity. *Journal of Heat Transfer*, 100(4), 580-587. doi:10.1115/1.3450860
- Coleman, G. N., & Sandberg, R. D. (2010). A primer on direct numerical simulation of turbulence-methods, procedures and guidelines.
- Comte-Bellot, G., & Corrsin, S. (1966). Use of a contraction to improve isotropy of grid-generated turbulence. *Journal of Fluid Mechanics*, 25, 657-&. doi:10.1017/s0022112066000338
- Dimotakis, P. E. (2005). Turbulent mixing *Annual Review of Fluid Mechanics* (Vol. 37, pp. 329-356). Palo Alto: Annual Reviews.
- Eckart, C. (1948). An Analysis of the Strring and Mixing Processes in Incompressible Fluids. *Journal of Marine Research*, 7, 265-275. Retrieved from <Go to ISI>://WOS:A1948XR63800012
- Fossa, M., & Guglielmini, G. (2002). Pressure drop and void fraction profiles during horizontal flow through thin and thick orifices. *Experimental Thermal and Fluid Science*, 26(5), 513-523. Retrieved from <Go to ISI>://WOS:000176945700010

-
- Geipel, P., Goh, K. H. H., & Lindstedt, R. P. (2010). Fractal-Generated Turbulence in Opposed Jet Flows. *Flow, Turbulence and Combustion*, 85(3-4), 397-419. doi:10.1007/s10494-010-9288-x
- Gomes-Fernandes, R., Ganapathisubramani, B., & Vassilicos, J. C. (2012). Particle image velocimetry study of fractal-generated turbulence. *Journal of Fluid Mechanics*, 711, 306-336. doi:10.1017/jfm.2012.394
- Hashiehbaf, A., & Romano, G. P. (2013). Particle image velocimetry investigation on mixing enhancement of non-circular sharp edge nozzles. *International Journal of Heat and Fluid Flow*, 44(0), 208-221. doi:<http://dx.doi.org/10.1016/j.ijheatfluidflow.2013.05.017>
- Hiramatsu, T., Kato, Y., Ushijima, T., & Kitoh, O. (2011). *Development of Flow Behind Three-Dimensional Fractal Structure*. Paper presented at the ASME-JSME-KSME 2011 Joint Fluids Engineering Conference.
- Hurst, D., & Vassilicos, J. C. (2007). Scalings and decay of fractal-generated turbulence. *Physics of Fluids*, 19, 31. doi:10.1063/1.2676448
- Khan, Z., & Joshi, J. B. (2015). Comparison of k-epsilon, RSM and LES models for the prediction of flow pattern in jet loop reactor. *Chemical Engineering Science*, 127, 323-333. doi:10.1016/j.ces.2015.01.054
- Kolmogorov, A. N. (1941). The local structure of turbulence in incompressible viscous fluid for very large reynolds numbers. *Proceedings of the USSR Academy of Sciences*, 30, 301-305.
- Kumar, A. (2015). Mean Flow and Thermal Characteristics of a Turbulent Dual Jet Consisting of a Plane Wall Jet and a Parallel Offset Jet. *Numerical Heat Transfer Part a-Applications*, 67(10), 1075-1096. doi:10.1080/10407782.2014.955348
- Laizet, S., Lamballais, E., & Vassilicos, J. C. (2010). A numerical strategy to combine high-order schemes, complex geometry and parallel computing for high resolution DNS of fractal generated turbulence. *Computers & Fluids*, 39, 471-484. doi:10.1016/j.compfluid.2009.09.018
- Laizet, S., & Vassilicos, J. C. (2009). Multiscale generation of turbulence. *Journal of Multiscale Modelling*, 01(01), 177-196. doi:doi:10.1142/S1756973709000098
- Laizet, S., & Vassilicos, J. C. (2011). DNS of Fractal-Generated Turbulence. *Flow Turbulence and Combustion*, 87, 673-705. doi:10.1007/s10494-011-9351-2
- Laizet, S., & Vassilicos, J. C. (2012). Fractal space-scale unfolding mechanism for energy-efficient turbulent mixing. *Physical Review E*, 86(4), 046302-046302. doi:10.1103/PhysRevE.86.046302

-
- Mandelbrot, B. B. (1983). *The fractal geometry of nature*: Macmillan.
- Mazellier, N., & Vassilicos, J. C. (2010). Turbulence without Richardson-Kolmogorov cascade. *Physics of Fluids*, 22(7), 25. doi:10.1063/1.3453708
- Mazzi, B., Okkels, F., & Vassilicos, J. C. (2002). A shell-model approach to fractal-induced turbulence. *European Physical Journal B*, 28, 243-251. doi:10.1140/epjb/e2002-00226-6
- Meshkov, E. E. (1969). Instability of the interface of two gases accelerated by a shock wave. *Fluid Dynamics*, 4, 101--104.
- Mi, J., Nathan, G. J., & Nobes, D. S. (2001). Mixing characteristics of axisymmetric free jets from a contoured nozzle, an orifice plate and a pipe. *Journal of Fluids Engineering-Transactions of the Asme*, 123(4), 878-883. doi:10.1115/1.1412460
- Mishra, M., Das, P. K., & Sarangi, S. (2008). Effect of temperature and flow nonuniformity on transient behaviour of crossflow heat exchanger. *International Journal of Heat and Mass Transfer*, 51(9-10), 2583-2592. doi:10.1016/j.ijheatmasstransfer.2007.07.054
- Morrison, G. L., Deotte, R. E., Nail, G. H., & Panak, D. L. (1993). Mean velocity and turbulence fields inside a $\beta=0.50$ orifice flowmeter. *AIChE Journal*, 39(5), 745-756. doi:10.1002/aic.690390503
- Murzyn, F., & Belorgey, M. (2005). Experimental investigation of the grid-generated turbulence features in a free surface flow. *Experimental Thermal and Fluid Science*, 29(8), 925-935. doi:10.1016/j.expthermflusci.2005.02.002
- Nagata, K., Sakai, Y., Inaba, T., Suzuki, H., Terashima, O., & Suzuki, H. (2013). Turbulence structure and turbulence kinetic energy transport in multiscale/fractal-generated turbulence. *Physics of Fluids*, 25(6), 26. doi:10.1063/1.4811402
- Nicolleau, F. C. G. A., Salim, S. M. M., & Nowakowski, A. F. (2011). Experimental study of a turbulent pipe flow through a fractal plate. *Journal of Turbulence*, 12, 1-20. doi:10.1080/14685248.2011.637046
- Queiros-Conde, D., & Vassilicos, J. C. (2001). Turbulent wakes of 3D fractal grids. *Intermittency in Turbulent Flows*, 136-167. Retrieved from <Go to ISI>://WOS:000169874300009
- Rackes, A., & Waring, M. S. (2014). Using multiobjective optimizations to discover dynamic building ventilation strategies that can improve indoor air quality and reduce energy use. *Energy and Buildings*, 75, 272-280. doi:10.1016/j.enbuild.2014.02.024

-
- Rayleigh, S. J. W. L. (1883). Investigation of the character of the equilibrium of an incompressible heavy fluid of variable density. *Proceedings of the London mathematical society*, 14, 170--177.
- Reynolds, O. (1883). An experimental investigation of the circumstances which determine whether the motion of water shall be direct or sinuous, and of the law of resistance in parallel channels. *Proceedings of the Royal Society of London*, 35(224-226), 84-99.
- Richtmyer, R. D. (1960). Taylor Instability in Shock Acceleration of Compressible Fluids. *Communications on Pure and Applied Mathematics*, XIII, 297--319.
- Salim, S. M. M., & Nicolleau, F. (2012). Fractality in turbulence. *Journal of Mechanical Science and Technology*, 26(5), 1311-1314. doi:10.1007/s12206-012-0329-3
- Sarkar, A., & Schluter, J. (2014). Large Eddy Simulations of Turbulent Mixing Layers Excited with Two Frequencies. *Flow Turbulence and Combustion*, 92(3), 651-671. doi:10.1007/s10494-013-9507-3
- Seoud, R. E., & Vassilicos, J. C. (2007). Dissipation and decay of fractal-generated turbulence. *Physics of Fluids*, 19(10), 105-108. doi:10.1063/1.2795211
- Shaaban, S. (2014). Optimization of orifice meter's energy consumption. *Chemical Engineering Research & Design*, 92(6), 1005-1015. doi:10.1016/j.cherd.2013.08.022
- Shehabi, A., Ganguly, S., Gundel, L. A., Horvath, A., Kirchstetter, T. W., Lunden, M. M., . . . Nazaroff, W. W. (2009). Can combining economizers with improved filtration save energy and protect equipment in data centers? *Building and Environment*, 45(3), 718-726.
- Siriwardana, J., Jayasekara, S., & Halgamuge, S. K. (2013). Potential of air-side economizers for data center cooling: A case study for key Australian cities. *Applied Energy*, 104, 207-219. doi:10.1016/j.apenergy.2012.10.046
- Souloupoulos, N., Kerl, J., Sponfeldner, T., Beyrau, F., Hardalupas, Y., Taylor, A., & Vassilicos, J. C. (2013). Turbulent premixed flames on fractal-grid-generated turbulence. *Fluid Dynamics Research*, 45(6), 18. doi:10.1088/0169-5983/45/6/061404
- Staicu, A., Mazzi, B., Vassilicos, J. C., & van de Water, W. (2003). Turbulent wakes of fractal objects. *Physical Review E*, 67, 8. doi:10.1103/PhysRevE.67.066306
- Strasing, R., Peinke, J., Seoud, R. E., & Vassilicos, J. C. (2010). Defining a New Class of Turbulent Flows. *Physical Review Letters*, 104(19), 4. doi:10.1103/PhysRevLett.104.194501

-
- Suzuki, H., Nagata, K., Sakai, Y., & Hayase, T. (2010). Direct numerical simulation of turbulent mixing in regular and fractal grid turbulence. *Physica Scripta*, T142. doi:10.1088/0031-8949/2010/t142/014065
- Suzuki, H., Nagata, K., Sakai, Y., Hayase, T., Hasegawa, Y., & Ushijima, T. (2013). Direct numerical simulation of fractal-generated turbulence. *Fluid Dynamics Research*, 45(6), 23. doi:10.1088/0169-5983/45/6/061409
- Suzuki, H., Nagata, K., Sakai, Y., & Ukai, R. (2010). High-Schmidt-number scalar transfer in regular and fractal grid turbulence. *Physica Scripta*, T142, 6. doi:10.1088/0031-8949/2010/t142/014069
- Taylor, G. (1950). The Instability of Liquid Surfaces When Accelerated in a Direction Perpendicular to Their Planes .1. *Proceedings of the Royal Society of London Series a-Mathematical and Physical Sciences*, 201, 192-196. doi:10.1098/rspa.1950.0052
- Valente, P. C., & Vassilicos, J. C. (2011). The decay of turbulence generated by a class of multiscale grids. *Journal of Fluid Mechanics*, 687, 300-340. doi:10.1017/jfm.2011.353
- Zhang, H. N., Shao, S. Q., Xu, H. B., Zou, H. M., & Tian, C. Q. (2014). Free cooling of data centers: A review. *Renewable & Sustainable Energy Reviews*, 35, 171-182. doi:10.1016/j.rser.2014.04.017
- Zhang, L. Z. (2009). Flow maldistribution and thermal performance deterioration in a cross-flow air to air heat exchanger with plate-fin cores. *International Journal of Heat and Mass Transfer*, 52(19-20), 4500-4509. doi:10.1016/j.ijheatmasstransfer.2009.03.049
- Zheng, H. W., Nicolleau, F. C. G. A., & Qin, N. (2012). Detached Eddy Simulation for Turbulent Flows in a Pipe with a Snowflake Fractal Orifice. In F. C. G. A. Nicolleau, C. Cambon, J. M. Redondo, J. C. Vassilicos, M. Reeks, & A. F. Nowakowski (Eds.), (Vol. 18, pp. 9-21): Springer Netherlands.

Appendix A

Turbulence Theory

As extracted from ANSYS FLUENT Theory Guide.

Navier-Stokes Equation

Conservation of mass in general form can be expressed as:

$$\frac{\partial \rho}{\partial t} + \nabla \cdot (\rho \vec{v}) = 0 \quad \text{Eqn. 14}$$

Conservation of momentum in general form can be expressed as:

$$\rho \frac{D\vec{u}_i}{Dt} = -\nabla p + \nabla \cdot \mathbf{T} + \vec{f} \quad \text{Eqn. 15}$$

Reynolds-averaged Navier-Stokes Equations

From the instantaneous Navier-Stokes equation, RANS equations can be expressed as:

$$\frac{\partial \rho}{\partial t} + \frac{\partial}{\partial x_i} (\rho u_i) = 0 \quad \text{Eqn. 16}$$

$$\begin{aligned} \frac{\partial}{\partial t} (\rho u_i) + \frac{\partial}{\partial x_j} (\rho u_i u_j) \\ = -\frac{\partial p}{\partial x_i} + \frac{\partial}{\partial x_j} \left[\mu \left(\frac{\partial u_i}{\partial x_j} + \frac{\partial u_j}{\partial x_i} - \frac{2}{3} \delta_{ij} \frac{\partial u_l}{\partial x_l} \right) \right] + \frac{\partial}{\partial x_j} (-\rho \overline{u'_i u'_j}) \end{aligned} \quad \text{Eqn. 17}$$

Turbulence models are used to predict the Reynolds stresses, $-\rho \overline{u'_i u'_j}$.

k - ε Turbulence Model

In standard k - ε turbulence model, transport equations for the turbulence kinetic energy k and turbulence kinetic energy dissipation rate ε can be expressed as:

$$\frac{\partial}{\partial t} (\rho k) + \frac{\partial}{\partial x_i} (\rho k u_i) = \frac{\partial}{\partial x_j} \left[\left(\mu + \frac{\mu_t}{\sigma_k} \right) \frac{\partial k}{\partial x_j} \right] + G_k + G_b + \rho \varepsilon - Y_M + S_k \quad \text{Eqn. 18}$$

$$\frac{\partial}{\partial t} (\rho \varepsilon) + \frac{\partial}{\partial x_j} (\rho \varepsilon u_j) = \frac{\partial}{\partial x_j} \left[\left(\mu + \frac{\mu_t}{\sigma_\varepsilon} \right) \frac{\partial \varepsilon}{\partial x_j} \right] + C_{1\varepsilon} \frac{\varepsilon}{k} (G_k + C_{3\varepsilon} G_b) - C_{2\varepsilon} \rho \frac{\varepsilon^2}{k} + S_\varepsilon \quad \text{Eqn. 19}$$

The turbulence viscosity μ_t can be expressed as:

$$\mu_t = \rho C_\mu \frac{k^2}{\varepsilon} \quad \text{Eqn. 20}$$

The model constants usually have the value of $C_{1\varepsilon} = 1.44$, $C_{2\varepsilon} = 1.92$, $C_\mu = 0.09$, $\sigma_k = 1.0$, and $\sigma_\varepsilon = 1.3$.

In realisable k - ε turbulence model, transport equations for the turbulence kinetic energy k turbulence kinetic energy dissipation rate ε can be expressed as:

$$\frac{\partial}{\partial t}(\rho k) + \frac{\partial}{\partial x_j}(\rho k u_j) = \frac{\partial}{\partial x_j} \left[\left(\mu + \frac{\mu_t}{\sigma_k} \right) \frac{\partial k}{\partial x_j} \right] + G_k + G_b + \rho \varepsilon - Y_M + S_k \quad \text{Eqn. 21}$$

$$\begin{aligned} \frac{\partial}{\partial t}(\rho \varepsilon) + \frac{\partial}{\partial x_j}(\rho \varepsilon u_j) \\ = \frac{\partial}{\partial x_j} \left[\left(\mu + \frac{\mu_t}{\sigma_\varepsilon} \right) \frac{\partial \varepsilon}{\partial x_j} \right] + \rho C_{1\varepsilon} S_\varepsilon - \rho C_{2\varepsilon} \frac{\varepsilon^2}{k + \sqrt{\nu \varepsilon}} + C_{1\varepsilon} \frac{\varepsilon}{k} C_{3\varepsilon} G_b + S_\varepsilon \end{aligned} \quad \text{Eqn. 22}$$

where

$$C_1 = \max \left[0.43, \frac{\eta}{\eta + 5} \right] \quad \eta = S \frac{k}{\varepsilon}, S = \sqrt{2 S_{ij} S_{ij}} \quad \text{Eqn. 23}$$

$$\eta = S \frac{k}{\varepsilon}, S = \sqrt{2 S_{ij} S_{ij}} \quad \text{Eqn. 24}$$

$$S = \sqrt{2 S_{ij} S_{ij}} \quad \text{Eqn. 25}$$

Turbulence viscosity μ_t can be expressed as the same as Eqn. 20.

In the case of realisable k - ε , C_μ can be expressed as:

$$C_\mu = \frac{1}{A_0 + A_S \frac{k U^*}{\varepsilon}} \quad \text{Eqn. 26}$$

where

$$U^* \equiv \sqrt{(S_{ij} S_{ij} + \tilde{\Omega}_{ij} \tilde{\Omega}_{ij})} \quad \text{Eqn. 27}$$

and

$$\tilde{\Omega}_{ij} = \Omega_{ij} - 2 \varepsilon_{ijk} \omega_k$$

$$\Omega_{ij} = \overline{\Omega_{ij}} - \varepsilon_{ijk} \omega_k$$

$$A_0 = 4.04$$

$$A_S = \sqrt{6} \cos \phi \quad \text{Eqn. 28}$$

where

$$\phi = \frac{1}{3} \cos^{-1}(\sqrt{6}W) \quad \text{Eqn. 29}$$

$$W = \frac{S_{ij}S_{jk}S_{ki}}{\tilde{S}^3} \quad \text{Eqn. 30}$$

$$\tilde{S} = \sqrt{S_{ij}S_{ij}} \quad \text{Eqn. 31}$$

$$S_{ij} = \frac{1}{2} \left(\frac{\partial u_j}{\partial x_i} + \frac{\partial u_i}{\partial x_j} \right) \quad \text{Eqn. 32}$$

The model constants usually have the value of $C_{1\varepsilon} = 1.44$, $C_2 = 1.9$, $\sigma_k = 1.0$, and $\sigma_\varepsilon = 1.2$.

In both standard and realisable k - ε , the production of turbulence kinetic energy can be expressed as:

$$G_k = -\rho \overline{u'_i u'_j} \frac{\partial u_j}{\partial x_i} \quad \text{Eqn. 33}$$

$$G_k = \mu_t S^2 \quad \text{Eqn. 34}$$

where

$$S \equiv \sqrt{2S_{ij}S_{ij}} \quad \text{Eqn. 35}$$

Hence, after known μ_t , k and ε , Reynolds stresses $-\rho \overline{u'_i u'_j}$, can be calculated using Boussinesq hypothesis:

$$-\rho \overline{u'_i u'_j} = \mu_t \left(\frac{\partial u_i}{\partial x_j} + \frac{\partial u_j}{\partial x_i} \right) - \frac{2}{3} \left(\rho k + \mu_t \frac{\partial u_k}{\partial x_k} \right) \delta_{ij} \quad \text{Eqn. 36}$$

Buoyancy could cause turbulence in a flow, the effect of turbulence is expressed as:

$$G_b = \beta_T g_i \frac{\mu_t}{Pr_t} \frac{\partial T}{\partial x_i} \quad \text{Eqn. 37}$$

In standard and realisable k - ε models, $Pr_t = 0.85$

$$\beta_T = -\frac{1}{\rho} \left(\frac{\partial \rho}{\partial T} \right)_p \quad \text{Eqn. 38}$$

In ideal gases, G_b can be expressed as:

$$G_b = -g_i \frac{\mu_t}{\rho Pr_t} \frac{\partial \rho}{\partial x_i} \quad \text{Eqn. 39}$$

$$C_{3\varepsilon} = \tanh \left| \frac{v}{u} \right| \quad \text{Eqn. 40}$$

The effect of compressibility on turbulence in k - ε can be expressed as:

$$Y_M = 2\rho\varepsilon M_t^2 \quad \text{Eqn. 41}$$

$$M_t = \sqrt{\frac{k}{a^2}} \quad \text{Eqn. 42}$$

$$a \equiv \sqrt{\gamma RT} \text{ (Speed of sound)} \quad \text{Eqn. 43}$$

The convective heat and mass transfer equations used in k - ε models can be expressed as:

$$\frac{\partial}{\partial t}(\rho E) + \frac{\partial}{\partial x_i} [u_i(\rho E + p)] = \frac{\partial}{\partial x_j} \left(k_{eff} \frac{\partial T}{\partial x_j} + u_i(\tau_{ij})_{eff} \right) + S_h \quad \text{Eqn. 44}$$

$$u_i(\tau_{ij})_{eff} = \mu_{eff} \left(\frac{\partial u_j}{\partial x_i} + \frac{\partial u_i}{\partial x_j} \right) - \frac{2}{3} \mu_{eff} \frac{\partial u_k}{\partial x_k} \delta_{ij}$$

$$k_{eff} = k + \frac{c_p \mu_t}{Pr_t}$$

Note the k is thermal conductivity in this case. $Sc_t = 0.7$

Reynolds Stress Model (RSM)

The transport equations for Reynolds stresses $\overline{\rho u'_i u'_j}$ can be expressed as:

Local Time Derivative + C_{ij} (Convection) =
 $D_{T,ij}$ (Turbulent Diffusion)
 $+D_{L,ij}$ (Molecular Diffusion)
 $+G_{ij}$ (Buoyancy Production)
 $+ \phi_{ij}$ (Pressure Strain)
 $-\varepsilon_{ij}$ (Dissipation)
 $+F_{ij}$ (Production by System Rotation)
 $+S_{user}$ (User-Defined Source Term)

of which

$$\begin{aligned}
& \frac{\partial}{\partial t} (\rho \overline{u'_i u'_j}) + \frac{\partial}{\partial x_k} (\rho u_k \overline{u'_i u'_j}) = \\
& - \frac{\partial}{\partial x_k} [\rho \overline{u'_i u'_j u'_k} + (\overline{p'} (\delta_{kj} u'_i + \delta_{ik} u'_j))] \\
& + \frac{\partial}{\partial x_k} \left[\mu \frac{\partial}{\partial x_k} (\overline{u'_i u'_j}) \right] \\
& - \rho \left(\overline{u'_i u'_k} \frac{\partial u_j}{\partial x_k} + \overline{u'_j u'_k} \frac{\partial u_i}{\partial x_k} \right) \\
& - \rho \beta (g_i \overline{u'_j \theta} + g_j \overline{u'_i \theta}) \\
& + p' \left(\frac{\partial u'_i}{\partial x_j} + \frac{\partial u'_j}{\partial x_i} \right) \\
& - 2\mu \frac{\partial u'_i}{\partial x_k} \frac{\partial u'_i}{\partial x_k} \\
& - 2\rho \Omega_k (\overline{u'_j u'_m} \varepsilon_{ikm} + \overline{u'_i u'_m} \varepsilon_{jkm}) \\
& + S_{user}
\end{aligned} \tag{Eqn. 45}$$

Turbulence diffusive equation can be expressed as:

$$D_{T,ij} = \frac{\partial}{\partial x_k} \left(\frac{\mu_t}{\sigma_k} \frac{\partial \overline{u'_i u'_j}}{\partial x_k} \right) \tag{Eqn. 46}$$

where $\sigma_k = 0.82$

Pressure-strain term is modelled using linear pressure-strain model, which can be expressed as:

$$\phi_{ij} = \phi_{ij,1} + \phi_{ij,2} + \phi_{ij,w} \tag{Eqn. 47}$$

where

$$\phi_{ij,1} \equiv -C_1 \rho \frac{\varepsilon}{k} \left[\overline{u'_i u'_j} - \frac{2}{3} \delta_{ij} k \right] \tag{Eqn. 48}$$

where $C_1 = 1.8$

$$\phi_{ij,2} \equiv -C_2 \left[\left(P_{ij} + F_{ij} + \frac{5}{6} G_{ij} - C_{ij} \right) - \frac{2}{3} \delta_{ij} \left(P + \frac{5}{6} G - C \right) \right] \quad \text{Eqn. 49}$$

which $C_2 = 0.6$

$$P = \frac{1}{2} P_{kk}$$

$$G = \frac{1}{2} G_{kk}$$

$$C = \frac{1}{2} C_{kk}$$

$$\begin{aligned} \phi_{ij,w} \equiv C'_1 \frac{\varepsilon}{k} \left(\overline{u'_k u'_m} n_k n_m \delta_{ij} - \frac{3}{2} \overline{u'_i u'_k} n_j n_k - \frac{3}{2} \overline{u'_j u'_k} n_i n_k \right) \frac{C_\ell k^{\frac{3}{2}}}{\varepsilon d} \\ + C'_2 \left(\phi_{km,2} n_k n_m \delta_{ij} - \frac{3}{2} \phi_{ik,2} n_j n_k - \frac{3}{2} \phi_{ij,2} n_i n_k \right) \frac{C_\ell k^{\frac{3}{2}}}{\varepsilon d} \end{aligned} \quad \text{Eqn. 50}$$

where $C'_1 = 0.5$, $C'_2 = 0.3$

$$C_\ell = \frac{C_\mu^{\frac{3}{4}}}{\kappa} \quad \text{Eqn. 51}$$

where $C_\mu = 0.09$ and $\kappa = 0.4187$

Buoyancy could cause turbulence in a flow, the effect of turbulence is expressed as:

$$G_{ij} = -\rho \beta_T (g_i \overline{u'_j \theta} + g_j \overline{u'_i \theta}) \quad \text{Eqn. 52}$$

$$\overline{u_i \theta} = \frac{\mu_t}{Pr_t} \left(\frac{\partial T}{\partial x_i} \right) \quad \text{Eqn. 53}$$

where $Pr_t = 0.85$

$$G_{ij} = -\frac{\mu_t}{\rho Pr_t} \left(g_i \frac{\partial \rho}{\partial x_j} + g_j \frac{\partial \rho}{\partial x_i} \right) \quad \text{Eqn. 54}$$

Turbulence kinetic energy can be modelled as:

$$k = \frac{1}{2} \overline{u'_i u'_i} \quad \text{Eqn. 55}$$

$$\frac{\partial}{\partial t} (\rho k) + \frac{\partial}{\partial x_i} (\rho k u_i) = \frac{\partial}{\partial x_j} \left[\left(\mu + \frac{\mu_t}{\sigma_k} \right) \frac{\partial k}{\partial x_j} \right] + \frac{1}{2} (P_{ii} + G_{ii}) - \rho \varepsilon (1 + 2M_t^2) + S_k \quad \text{Eqn. 56}$$

where $\sigma_k = 0.82$ and S_k is user-defined source term

Dissipation rate can be modelled as:

$$\varepsilon_{ij} = \frac{2}{3}(\rho\varepsilon + Y_M) \quad \text{Eqn. 57}$$

where $Y_M = 2\rho\varepsilon M_t^2$

$$M_t = \sqrt{\frac{k}{a^2}} \quad \text{Eqn. 58}$$

where $a \equiv \sqrt{\gamma RT}$ is the speed of sound

Scalar dissipation rate ε is computed similarly to standard k - ε model, i.e.

$$\begin{aligned} \frac{\partial}{\partial t}(\rho\varepsilon) + \frac{\partial}{\partial x_i}(\rho\varepsilon u_i) \\ = \frac{\partial}{\partial x_j} \left[\left(\mu + \frac{\mu_t}{\sigma_\varepsilon} \right) \frac{\partial \varepsilon}{\partial x_j} \right] C_{\varepsilon 1} \frac{1}{2} [P_{ii} + C_{\varepsilon 3} G_{ii}] \frac{\varepsilon}{k} - C_{\varepsilon 2} \rho \frac{\varepsilon^2}{k} - C_{\varepsilon 2} \rho \frac{\varepsilon^2}{k} \\ + S_\varepsilon \end{aligned} \quad \text{Eqn. 59}$$

where $\sigma_\varepsilon = 1.0$, $C_{\varepsilon 1} = 1.44$, $C_{\varepsilon 2} = 1.92$, $C_{\varepsilon 3}$ is evaluated as Eqn. 40.

Also similar to k - ε model, turbulent viscosity can be expressed as

$$\mu_t = \rho C_\mu \frac{k^2}{\varepsilon} \quad \text{Eqn. 60}$$

where $C_\mu = 0.09$

Wall boundary conditions can be modelled as:

$$\frac{\overline{u_\tau'^2}}{k} = 1.098, \frac{\overline{u_\eta'^2}}{k} = 0.247, \frac{\overline{u_\lambda'^2}}{k} = 0.655, -\frac{\overline{u_\tau' u_\eta'}}{k} = 0.255 \quad \text{Eqn. 61}$$

where τ is the tangential coordinate, η is the normal coordinate, and λ is the binormal coordinate

Convective heat and mass transfer can be modelled as:

$$\frac{\partial}{\partial t}(\rho E) + \frac{\partial}{\partial x_i} [u_i(\rho E + p)] = \frac{\partial}{\partial x_j} \left[\left(k + \frac{c_p \mu_t}{Pr_t} \right) \frac{\partial T}{\partial x_j} + u_i(\tau_{ij})_{eff} \right] + S_h \quad \text{Eqn. 62}$$

where E is the total energy and $(\tau_{ij})_{eff}$ is the deviatoric stress tensor

$$(\tau_{ij})_{eff} = \mu_{eff} \left(\frac{\partial u_j}{\partial x_i} + \frac{\partial u_i}{\partial x_j} \right) - \frac{2}{3} u_{eff} \frac{\partial u_k}{\partial x_k} \delta_{ij} \quad \text{Eqn. 63}$$

which is off by default in pressure-based solver

Large Eddy Simulation (LES) Model

Subgrid-scale models employed Boussinesq hypothesis which results in using RANS models to compute subgrid-scale turbulent stresses

$$\tau_{ij} - \frac{1}{3}\tau_{kk}\delta_{ij} = -2\mu_t\bar{S}_{ij} \quad \text{Eqn. 64}$$

where μ_t is the subgrid-scale turbulent viscosity, τ_{kk} is the subgrid-scale stresses, and \bar{S}_{ij} is the rate-of strain tensor for resolved scale

$$\bar{S}_{ij} \equiv \frac{1}{2}\left(\frac{\partial \bar{u}_i}{\partial x_j} + \frac{\partial \bar{u}_j}{\partial x_i}\right) \quad \text{Eqn. 65}$$

In incompressible flow

$$\tau_{kk} = \gamma M_{sgs}^2 \bar{p} \quad \text{Eqn. 66}$$

where M_{sgs} is the subgrid Mach number, which is usually small at low Mach number flow.

$$q_j = -\frac{\mu_t}{\sigma_t} \frac{\partial \phi}{\partial x_j} \quad \text{Eqn. 67}$$

where ϕ is the subgrid-scale scalar turbulence flux, q_j is the subgrid-scale flux

Eddy-viscosity in Smagorinsky-Lilly model can be expressed as:

$$\mu_t = \rho L_s^2 |\bar{S}| \quad \text{Eqn. 68}$$

where L_s is the mixing length for subgrid scales and $|\bar{S}| \equiv \sqrt{2\bar{S}_{ij}\bar{S}_{ij}}$

$$L_s = \min(\kappa d, C_s \Delta) \quad \text{Eqn. 69}$$

where κ is the von Kármán constant, d is the distance to the closest wall, C_s is Smagorinsky constant and Δ is the local grid scale

$$\Delta = V^{\frac{1}{3}} \quad \text{Eqn. 70}$$

where $C_s = 0.23$ (Lilly's derivation) or $C_s = 0.1$ (ANSYS Fluent default)

Inlet boundary conditions is set as “No Perturbations”, hence stochastic components of the flow are neglected

NONMENCLATURE

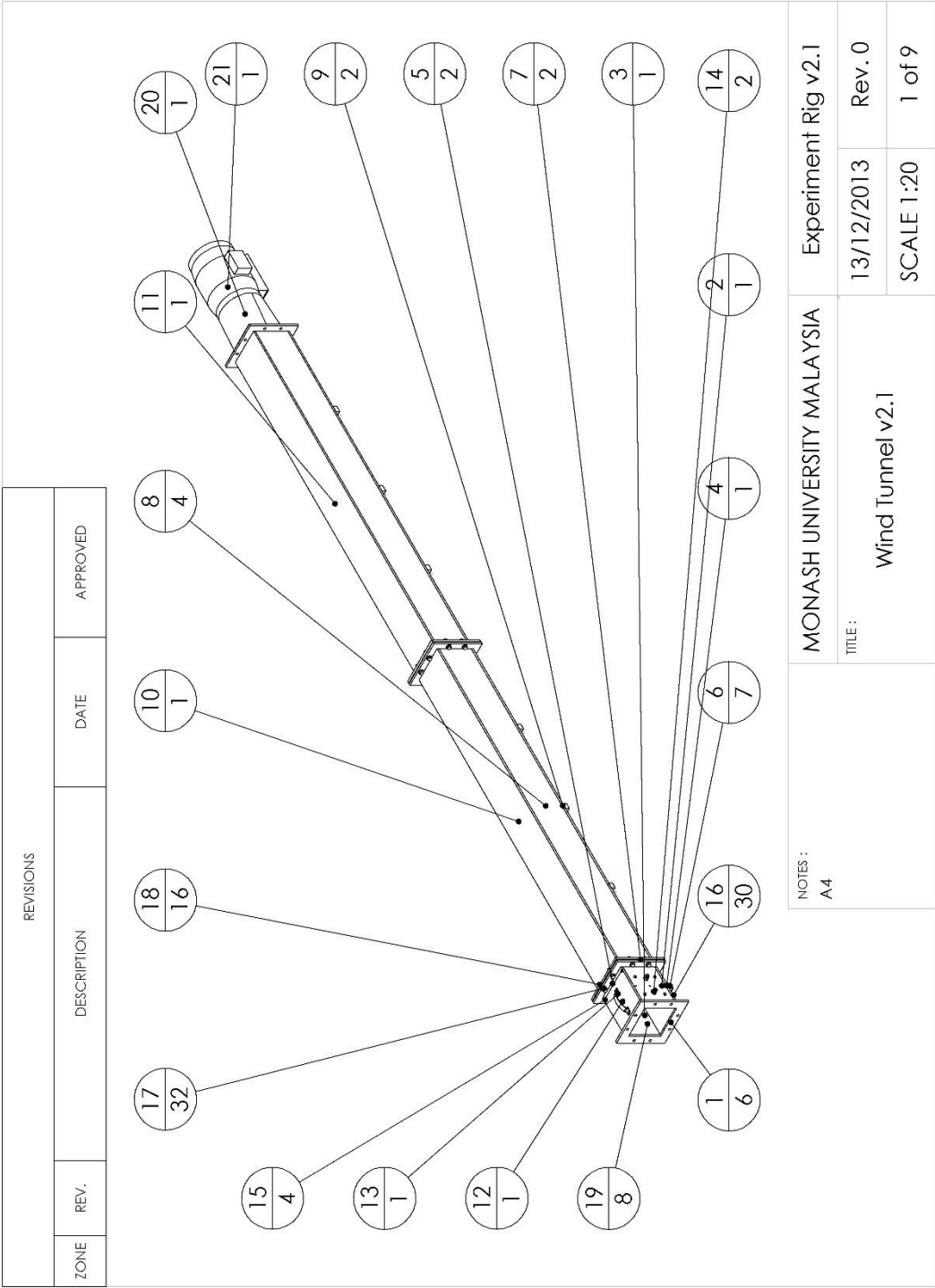
C_d	Drag coefficient
C_μ	Function of mean strain and rotation rates, angular velocity of the system rotation, and turbulence fields
C_d	Drag coefficient
E	Total energy
\vec{f}	Other bodily forces
g_i	Gravitational vector
G_b	Generation of turbulence kinetic energy due to buoyancy
G_k	Generation of turbulence kinetic energy due to mean velocity gradients
k_{eff}	Effective thermal conductivity
M_t	Turbulence Mach number
n_k	x_k component of the unit normal to the wall
Pr_t	Turbulence Prandtl number for energy
S	Modulus of the mean rate-of strain tensor
Sc_t	Turbulence Schmidt number
$S_k \text{ and } S_\varepsilon$	Source term for k and ε
v	Component of the flow velocity parallel to the gravitational vector
Y_M	Contribution due to fluctuating dilatation in compressible turbulence to overall dissipation rate

Greek Symbols

κ	von Kármán constant
β_T	Coefficient of thermal expansion
μ_t	Turbulence viscosity
$\overline{\Omega_{ij}}$	Mean rate-of -rotation tensor
$\phi_{ij,1}$	Slow pressure-strain
$\phi_{ij,2}$	Rapid pressure-strain
$\phi_{ij,w}$	Wall-reflection
σ_k and σ_ε	Turbulent Prandtl number for k and ε
T or $(\tau_{ij})_{eff}$	Deviatory stress tensor

Appendix B

Wind Tunnel Technical Drawings



ITEM NO.	DESCRIPTION	QTY.
1	10mm 240 x 240 - 160 x 160 Flange	6
2	10mm x 220 x 160 Plate Channel A	1
3	10mm x 220 x 160 Plate Channel B	1
4	10mm x 220 x 180 Plate Channel Bottom	1
5	10mm x 15 x 180 Plate Channel Top	2
6	20mm x 30 x 180 Channel Support	7
7	3mm Flange Rubber Gasket	2
8	10mm x 1808.80 x 160 Outflow Channel Side	4
9	10mm x 1808.80 x 180 Outflow Channel Bottom	2
10	10mm x 1808.80 x 180 Outflow Channel Top A	1
11	10mm x 1808.80 x 180 Outflow Channel Top B	1
12	Plate Access	1
13	Handle	1
14	1/4" BSP x 10mm OD Tube Connector	2
15	M5 Hex Socket Cap Screw x 15mm	4
16	M10 x 1.5 Bolt x 40mm	30
17	M10 Washer	32
18	M10 x 1.5 Nut	16
19	5.3mm Hole Cover	8
20	1mm - 160 x 160 to 200 dia Transition Duct	1
21	Axial Fan Kruger MTD200	1

NOTES :
A4

MONASH UNIVERSITY MALAYSIA

TITLE :

Bill of Material
Wind Tunnel v2.1

Experiment Rig v2.1

13/12/2013
Rev. 0

SCALE 1:20
2 of 9

